Harpur Hill, Buxton
Derbyshire, SK17 9JN
T: +44 (0)1298 218000
F: +44 (0)1298 218590
W: www.hsl.gov.uk

HEALTH & SAFETY LABORATORY

CFD Modelling of Evaporating Hydrocarbon Sprays

CM/07/04

Project Leader: **S. E. Gant**

Author(s): **S. E. Gant, A. Heather, A. Kelsey**

Science Group: **Health Improvement**

DISTRIBUTION

D. Painter	Customer Project Officer, HID CI5, HSE
S. Barlow	HID, CI1, HSE
M. Bilio	HID, OSD3.2, HSE
A. Garrod	FOD, CHSD3, HSE
A. D. Curran	Director of Health Improvement, HSL
D. Morgan	Head of Mathematical Modelling Unit, HSL
M. J. Ivings	Head of Fluid Dynamics Team, HSL

PRIVACY MARKING:

Available to the public.

HSL report approval:	**A. D. Curran**
Date of issue:	**August 2007**
Job number:	**JS2005019**
Registry file:	**025593**
Electronic file name:	**CM0704.doc**

ACKNOWLEDGEMENTS

The authors would like to thank Scott Samuelsen and Vincent McDonell (University of California at Irvine Combustion Laboratory) for assistance in providing the experimental data used in this report, and Chris Staples and Ian Jones at ANSYS-CFX.

CONTENTS

EXECUTIVE SUMMARY

The aim of this study is to validate CFD models of evaporating sprays. The need for this work has arisen following the Buncefield Incident, where volatile liquid overspilling from the top of a bulk storage tank formed an evaporating spray that led to the build-up of a large vapour cloud, which subsequently ignited, causing extensive damage [1-3]. There is a need to be able to predict the amount of flammable vapour produced from such spray releases to help quantify the hazard.

A survey of the scientific literature could find no experimental or CFD studies of liquid hydrocarbon releases of scale and type similar to the Buncefield Incident. Instead, for the current study, two methanol sprays formed by pressurized releases through nozzles have been examined. Well-documented experimental data is available for the two cases, published by McDonell & Samuelsen [4-9], and CFD simulations have previously been made for one of the cases [10-12]. Although the sprays differ from the Buncefield-type of release scenario, they enable CFD evaporation models to be validated against detailed experimental data.

The two sprays examined exhibit different flow phenomena. One is an air-assisted spray where both methanol liquid and air are released through the nozzle at high speed (around 40 m/s). The development of the spray follows similar behaviour to a simple free-jet. CFD models are able to predict correctly the velocity of the gas phase (air and vapour) without difficulty. The CFD droplet evaporation models also produce methanol vapour concentrations in reasonably good agreement with the experimental measurements. Sensitivity tests are undertaken to show how the CFD predictions change due to small changes in the inlet conditions and to examine the significance of various sub-models.

The second case considered is a non-air-assist spray, where the flow is driven entirely by the droplets entraining air into the spray. The flow velocities are much lower in this case, typically around 3 m/s. This scenario is closer to the spray release at Buncefield, although the mass flux of spray droplets per unit volume of air is much lower and the droplets are much finer in the case studied here. The CFD results for this spray are generally not in as good experimental agreement compared to the previous case. The shape of the gas phase velocity profile is not well predicted despite experimental data being used to set the majority of the necessary inlet conditions. However, the predicted peak methanol vapour concentrations are mostly well predicted. Sensitivity tests for this case show that the initial droplet size distribution has a significant effect on predicted vapour concentrations but relatively little effect on the induced velocities in the gas phase. Possible reasons for the discrepancies between CFD predictions and experiments are discussed.

Overall, this study indicates that CFD models can provide reasonably accurate predictions of spray evaporation. The error in the predicted total flow rate of methanol vapour produced in both of the evaporating sprays was generally less than 25%. Care should be taken, however, in extrapolating the performance of CFD models from one spray to another, where the balance of physical effects such as droplet collisions and spray entrainment are different.

Only droplets composed of a single component, methanol, are considered in the present study. Future work could examine evaporation of a multi-component liquid, such as petrol or crude oil to enable more direct comparisons to Buncefield-like releases.

It is recommended that experiments should be performed of weir-type sprays of volatile hydrocarbons to study their evaporation behaviour. Experimental data is needed for these types of releases to further validate CFD models and develop other simplified engineering approximations for the prediction of vapour cloud build-up.

1 INTRODUCTION

On the morning of 11th December 2005 there was a large explosion and fire at the Buncefield Oil Storage Depot, near Hemel Hempstead. The subsequent investigation into the incident indicated that the explosion had been caused by the ignition of a large flammable vapour cloud that was produced by overfilling of one of the large petrol tanks on the site [1-3]. When the tank was overfilled, petrol flowed from vents in the roof of the tank and cascaded over the tank sides, falling around 15 metres to the floor of the bund. Figures 1 and 2 show the likely release scenario which has been reproduced in experiments undertaken at HSL. As the liquid fuel fell through the air, it partially evaporated and produced a cold, dense, vapour-rich cloud. This dense cloud then spread over a considerable area across the Buncefield site before it was ignited. There have previously been other major incidents involving ignition of a vapour cloud produced by sprays of volatile liquids from tank overfilling (e.g. Naples harbour fuel storage depot, Italy in 1985 [13] and Sri Racha Refinery, Thailand in 1999 [14]).

In the wake of the Buncefield Incident, there has been a reassessment of the risk posed by other fuel depots around the UK. Simplified models for the production of vapour from a tank overfilling incident are currently being developed at HSL. These models rely to a certain extent on Computational Fluid Dynamics (CFD) to help predict how much vapour is produced by a spray of liquid fuel. In view of the importance of this modelling work, the present report documents a validation study that has been undertaken to help establish the accuracy of CFD models of droplet evaporation and provide a better understanding of the model's capabilities and limitations.

The objectives of the present study were:

- To carry out a literature survey of previous validation work to help identify suitable modelling approaches.
- To compare CFD model predictions against experimental data for evaporating hydrocarbon sprays.
- To assess the accuracy of the CFD model and, where necessary, provide guidance on which sub-model(s) should be used for which scenario.
- To help understand the CFD model's sensitivities, i.e. identify the important factors affecting the model predictions.
- To provide indications of the cost of running such simulations in terms of the ease-of-use, numerical stability and computing time required.

The fluid dynamics involved in a falling spray of evaporating hydrocarbon droplets is complex. Section 2 presents a brief review of the important physical processes and the CFD models used. Experimental studies of evaporating sprays are also briefly surveyed. Section 3 presents the results of CFD simulations of two evaporating sprays. The final section provides a discussion of the results and some conclusions.

Figure 1 A storage tank similar in design to that which was overfilled in the Buncefield Incident (left) and a close-up view of an experiment showing how liquid overflowing through a roof vent produces a spray of liquid (right).

Figure 2 Photo of a vertical section of tank wall showing the liquid spray falling over around 15 metres.

2 LITERATURE SURVEY

2.1 PHYSICS OF SPRAYS

Sprays are used in a wide range of technical applications, including internal combustion engines, gas turbines, rocket engines, fire/explosion suppression systems, agricultural fertilizer/pesticide applications and spray-dryers. Over the last 50 years, a considerable amount of research has been undertaken within the science and engineering community to understand the physical processes involved in sprays and to develop mathematical spray models. It is beyond the scope of the present work to provide a detailed survey of this large body of work. The reader is instead referred to the recent text books by Sirignano [15] and Crowe *et al*. [16]. However, a brief description of the fundamental physics and important factors to consider in modelling sprays is provided below.

2.1.1 Spray Formation

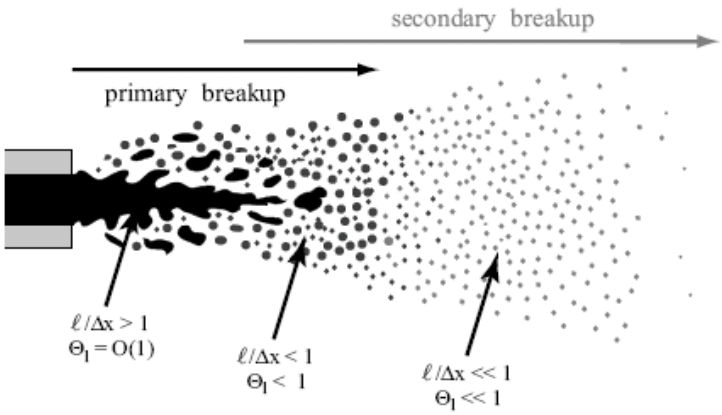

Figure 3 Breakup of a liquid jet (from Herrmann [17], reproduced with permission from Stanford University Center for Turbulence Research)

Sprays are formed by the breakup of a liquid stream into discrete droplets. This process is illustrated in Figure 3. The breakup, or atomisation, process is usually divided into two consecutive steps: primary and secondary breakup. During primary breakup the liquid stream flowing through the nozzle or orifice is fragmented to form ligaments, network structures and large droplets under the action of internal processes and interaction with the surrounding gas. As these large droplets are convected downstream, they undergo further breakup due to the combined action of aerodynamic forces and droplet collisions (secondary breakup). Figure 4 describes some of the different mechanisms involved in secondary breakup. Because of the difficulty in examining these mechanisms experimentally, researchers are increasingly turning to high-quality direct numerical simulations to understand the underlying physical processes [18, 19]. An example of a numerical simulation of a single droplet fragmenting in a shear flow is shown in Figure 5.

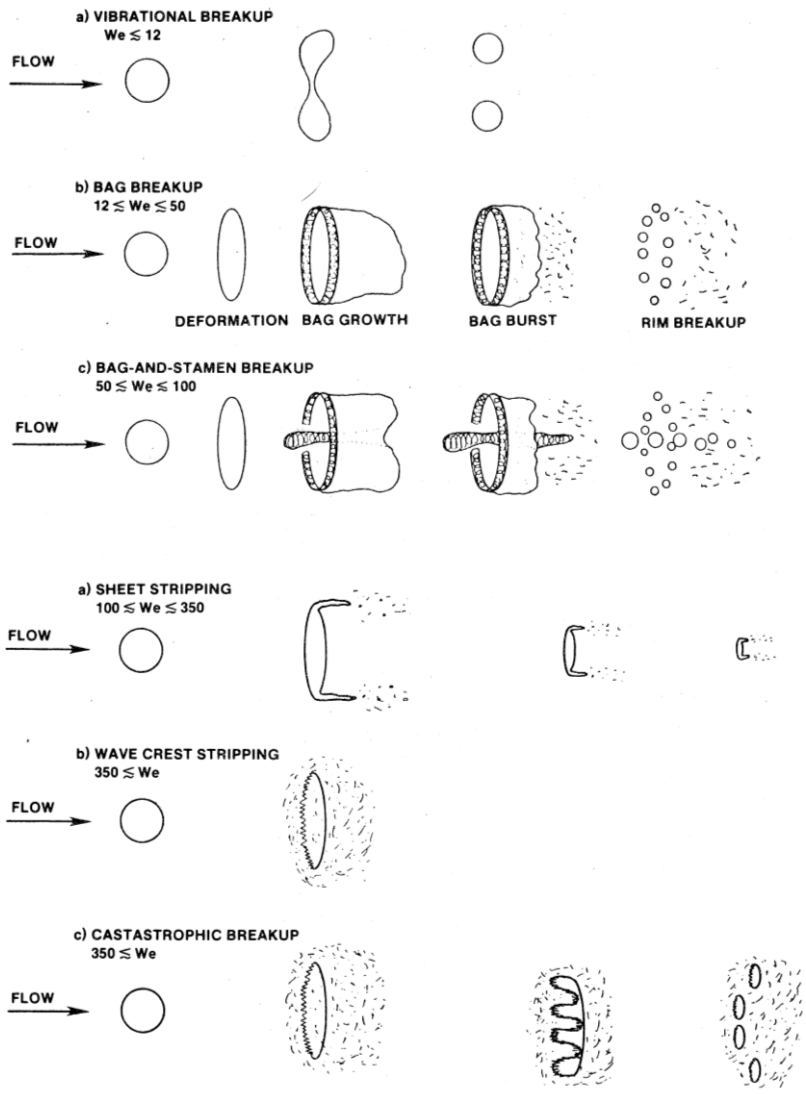

Figure 4 Secondary droplet breakup mechanisms (reprinted from Pilch & Erdman [20] with permission from Elsevier)

The various modes of droplet breakup are often classified according to two dimensionless parameters: the Weber and Ohnesorge numbers. The Weber number, *We*, represents the ratio of disruptive hydrodynamic forces to stabilizing surface tension forces:

$$We = \frac{\rho V^2 D}{\sigma} \tag{1}$$

where ρ is the density of the fluid continuum surrounding the droplet, V is the relative velocity between droplet and fluid continuum, D is the droplet diameter and σ the surface tension of the droplet. The Ohnesorge number[1], *On*, characterises the viscous effects on the droplet breakup:

[1] *Also referred to as the Laplace number or 'Z' number.*

$$On = \frac{\mu_d}{\sqrt{\rho_d D \sigma}} \tag{2}$$

where μ_d and ρ_d are the dynamic viscosity and density of the droplet, respectively. The Ohnesorge number only involves droplet parameters and it is implicitly assumed that the viscosity of the surrounding fluid medium is low in comparison to the droplet viscosity.

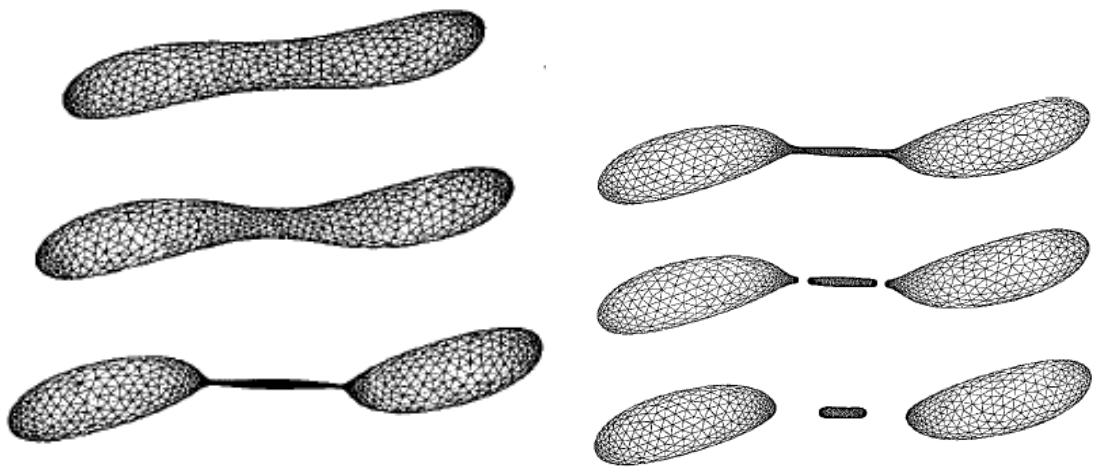

Figure 5 Simulations of droplet breakup in a shear flow (reprinted from Cristini & Renardy [19] with permission from Elsevier)

Five different secondary droplet breakup mechanisms were identified by Pilch & Erdman [20] (Figure 4) and each was found to occur within a particular Weber number range. Below a critical Weber number, We_c, droplet breakup does not occur and the droplet size remains stable. An empirical correlation describing how this critical Weber number varies as a function of the Ohnesorge number was developed by Brodkey [21]:

$$We_c = 12\left(1 + 1.077 On^{1.6}\right) \tag{3}$$

This equation can be rearranged to express the relative droplet-gas velocity as a function of the maximum stable droplet diameter and other material and flow properties, as follows:

$$V = \left\{ \frac{12\sigma}{\rho D} \left[1 + 1.077 \left(\frac{\mu_d}{\sqrt{\rho_d D \sigma}} \right) \right] \right\}^{0.5} \tag{4}$$

A graph showing how the slip velocity, V, varies as a function of maximum stable diameter, D, for water, hexane and a simplified petrol mixture are shown in Figure 6. These show that for a droplet to air slip velocity of 15 m/s, the maximum stable droplet diameter for water is approximately 3.3 mm, for hexane 0.8 mm and for petrol 0.9 mm.

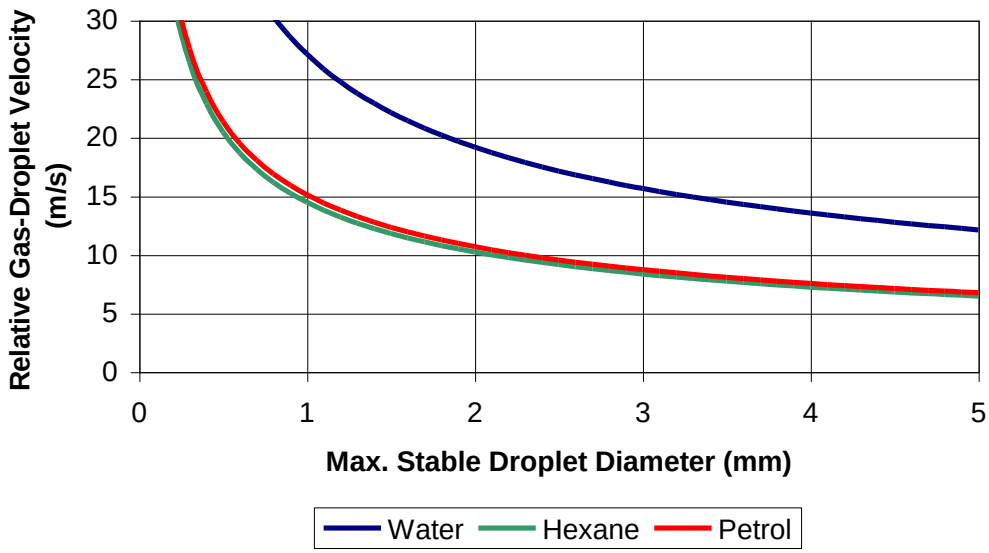

Figure 6 Maximum stable droplet sizes as a function of the relative velocity between the droplets and surrounding air using the empirical formula of Brodkey [21]. The petrol is composed of 9.6% butane, 17.2% pentane, 16% hexane and 57.2% decane by mass.

2.1.2 Droplet Momentum

The interaction between droplets and air involves the exchange of momentum, mass and heat. The evolution of momentum is governed by Newton's second law: net force equals the rate of change of momentum. For droplets or particles, this is expressed in terms of the Basset-Boussinesq-Oseen (BBO) equation (see [16]):

$$\underbrace{m\frac{d\mathbf{v}}{dt}}_{\text{Rate of change of droplet momentum}} = \underbrace{\frac{1}{2}\rho_c C_D A|\mathbf{u}-\mathbf{v}|(\mathbf{u}-\mathbf{v})}_{\text{Drag Force}} + \underbrace{V_d(-\nabla p + \nabla\cdot\boldsymbol{\tau})}_{\text{Pressure gradient \& shear stress}} \tag{5}$$

$$+\underbrace{\frac{\rho_c V_d}{2}(\dot{\mathbf{u}}-\dot{\mathbf{v}})}_{\text{Virtual mass force}} + \underbrace{\frac{3}{2}D^2\sqrt{\pi\rho_c\mu_c}\left[\int_0^t \frac{\dot{\mathbf{u}}-\dot{\mathbf{v}}}{\sqrt{t-t'}}dt' + \frac{(\mathbf{u}-\mathbf{v})_0}{\sqrt{t}}\right]}_{\text{Basset Force}} + \underbrace{m\mathbf{g}}_{\text{Gravitational Force}}$$

where **u** and **v** are the gas and droplet velocity vectors respectively, m is the mass, ρ density, C_D the droplet drag coefficient, A the projected frontal area of the droplet, V_d the particle or droplet volume, p pressure, $\boldsymbol{\tau}$ shear stress, D the droplet diameter, t time and g gravity. Subscript c refers to properties of the continuous (gas) phase, subscript 0 to an initial condition at time $t = 0$, and a dot above a letter to the time-derivative. The variable t' in the Basset force term represents a time-scale that varies from 0 to time t. The BBO equation is applicable to a wide range of flows, not only droplets but particles and bubbles. The carrier phase can also be either liquid or gas.

In the BBO equation, the combined pressure gradient and shear stress term represents the forces on the droplet due to acceleration of the continuous phase. It is only significant when the

continuous phase has a density comparable or larger than that of the droplet (e.g. oil droplets in water). The virtual mass force term represents the force required to accelerate the surrounding fluid. This is important in bubbly flows where the displaced fluid mass exceeds the particle mass. The Basset force, sometimes known as the 'history' term, accounts for the deviation of the flow behaviour around the particle from the steady state flow conditions, due to the development of the boundary layer around the droplet as the relative velocity changes with time. The Basset force can be important in unsteady flows, however Rudinger [22] noted that the term is insignificant for a 10 μm particle in a stream oscillating at less than 700 Hz (see Crowe *et al*. [16] for details).

For a 'waterfall' spray of petrol from a tank release under atmospheric conditions, the motion of the droplets is dominated by the drag and the gravitational forces. Similarly, for the simple sprays considered in this validation study, the pressure gradient/shear stress term, the virtual mass term and the Basset force can all be neglected. Empirical correlations for the drag coefficient, C_D, and the influence of turbulence on the droplet momentum are discussed below.

2.1.3 Droplet Temperature

The rate of change of the droplet temperature is governed by four physical processes: conduction, convection, radiation and mass-transfer-related heat transfer (evaporation or condensation). For the applications considered in the present work, radiation can be ignored. The mean temperature of a droplet, T_d, is then governed by the following energy equation:

$$mc_p \frac{dT_d}{dt} = \dot{Q} + h_{fg} \frac{dm}{dt} \tag{6}$$

where c_p is the specific heat at constant pressure for the droplet, $\dot{Q}$ is the rate of heat transfer to the droplets (accounting for conduction and convection) and h_{fg} is the latent heat of evaporation of the droplet material. Mathematical models of sprays often evaluate $\dot{Q}$ using empirical correlations involving dimensionless heat transfer parameters such as the Nusselt number.

Evaporation and condensation involve a change of phase between liquid and vapour at the droplet surface and transport of droplet vapour to/from the droplet surface. For the applications considered here, the droplets are not boiling and the driving force for evaporation is the concentration gradient between the droplet surface and the free-stream. This is expressed by Fick's Law:

$$\frac{dm}{dt} = -D_v A \frac{\partial \rho}{\partial n} \tag{7}$$

where D_v is the diffusion coefficient for the particular species, A is the area across which the mass transfer takes place and $\partial\rho/\partial n$ is the density gradient of the particular species in the direction normal to the surface. Mathematical models for droplet mass transfer often approximate D_v using empirical correlations involving the Sherwood number, Sh.

2.1.4 Vapour Pressures

The propensity of a substance to evaporate can be expressed in terms of its saturation vapour pressure. The concept of the saturation vapour pressure is based on the notion of partial pressures. This is best explained in terms of an example. Normal atmospheric air can be treated as an ideal gas mixture whose pressure, P, is equal to the sum of the partial pressures of water vapour, P_A, and dry air, P_B:

$$P = P_A + P_B \tag{8}$$

Here, the partial pressure of the water vapour, P_A, can be thought of as the pressure the water vapour would exert if it existed alone at the temperature and volume of the mixture. Considering the case of water droplets suddenly introduced into a container filled with dry air, the liquid droplets will start evaporating and the amount of water vapour in the air will gradually rise until the conditions within the container reach an equilibrium. At this equilibrium condition, the water vapour is in balance with the liquid and there is no tendency for the material to evaporate or condense. The value of the partial pressure of the water vapour at this point is the equilibrium, or saturation, vapour pressure, P^{sat}.

The saturation vapour pressure for a particular substance changes as a function of the temperature and pressure. Values of P^{sat} for water and some common refrigerants can be found in the Steam Tables [23]. At a temperature of 15˚C and 101.325 kPa the saturation vapour pressure for water is P^{sat} = 1.68 kPa.

The concentration of water vapour in air, expressed as a molar fraction, X_A, is given by:

$$X_A = \frac{N_A}{N_A + N_B} \tag{9}$$

where N is the number of moles and subscripts A and B refer to the water vapour and dry air properties, as before. The ideal gas law ($PV = NR_uT$) can be applied separately for each of the substances, A and B, giving:

$$X_A = \frac{P_A V / R_u T}{P_A V / R_u T + P_B V / R_u T} \tag{10}$$

Hence, the molar fraction, X_A, can be expressed in terms of the ratio of partial pressures:

$$X_A = \frac{P_A}{P_A + P_B} \tag{11}$$

The denominator in this expression is just the total pressure (since $P = P_A + P_B$). For water in equilibrium with air at 15ºC, the molar fraction is then:

$$X_A = \frac{1.68}{101.325} = 0.017 \tag{12}$$

Under equilibrium conditions at 15ºC the air will therefore contain 1.7 % water vapour by volume. By definition, the saturation vapour pressure of water at 100˚C and 1 atm is 101.325 kPa, i.e. at 100˚C the water can exist in equilibrium as a pure vapour. Substances with a saturation vapour pressure greater than 101.325 kPa will exist as a vapour under equilibrium conditions at 1 atm (e.g. for butane the saturation vapour pressure is 173 kPa at 15ºC).

There are two commonly used empirical correlations used to determine the saturation vapour pressure for a substance at a given pressure and temperature. The first is the Clausius-Clapeyron equation:

$$P^{sat} = \exp\left[\frac{h_{fg}}{R}\left(\frac{1}{T_b} - \frac{1}{T}\right)\right] \tag{13}$$

where h_{fg} is the latent heat of vaporization, R the gas constant for the substance, T_b the boiling point at a pressure of 101.325 kPa and T the temperature. The second relation is Antoine's equation:

$$P^{sat} = P_{ref}\ \exp\left(A - \frac{B}{T + C}\right) \tag{14}$$

where P_{ref} is standard atmospheric pressure and A, B and C are material-specific coefficients.

The above equations can be used to determine the percentage of a pure substance that will exist in air under equilibrium conditions, assuming that the substance evaporating is a pure liquid. In many cases, however, the evaporating substance is a mixture of many components (a notable example being the petrol released at Buncefield).

For droplets composed of multiple components, the equilibrium concentration of species A in the air is the single-component value scaled by the molar fraction of A in the liquid droplet, x_A:

$$X_A = \frac{P_A^{sat}}{P} x_A \tag{15}$$

This equation is known as Raoult's Law. The law holds true for 'ideal' solutions where the intermolecular forces between molecules of the pure substances are similar to the forces between molecules of one component and another. This is a good approximation for mixtures of hydrocarbons such as butane, pentane, hexane and decane. Raoult's law is not appropriate for polar solutions, such as mixtures of water and ethanol.

For an example of Raoult's law in use, consider droplets of pure pentane evaporating in air. Pentane has a saturation vapour pressure of 46.4 kPa at 15ºC and atmospheric pressure, so the equilibrium molar fraction of pentane vapour is 46.4 / 101.325 = 45.8%. If instead the droplets are composed of 50% pentane and 50% hexane liquid by volume, the equilibrium concentration of pentane vapour in the air will be halved to only 46.4 × 0.5 / 101.325 = 22.9%.

A summary of relevant material properties for a number of hydrocarbon compounds is provided for reference in Table 1.

Table 1 Summary of hydrocarbon and other common chemical properties at 15ºC and atmospheric pressure (sources: CRC Handbook of Thermophysical and Thermochemical Data [24] and Yaws [25]).

Chemical Name	*Composition*	*Density, ρ (kg/m^3)*	*Viscosity, μ (N.s/m^2)*	*Surface Tension, σ (N/m)*	*Saturation Vapour Pressure, P^{sat} (Bar)*
Butane	C_4H_{10}	585	1.83×10^{-4}	1.30×10^{-2}	1.732
Pentane	C_5H_{12}	631	2.81×10^{-4}	1.66×10^{-2}	0.464
Hexane	C_6H_{14}	665	3.25×10^{-4}	1.91×10^{-2}	0.128
Decane	$C_{10}H_{22}$	736	10.04×10^{-4}	2.44×10^{-2}	0.0008
Water	H_2O	1037	11.62×10^{-4}	7.56×10^{-2}	0.0168
Methanol	CH_3OH	796	6.19×10^{-4}	2.49×10^{-2}	0.0988

2.2 CFD MODELS FOR EVAPORATING SPRAYS

The fundamental equations governing fluid flow behaviour are the *Navier-Stokes* equations. These equations are coupled and non-linear meaning that to find a solution one has to use a numerical method with a discrete approximation to the equations and then iterate towards a solution. Computational Fluid Dynamics (CFD) consists of finding the solution to the Navier-Stokes equations using this numerical approach.

In the present work, the flow of air and vapour is modelled using an Eulerian approach. This consists of a computational grid that is fixed in space through which the gases flow. Momentum, mass and energy conservation equations are solved in each grid cell to find the velocity, temperature, pressure and concentration distributions.

The spray of droplets is modelled using a particle-tracking or Lagrangian approach. The spray is represented by a number of discrete computational particles. Each fluid particle typically represents a large number of droplets with given mean size and transport properties. Individual particles are tracked through the flow domain from their injection point until they escape the domain or evaporate completely.

For the types of spray considered here, the coupling between the Eulerian phase and Lagrangian particles is two-way. Particles falling through the air are subjected to drag forces and their trajectories can be affected by turbulent perturbations in the air. The air is also affected by the drag of the droplets and is entrained into the spray. This two-way coupling is important in mass transfer where the vapour concentration in the gas phase affects the rate of evaporation from the droplets and the evaporation rates effect the vapour concentration. Droplet evaporation also leads to a temperature decrease which affects the vapour pressure and hence the evaporation rates.

Two-way coupling is achieved by introducing source terms derived from the Lagrangian solution into the Eulerian transport equations. The overall CFD solution is obtained by iterating between the Eulerian and Lagrangian calculations.

In the present work, the commercial CFD code, CFX, has been used. A description of the droplet models available in this code are described below.

2.2.1 Droplet Momentum

Droplet trajectories are calculated using the BBO equation. The pressure/stress gradient, virtual mass, and Bassett force terms are neglected. For the flows considered here, ignoring these terms should have very little or no effect. The drag coefficient, C_D, in the BBO equation is calculated using the Schiller-Naumann correlation [26], given by:

$$C_D = \max\left[\frac{24}{Re}\left(1 + 0.15 Re^{0.687}\right), 0.44\right] \tag{16}$$

where the Reynolds number, *Re*, is calculated from:

$$Re = \frac{\rho_g \left(|\mathbf{u} - \mathbf{v}|\right) d}{\mu_g} \tag{17}$$

where **u** is the gas mixture velocity and **v** the droplet velocity, *d* the droplet diameter and μ_g the gas viscosity and ρ_g the gas density.

For a typical droplet in the validation cases studied later, with a slip velocity of 12 m/s and droplet diameter 40 microns, the droplet Reynolds number is:

$$Re = \frac{(1.2)(12)\left(40 \times 10^{-6}\right)}{\left(1.57 \times 10^{-5}\right)} \approx 37 \tag{18}$$

This is in the transitional region, between Stokes flow ($Re < 1$) and the inertial range ($750 < Re < 3.5 \times 10^5$). At this Reynolds number, the drag coefficient is:

$$C_D = \max\left[\frac{24}{37}\left(1 + 0.15(37)^{0.687}\right), 0.44\right] \approx 1.8 \tag{19}$$

The Schiller-Naumann drag model is only strictly valid for spherical particles. However, Gosman & Clerides [27] comment that inaccuracies in the modelled drag coefficient are usually self-compensating in sprays: an increase in the drag coefficient leads to a more rapid fall in velocity which leads to reduced drag (see also Patterson *et al*. [28]).

The evaporation of vapour from a liquid droplet leads to thickening of the laminar boundary layer surrounding the droplet. This so-called “blowing” effect leads to a drop in the drag coefficient. Crowe *et al*. [16] describe a number of approaches used to take account of blowing effects. The correlation perhaps most widely used is that of Eisenklam *et al*. [29]:

$$C_D = \frac{C_{D,0}}{1 + B} \tag{20}$$

where $C_{D,0}$ is the drag coefficient without evaporation effects and *B* is the ‘transfer number’ determined from:

$$B = \frac{c_p \Delta T}{h_L} \tag{21}$$

where c_p is the specific heat at constant pressure and h_L the latent heat of vaporisation. For methanol droplets with a temperature difference of 20 ˚C, the transfer number is:

$$B = \frac{(81.1)(20)}{(37430)} = 0.043 \tag{22}$$

This equates to a difference in the drag coefficient of around 4% due to blowing effects. For comparison, a change in the slip velocity from 12 to 10 m/s causes a 10% increase in the drag coefficient using the Schiller-Nauman correlation. Blowing effects are therefore likely to be relatively minor for the sprays studied here and have been ignored.

2.2.2 Droplet Temperature

The temperature of the droplets is affected by convective heat transfer with the air and latent heat transfer associated with evaporation. The modelled convective heat transfer, $\dot{Q}$, is a function of the Nusselt number, *Nu*, as follows.

$$\dot{Q} = \pi d \lambda \, Nu \left(T_g - T\right) \tag{23}$$

where T_g and T are the temperatures of the gas phase and the droplet respectively, d the droplet diameter and λ is the thermal conductivity of the gas. The empirical Nusselt number correlation is given by:

$$Nu = 2 + 0.6 Re^{0.5} \left(\mu \frac{c_p}{\lambda} \right)^{1/3} \tag{24}$$

where μ is the dynamic viscosity.

2.2.3 Droplet Mass Transfer

If, as is the case here, the liquid droplets are not boiling, the mass transfer rate is calculated from:

$$\frac{dm}{dt} = \min\left[\pi d \rho_g D_g Sh \frac{W_c}{W_g} \ln\left(\frac{1 - X_g}{\max\left[1 - X_c, \varepsilon_0\right]} \right), 0 \right] \tag{25}$$

where subscript c refers to the gas-phase properties of the component evaporating and g to the properties of the gas mixture, W is the relative molecular mass, d is the droplet diameter, D is the diffusivity, and ε_0 is a small number used here to avoid numerical difficulties when X_g becomes close to unity. The molar fractions, X_c and X_g, are calculated from:

$$X_c = \frac{\gamma_c \rho_g}{W_c C_g} \qquad\qquad X_g = \frac{P_c^{sat}}{P} \tag{26}$$

where γ is the mass fraction, ρ is the density, C is the molar concentration $\left(C = P / R_u T\right)$, P_c^{sat} is the vapour pressure for the component evaporating, found from Antoine's equation (Eqn 14), and P is the total pressure in the gas mixture. The expression for the molar fraction, X, can be expanded as follows:

$$X_c = \frac{\gamma_c \rho_g}{W_c C} = \frac{[m_c/m_g][m_g/Vol]}{[m_c/N_c][N_g/Vol]} = \frac{N_c}{N_g} \tag{27}$$

where m is the mass, N is the number of moles and Vol a unit volume. Since the molar fraction, X_c, is equivalent to the ratio of the partial pressure, P_c to the total pressure, P, Equation (25) can also be written:

$$\frac{dm}{dt} = \pi d \rho_g D_g Sh \frac{W_c}{W_g} \ln\left(\frac{P - P_c^{sat}}{\max[P - P_c, P\varepsilon_0]} \right) \tag{28}$$

The Sherwood number, Sh, is calculated from:

$$Sh = 2 + 0.6 Re^{1/2} Sc^{1/3} \tag{29}$$

and the Schmidt number, Sc, from:

$$Sc = \frac{\mu_g}{\rho_c D_c} \tag{30}$$

The droplet continues evaporating until the partial pressure of the droplet component in the gas phase, P_c, reaches the ratio of the saturation vapour pressure P_c^{sat}. The model only accounts for evaporation, not condensation, since the min[…,0] function in Equation (25) means that the mass transfer rate can only be negative.

2.2.4 Secondary Breakup Models

There are numerous, mainly empirically-derived correlations for secondary droplet breakup, e.g. [20, 30-33]. In the present work, the Reitz-Diwakar model has been tested [30]. This calculates the rate of change of droplet radius, r, from:

$$\frac{dr}{dt} = -\frac{(r - r_{stable})}{t_{br}} \tag{31}$$

where r_{stable} and t_{br} are the new radius for the stable droplet and the characteristic breakup time. Values of r_{stable} and t_{br} are found from either of two expressions, depending on the local Weber and Reynolds numbers, to account for the effect of stripping and bag breakup modes (see Figure 4):

For $We > We_{crit}$ (bag breakup):

$$r_{stable} = \frac{6\sigma}{\rho_g V_{slip}^2} \qquad t_{br} = C_1 \sqrt{\frac{\rho_d r^3}{2\sigma}} \tag{32}$$

For $\frac{We}{\sqrt{Re}} > C_{s1}$ (stripping breakup):

$$r_{stable} = \frac{\sigma^2}{2\rho_g^2 V_{slip}^3 \nu} \qquad t_{br} = C_2 \frac{r}{V_{slip}} \sqrt{\frac{\rho_d}{\rho_g}} \tag{33}$$

where V_{slip} is the droplet-gas slip velocity, ρ_d is the droplet density and ρ_g is the gas density. The constants in the Reitz-Diwakar model are: We_{crit} = 12.0, $C_1 = \pi$, C_2 = 20.0 and C_{s1} = 0.5.

If the Weber and Reynolds criteria are met and a particle breaks-up to form child particles, the mean droplet diameter is reduced. No new computational particles are created and there is no perturbation to the path of the particle due to the droplet fragmentation.

2.2.5 Turbulent Dispersion

In a turbulent flow, the instantaneous velocity field ($\tilde{u}$) can be decomposed into two parts: a time-averaged mean velocity (U) and a velocity fluctuation about this mean (u):

$$\tilde{u} = U + u \tag{34}$$

In the present work, a Reynolds-Averaged Navier Stokes (RANS) approach has been used to approximate the effects of turbulence. In this approach, the Eulerian transport equations solve for the *mean* flow velocity (U) and the effect of turbulence on the mean flow (u) is modelled. This is the standard treatment used for industrial CFD simulations of turbulent flows (see Pope [34] or Versteeg & Malasekera [35] for further details).

In many CFD spray simulations, only the mean velocity U is used in the Lagrangian equations of motion governing the particle behaviour. As a consequence of this, the particle trajectories are governed only by the mean flow velocity and are unaffected by any turbulent fluctuations or localized eddy motion.

A number of different turbulent dispersion models have been proposed to try to introduce disturbances to the particle trajectories to account for turbulence effects (e.g. [36, 37]). These are commonly based on trying to reconstruct the instantaneous velocity field ($\tilde{u}$) by adding some synthetic stochastic velocity fluctuation to the mean velocity. The modelled instantaneous velocity field is then used in the BBO equation for the particle motion.

In the present work, the dispersion model of Gosman & Ioannides [38] has been tested. This approximates the instantaneous velocity, $\tilde{u}$, from:

$$\tilde{u} = U + \underbrace{\Gamma\left(\frac{2}{3}k\right)^{0.5}}_{u} \tag{35}$$

where U is the mean velocity interpolated from the Eulerian field to the particle position, k is the local turbulent kinetic energy and Γ is a normally-distributed random number. Rather than recalculate the reconstructed velocity fluctuation, u, at every Lagrangian time-step, it is only updated periodically according to an “eddy-lifetime” criteria.

This involves calculating an eddy length scale and time-scale from:

$$l_e = c_\mu^{3/4} \frac{k^{3/2}}{\varepsilon} \qquad t_e = \frac{l_e}{\sqrt{2k/3}} \tag{36}$$

where ε is the turbulence dissipation rate. There are two possible ways in which the particle interacts with this eddy. Either it is moving sufficiently slowly such that it remains within the eddy for the whole of the eddy lifetime (t_e) or it is moving sufficiently fast that it traverses the eddy in a transit time, t_r, given by:

$$t_r = \frac{l_e}{|\mathbf{u} - \mathbf{v}|} \tag{37}$$

The interaction time between the particle and the eddy is the minimum of the eddy lifetime and the residence time:

$$t_I = \min(t_e, t_r) \tag{38}$$

The velocity fluctuation, u, in Equation (35) is assumed to hold for the duration of the particle interaction time, t_I, which may last a number of Lagrangian time-steps. When it comes to the end of the interaction time interval, a new reconstructed velocity fluctuation, u, is obtained at the particle's new position using local values of the turbulent kinetic energy, k. This approach is termed a Discontinuous Random Walk model by McInnes & Bracco [36].

Using the particle dispersion model, particle trajectories are not deterministic. Two identical particles injected from the same point at different times may follow separate trajectories due to the influence of the random turbulent velocity fluctuation.

A greater number of particles must be used in CFD simulations involving a particle dispersion model to produce statistically smooth behaviour from the stochastic velocity fluctuations. Numerical convergence in steady flows can also become worse because of the random nature of the sources appearing the Eulerian phase.

3 CFD VALIDATION STUDY

Whilst it would have been most useful to consider a weir-type flow of droplets falling under gravity to best simulate the Buncefield tank release scenario, a literature search could find no experimental data or previous CFD simulations available for such conditions. Instead, two methanol sprays have been studied which were produced by a flow of liquid methanol forced under pressure through two different nozzles. The cases were chosen following a literature survey that indicated that they provided the most comprehensive and reliable data set.

3.1 OVERVIEW OF THE EXPERIMENTS

In the early 1990's, McDonell, Samuelsen and Adachi at the UCI Combustion Laboratory (University of California) performed a number of experiments on methanol sprays [4-9]. The aim of their work was to improve understanding of spray evaporation and spray combustion and help the development of mathematical spray models. Their work has been chosen for this validation study because of the high level of detail in their experiments and the comprehensive documentation they provided. Measurements were taken for both the gas phase and droplets using Phase Doppler Interferometry (PDI) and Infrared Extinction/Scattering (IRES). The data set includes axial and radial velocities (both mean and fluctuating), mass fluxes, droplet size distributions and methanol vapour concentrations at seven measurement planes downstream of the nozzle. Three different types of pressurized atomizers were tested: a simple methanol spray (denoted RSA01), an air-assisted spray (RSA02) and a swirling spray (RSA03). In the current work only the first two sprays are considered. Schematics of the apparatus and nozzle configuration are shown in Figures 7 and 8.

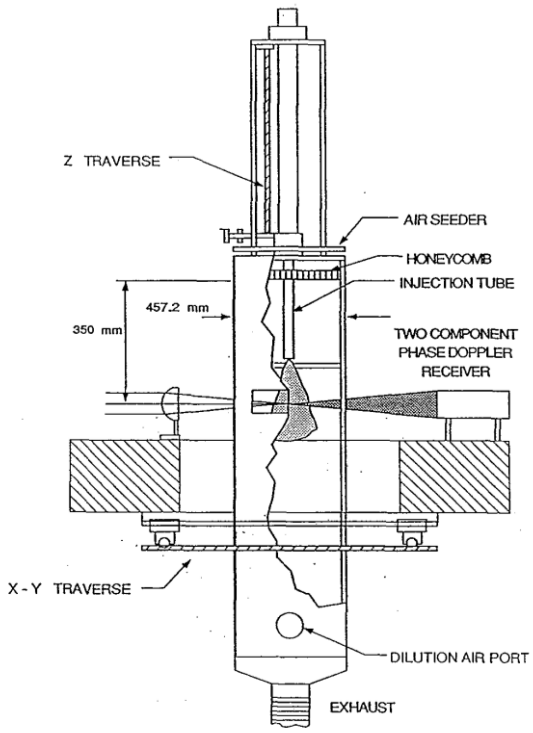

Figure 7 Schematic of the apparatus used in the McDonell & Samuelsen experiments, reproduced from [9] with permission from ASME.

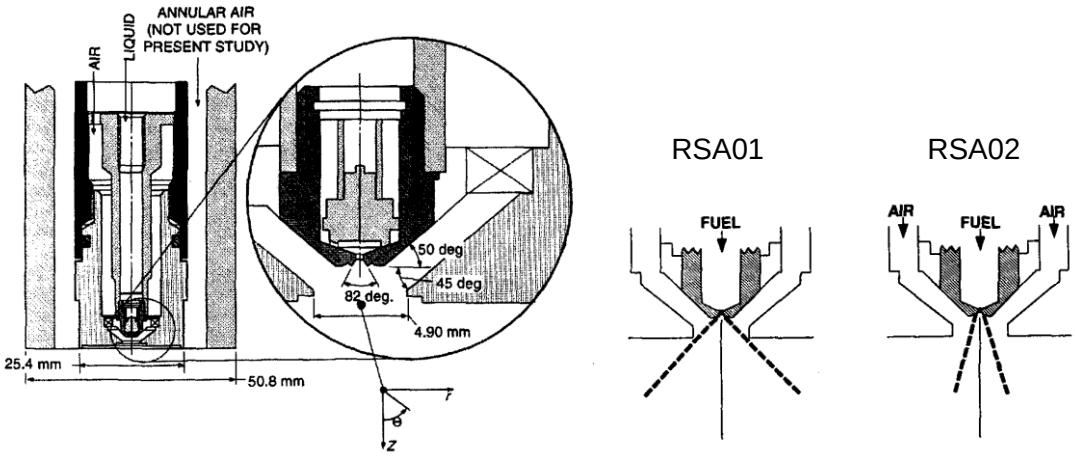

Figure 8 Sectional view through the McDonell & Samuelsen nozzle showing the dimensions (left) and flow configuration for the RSA01 and RSA02 cases (right), reproduced from [9] with permission from ASME.

The RSA01 and RSA02 cases exhibit quite different flow phenomena. In the RSA01 case, the maximum velocity of the air entrained into the spray was typically around 3 or 4 m/s. For the RSA02 spray, the velocity is an order of magnitude higher, between 20 and 50 m/s, due to the high-velocity air coflow through the nozzle.

In terms of CFD modelling, the air-assisted RSA02 case is the simpler of the two flows, consisting of essentially a free jet with some suspended droplets. The effect of the droplets on the gas flow is limited, i.e. the coupling is essentially one-way between the continuum gas phase and the dispersed droplet phase in terms of momentum transfer. For the RSA01 case, the flow is more difficult to predict, since the flow is driven entirely by the droplets and there is a strong two-way coupling.

The similarity between the RSA02 case and a free-jet flow is demonstrated by the top graph in Figure 9, which shows profiles of the axial gas velocity at various locations downstream from the nozzle. In this plot, the velocity and radial coordinate have been non-dimensionalised using the centreline velocity, U_0, and the radial location, $r_{1/2}$, where the velocity drops to half the centreline value. The symbols, indicating experimental values at each location, all fall roughly on top of one another, indicating that as the spray spreads and the velocity decays, the shape of the velocity profile remains the same. This phenomena, known as “self-similarity”, is typical of free-jet flows. The red line shown in Figure 9 is an empirical velocity profile for free jets taken from Pope [34].

A similar plot for the RSA01 case shows significantly more scatter about the empirical profile (Figure 9, bottom) suggesting that in this case, the flow is not self-similar. At the 75 and 100 mm positions, there is a local velocity minima at the centreline which is responsible for some of the velocities exceeding $U/U_0 = 1$. In the experiments, there was a small downward co-flow of air of 0.8 m/s around the periphery of the spray to reduce recirculation in the outer region of the duct. This air entered through the honeycomb shown in Figure 7. The coflow is responsible for the experimental profiles decaying to $U/U_0 \approx 0.2$, instead of zero, on the outer edges of the spray in Figure 9. In the RSA02 case, the spray velocity is an order of magnitude higher and so this effect is less pronounced.

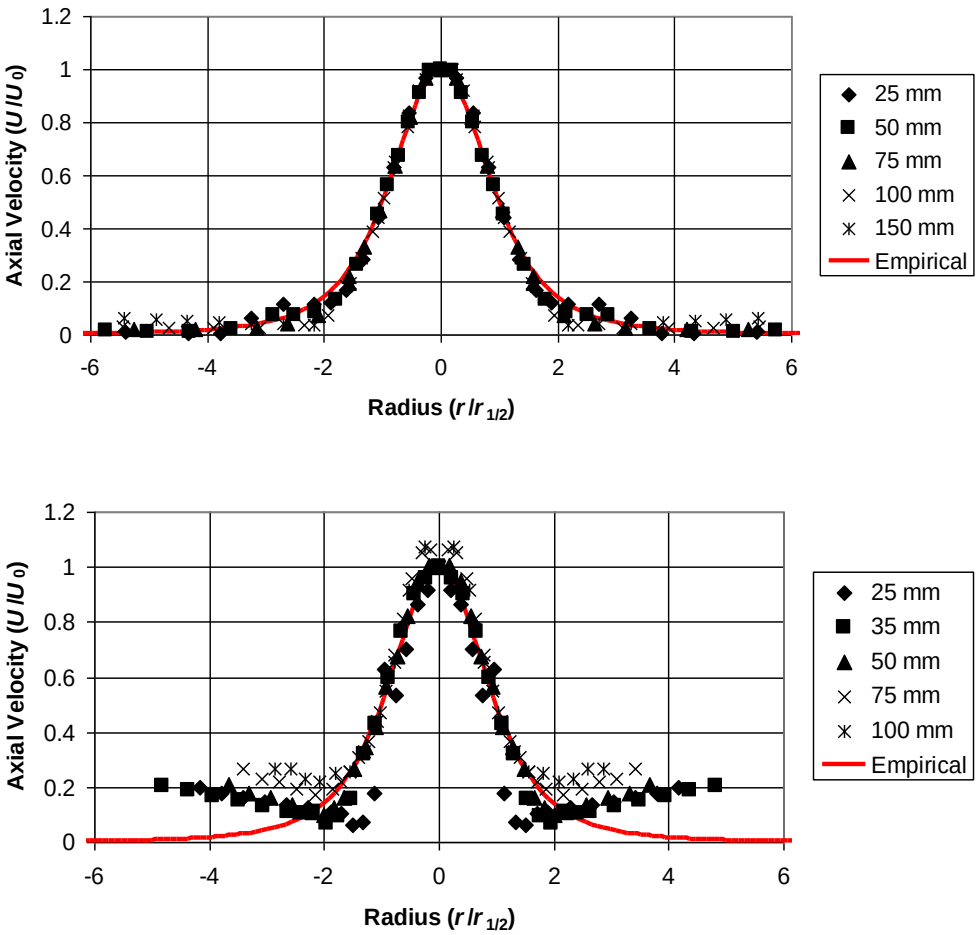

Figure 9 Dimensionless axial velocity profiles for the McDonell & Samuelsen RSA02 case (top) and RSA01 case (bottom). The red line is an empirical free-jet profile taken from Pope [34].

Relatively simple CFD models are able to predict the correct velocity field for a free-jet with a good degree of accuracy. To confirm this, a plot showing the self-similar behaviour for the RSA02 case predicted using the SST turbulence model is shown in Figure 10.

The two test cases: RSA01 and RSA02 are complementary for model evaluation purposes. In the RSA02 case, the velocity field should closely match the experimental results, so the effect of evaporation can be studied in relative isolation. If accurate predictions are obtained for the amount of vapour produced here, it would indicate that the CFD models for mass and heat transfer are a good approximation to reality. For the RSA01 case, the effects of both droplet drag and evaporation are combined. The predictions in this case are therefore dependent on the coupling of momentum, mass and heat transfer. In presenting the results below, the RSA02 flow is examined first because of the simpler nature of the flow.

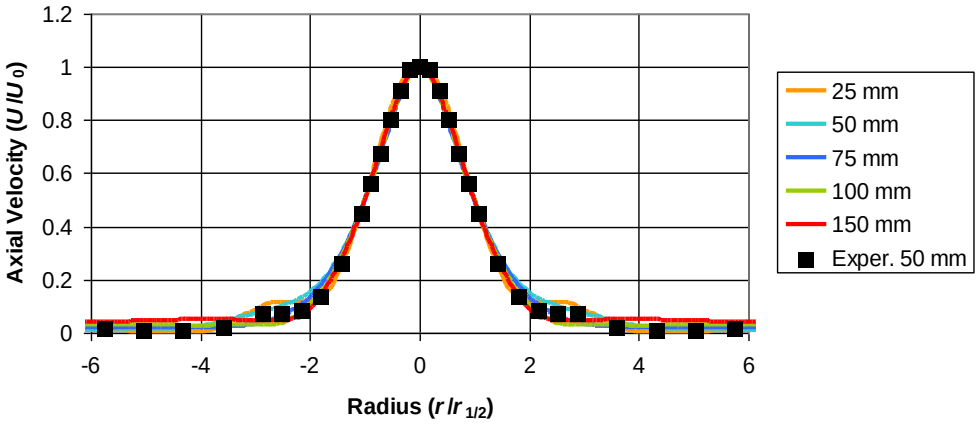

Figure 10 Dimensionless predicted vapour velocity profiles using CFD with the SST turbulence model for the RSA02 air-assisted spray. Symbols are the McDonell & Samuelsen measurements at a position 50 mm downstream from the nozzle.

Uncertainties in the Experiments

The most significant uncertainties in the McDonell & Samuelsen [4-9] data relate to the mass flux of vapour and droplets. In the experiments, measurements were made of the methanol vapour concentrations and gas phase velocities. These can be used to calculate the total volume flux of methanol vapour across each measurement plane. Similarly, the PDI system measured droplet diameters and count rates and these can be used to calculate the total liquid volume flow rate. The vapour and liquid flow rates can be added together to find the total methanol flow rate at each measurement plane, which should be a conserved property. However, calculations showed that the integrated mass flow rates are significantly less than the known mass flow rate of liquid released through the nozzle, which was measured independently using a flow meter.

For the RSA01 case, the mass flow rate of methanol released through the nozzle was 1.26 g/s[2]. At the first measurement plane, 7.5 mm downstream from the nozzle, the vapour and liquid mass flow rates integrated from the measured profiles were 0.031 g/s and 0.292 g/s, i.e. only 2.4% and 23% of the total mass flux. The values increase slightly further downstream: at the 25 mm measurement plane the integrated vapour and droplet mass fluxes are 3.3% and 58% for the RSA01 case and 6.0% and 28% for RSA02 case.

It is likely that most of the "missing" mass flux is in the liquid phase. The PDI system was not able to measure all the droplets passing through the measurement cell. If more than one droplet appeared in the measuring volume simultaneously, the measurement was rejected. In the dense spray region in the core of the spray, the droplet arrival rate was higher than the sampling frequency of the PDI system so the measured droplet number fluxes incurred greater error.

It is uncertain whether the measured mass flux profiles are the same shape as those in reality, and only need to be scaled-up to match 100% of the total mass flux, or whether an entirely different shape of profile should be used. In two previous studies of the RSA02 case, by Kaer *et*

[2] *There is some confusion over the mass flux value for the RSA02 case. In two papers published in 1993, McDonell & Samuelsen stated that the flow rate was 1.26 g/s [6,7]. However, in a later paper published in 1995 [9] it was reported as being 1.26 g/s for the RSA02 case and 1.32 g/s for the RSA01 case. In the present work, is has been assumed that the correct value is 1.26 g/s.*

al. [10] and Kelsey [11], the latter approach was taken to account for the 'missing' material. It was assumed that most of the rejected droplet measurements were in the core of the spray where the mass flux density was highest. In the Kaer *et al*. study [10], the mass flux profile near the inlet was assumed to take the same shape as that measured by a sample probe at 50 mm whereas Kelsey [11] adopted a similar Gaussian mass flux profile as shown in Figure 11.

To assess the sensitivity of CFD results to this uncertainty, a number of different droplet mass flux profiles were used as inlet boundary conditions for both the RSA01 and RSA02 cases. The profiles used are shown in Figure 11 and 12, marked 'Scaled' and 'Gaussian'. The shape of the modified Gaussian profiles have been chosen largely arbitrarily. In all cases, the total mass flux for the Scaled and Gaussian profiles (vapour + liquid) results in a total methanol mass flux of 1.26 g/s.

The aim of using the Gaussian profiles is to examine the degree of sensitivity to this parameter in the results. No tuning has been performed to try to make the CFD results match the experiments by modifying the shape of the profiles. In the RSA02 case, two different Gaussian profiles have been tested (marked as Gaussian A and Gaussian B in Figure 12). The peak mass flux for Gaussian A profile occurs on the spray centreline whereas for the Gaussian B profile the peak occurs off the axis, at a radius of 10 mm.

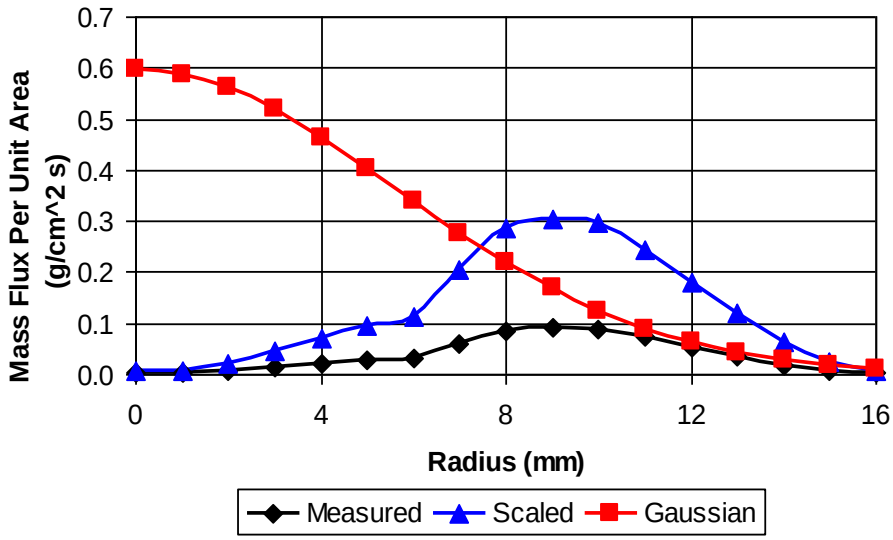

Figure 11 Droplet mass flux profiles for the RSA02 case at the 25 mm measurement plane. The Measured profile is that given by the data of McDonell & Samuelsen.

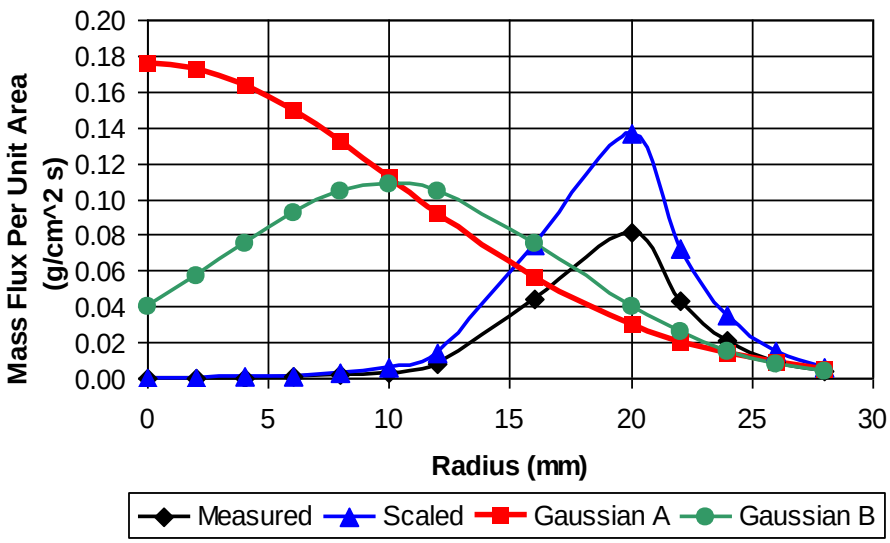

Figure 12 Droplet mass flux profiles for the RSA01 case at the 25 mm measurement plane. The Measured profile is that given by the data of McDonell & Samuelsen.

3.2 PREVIOUS CFD SIMULATIONS

The McDonell-Samuelsen RSA02 experiments have been studied previously using CFD by Kaer *et al*. [10], Kelsey [11] and Raju [12, 39]. The first two of these studies used the same commercial code, CFX, as used in the present work, although a much older version of the software than is available today (version 4.1 and 4.1C, compared to version 10.0 used here). In all cases an Eulerian-Lagrangian formulation was used with a RANS turbulence model. Kaer *et al*. [10] found that the CFD predictions were overall in good agreement with the experiments although the evaporation rates were slightly under-predicted. They also examined the reacting methanol sprays measured by McDonell & Samuelsen using a two-step gas combustion model.

Kelsey [11] examined the McDonell-Samuelsen RSA02 spray to help develop models for flashing jet releases. The predicted spreading rate of the continuous (gas) phase was found to be slightly underpredicted. It was suggested that this might have been a consequence of the choice of inlet conditions, in particular the assumed turbulence dissipation rate profile. The methanol vapour concentration was also slightly underpredicted. Calculations were performed using two commercial CFD codes, CFX-4.1C and Star-CD 3.05.

The study by Raju [12] focussed mainly on predictions of the reacting spray cases although some results were also shown for the non-reacting RSA02 spray. The results from the simulations were reported to be in reasonable agreement with the experimental data, although the axial gas velocities were actually underpredicted by up to 30% in the non-reacting spray. In the more recent work [39], four atomisation models and three different secondary droplet breakup models were tested. Both the reacting and non-reacting McDonell-Samuelsen experiments were examined, although not with every model combination. Comparisons with experimental measurements for the non-reacting case were not shown.

No previous simulations of the RSA01 test case could be found in the literature.

3.3 DETAILS OF THE CFD MODEL

CFD calculations for the two spray evaporation test cases have been carried out using the commercial CFD code, CFX-10.0. Details of the mathematical models used in CFX for spray evaporation are described in Section 2.

Figures 13 and 14 show three different approaches that were tested to model the flow geometry. In the first case, droplets were injected from the nozzle location and the geometry was fully three-dimensional. Relatively complex distributions for the initial droplet sizes and velocities were used to try to match the experimental inlet conditions. This involved interfacing the CFX code with specially-written Fortran subroutines. Unfortunately, although reasonable results could be obtained for non-evaporating droplets, there were some problems interfacing the Fortran code with CFX for the case when mass and heat transfer were included in the model. No solution could be found to this problem within the limited time-scale of this project and so an alternative approach was explored. Details of the Fortran coding have been included in the Appendix for reference.

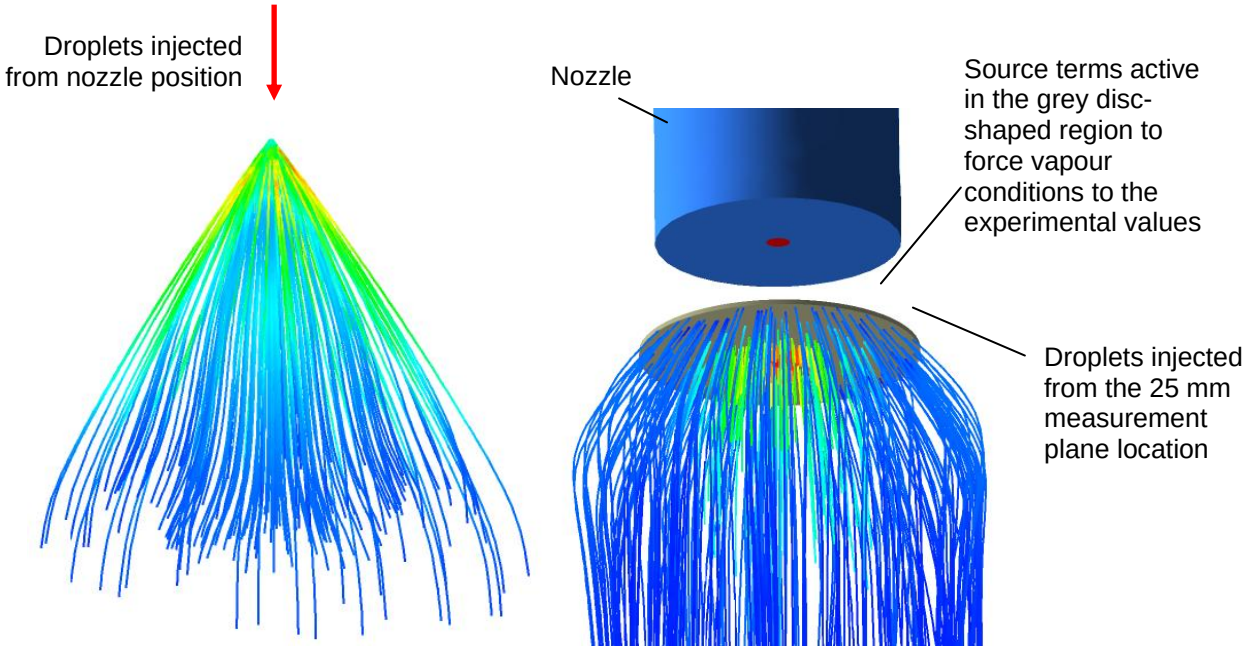

Figure 13 Two alternative approaches used to simulate the methanol sprays: injecting the droplets from the nozzle location (left) and injecting them at the 25 mm measurement position (right). Neither of these approaches produced satisfactory behaviour and both were abandoned.

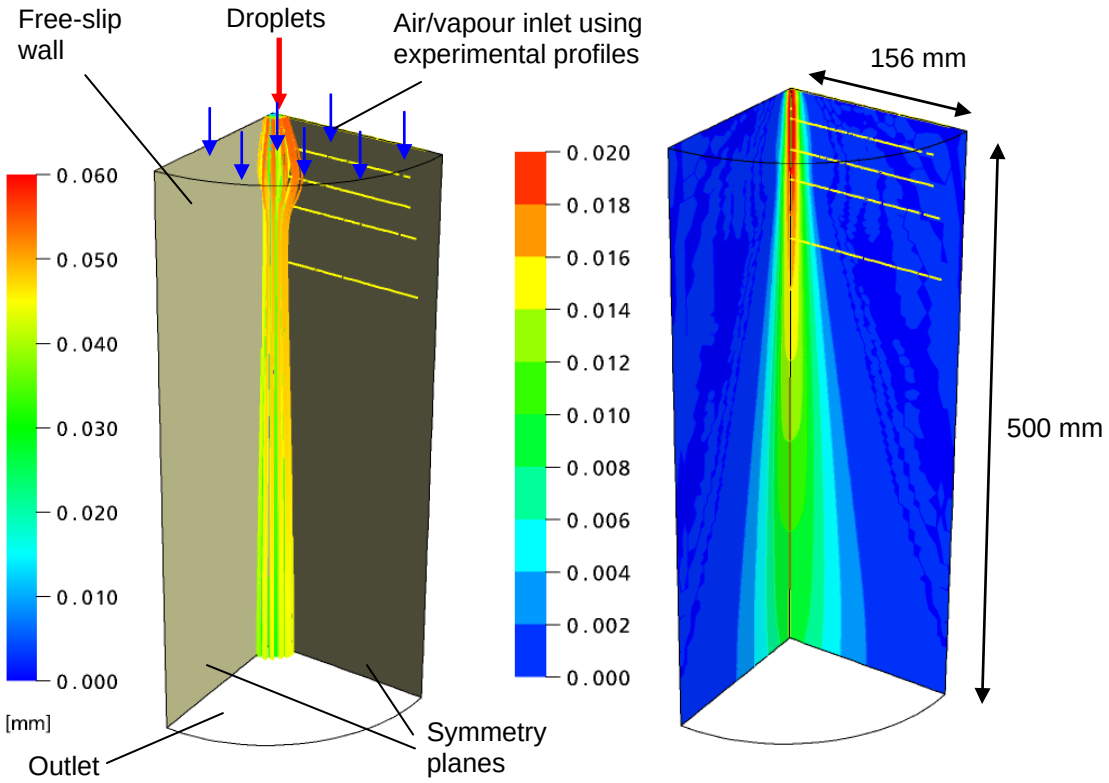

Figure 14 Two views of the flow geometry used to simulate the McDonell & Samuelsen sprays. Typical droplet trajectories coloured with their diameter (left) and methanol vapour concentrations (right). Yellow lines show the positions of the experimental measurement planes at 25 mm, 50 mm, 75 mm, 100 mm and 150 mm. The 25 mm plane coincides with the inlet to the flow domain.

A second approach also considered the full 3D geometry but injected droplets some distance downstream from the nozzle (Figure 13, right-hand plot). Instead of starting the CFD simulations at the nozzle and comparing predictions to the seven downstream measurement planes, the simulations started from the 25 mm position and predictions were compared to the four measurement planes further downstream. To provide the correct inlet conditions for the gas phase, source terms in the modelled equations were used to force the velocity and methanol vapour mass fraction to the experimental values at the 25 mm position. Figure 13 shows the disc-shaped region in which these source terms were active. Although this approach was able to match the experimental conditions at 25 mm, the CFD predictions rapidly diverged from the measurements. It was not clear whether this was a consequence of the source term treatment used, the peripheral flow around the disc-shaped region, the relatively coarse mesh, or some other effect.

To resolve this issue, a third approach was used, similar to that adopted in two previous studies [11, 12] (Figure 14). Only one quarter of the flow geometry was modelled to enable use of finer meshes. This is a reasonable approximation given that the flow should be axisymmetric[3]. The

[3] *An even more efficient solution would have been to solve the flow equations in axisymmetric coordinates which would have enabled use of a 2D mesh, but unfortunately CFX-10 does not have this functionality.*

computational flow domain started at the 25 mm position downstream from the nozzle. The flow conditions measured in the experiments were applied directly to the face of the domain, avoiding the need for special source term treatments. The dimensions of the flow domain and plots of the typical droplet trajectories are also shown in Figure 14. The same domain size and meshes were used for the RSA01 and RSA02 cases. Details of the computational mesh and the numbers of particles used in the CFD simulations are provided in the Appendix (Sections 5.1 and 5.2).

One of the limitations of the approach shown in Figure 14 is that the simulations only model the flow behaviour downstream of the 25 mm measurement plane. Most if not all of the droplet breakup occurs in the region upstream of the 25 mm position and so the performance of breakup models cannot be assessed. There is still significant air entrainment and evaporation taking place within the CFD domain. Figure 15 plots the volume flux of methanol vapour calculated by integrating the vapour fluxes in McDonell & Samuselsen's data. This shows that the amount of vapour increases throughout the region of interest. Close to the nozzle both RSA01 and RSA02 cases produce similar amounts of vapour. Further downstream, the RSA02 case exhibits an almost linear increase in vapour flow rate with distance whilst the non-air-assisted RSA01 spray, which spreads more rapidly, exhibits a faster rate of increase of methanol vapour production.

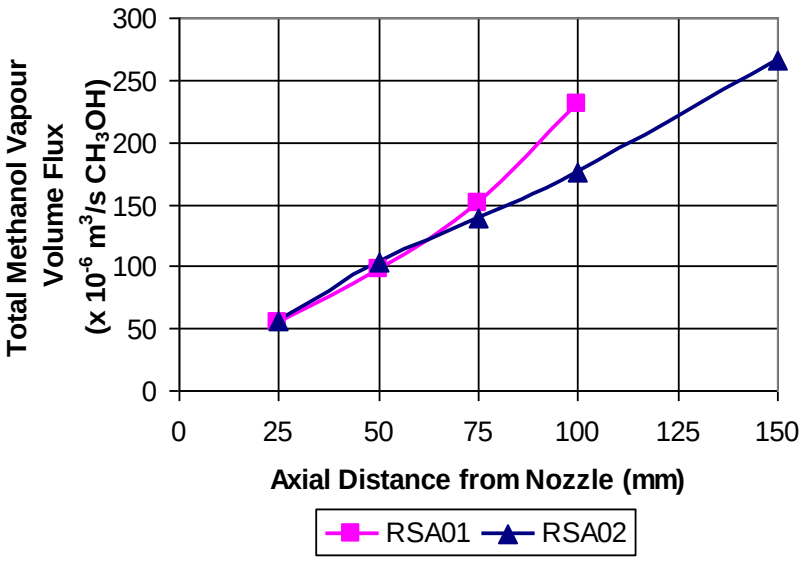

Figure 15 The rate of increase in the total methanol vapour volume flux with the distance from the nozzle for the two McDonell & Samuelsen experiments.

One of the advantages of starting the flow simulations at the 25 mm position is that the sprays have already dispersed before reaching this position. This means that even using a fine grid, the total volume of liquid within a computational cell is relatively low (a maximum of 0.4% in the grids used here). This avoids the numerical problems that can occur with higher liquid fractions (see [27] for details).

A summary of the inlet boundary conditions used in the CFD simulations is given below:

- Gas velocity: experimental profiles used for axial and radial components

- Methanol vapour concentration: experimental profiles used
- Turbulent kinetic energy: calculated from experimental profiles, using $k = 0.5(\overline{u_a^2} + 2\overline{u_r^2})$, where $\overline{u_a^2}$ and $\overline{u_r^2}$ are the measured axial and radial RMS velocity fluctuations.
- Turbulent dissipation rate: calculated from $\varepsilon = c_\mu^{3/4} k^{3/2} / l_m$, where c_μ = 0.09 is the constant from the $k - \varepsilon$ model and l_m is a length scale equal to $0.0075L_{1/2}$, and $L_{1/2}$ is the spray half-width, equal to 0.0037m.
- Droplet velocities: experimental profiles used for axial and radial components
- Droplet mass fluxes: two different profiles derived from the experimental profiles tested.
- Droplet diameters: a range of approaches tested based on the experimental profiles.
- Droplet and air temperatures: 20 ˚C

More details of the inlet boundary conditions and meshes used are provided in the Appendix (Section 5.1). Only one quarter of the full 360˚ flow was modelled, using symmetry conditions for the two faces at 0˚ and 90˚ (see Figure 14). The external curved face of the domain at radius r = 156 mm was modelled as a free-slip boundary. Tests showed that increasing the domain radius by 50% to r = 234 mm had no effect on the results, confirming the domain was sufficiently wide. The outlet was treated as a simple zero-pressure boundary.

3.4 AIR-ASSISTED METHANOL SPRAY (CASE RSA02)

The methanol droplets have very little effect on the gas flow velocity for the air-assisted RSA02 spray. Instead, the flow is dominated by the momentum of the air injected through the nozzle. This is shown in Figure 16 which compares the calculated velocities at 5 axial positions with McDonell & Samuelsen's experimental data. Results from three CFD predictions are shown: with no droplets (just the air flow), with the Gaussian droplet mass-flux profile and with the scaled mass-flux profile (see Figure 11 for the inlet profiles used). Overall, there are only minor differences between the three CFD models. The maximum difference occurs at the 75 mm position, where the velocity predicted by the model with the Gaussian profile is 10% greater than that predicted by the no-droplet model. The Gaussian model consistently produces slightly higher peak velocities than the other two models. This is a consequence of the fact that it has the highest peak mass flux of the three models.

A more significant factor affecting the predicted gas flow velocity is the turbulence model treatment in the gas phase. Figure 17 shows results obtained from the two-equation k-ε and SST models and the more complex LRR differential stress model. Since the jet is far away from walls, the SST model in this case behaves essentially as a k-ω model. The vapour velocities are all generally in good agreement with the experimental measurements, the k-ε model slightly overpredicts the peak velocity at the 50, 75 and 100 mm positions by around 10% but does better with the 150 mm measurements. The SST model does the reverse, predicting the 50, 75 and 100 mm measurements well, but then underpredicting the peak velocity in the 150 mm

measurements. The LRR model produces the worst predictions of the three, overpredicting the peak velocity at all positions by up to 20%. For the remainder of the calculations shown below, the SST model has been used. It is not unexpected to see different predictions for the spreading rates of the jet with different turbulence models. For a description of the reasons for this behaviour, see for example Pope [34].

It was noted earlier that despite the CFD simulations starting from the 25 mm measurement plane, rather than at the nozzle itself, there is still a significant amount of methanol vapour produced within the CFD domain due to further droplet evaporation (see Figure 15). To demonstrate how much vapour is produced within the domain, Figure 18 compares the vapour concentration profiles produced using CFD models with and without droplet evaporation. Close to the nozzle, the two models are the same, since they use identical initial conditions at the 25 mm position (where there is a certain amount of methanol vapour already present). However, at positions further downstream the results with and without the evaporation model diverge. At the final measurement plane, 150 mm downstream from the nozzle, the peak vapour concentration is over-predicted by around 50% when the evaporation model is used, but the results without an evaporation model under-predict the peak value by nearly 60%.

Also presented in Figure 18, although not readily visible, are results from running the simulations with the Reitz-Diwakar secondary droplet breakup model. These results are practically identical to the results obtained when the breakup model was not used. For any breakup to occur, the Weber number must be greater than 12 (see Section 2.2.4). In the case considered here, the air density is $\rho \approx 1.2$ kg/m^3, the maximum droplet diameter, $D \approx 50\times10^{-6}$ m, and the surface tension, $\sigma \approx 0.0024$ N/m. The slip velocity, V, varies across the flow and is highest towards the outer edge of the spray near the CFD inlet boundary, where it reaches around 12 m/s. This gives a Weber number of:

$$We = \frac{\rho V^2 D}{\sigma} = \frac{(1.2)(12)^2\left(50\times10^{-6}\right)}{(0.0024)} \approx 3.6 \tag{39}$$

This is too low for any droplet breakup to occur, which helps to explain why the results with and without the breakup model are identical.

One of the major uncertainties in modelling industrial sprays is in characterising the droplet size distributions. The data from the McDonell & Samuelsen experiments is very detailed in this respect. At the position 25 mm downstream from the nozzle, they measured the droplet size distribution at 17 different radial measurement positions. The distribution was described in terms of the number of droplet counts within 18 size classes, ranging in size from 1 to 10 microns, 11-21 microns etc. up to 200 microns. In addition, they gave arithmetic mean and Sauter mean diameters at each of the 17 positions. The arithmetic, or numerical, mean diameter (D_{10}) is obtained from the average of the droplet diameter based on the number of droplets counted:

$$D_{10} = \int_{D_{\min}}^{D_{\max}} n(D)\,D\,dD \tag{40}$$

where $n(D)$ is the number of droplets of diameter D. The Sauter mean diameter (D_{32}) is obtained from:

$$D_{32} = \frac{\int_{D_{\min}}^{D_{\max}} D^3 n(D) dD}{\int_{D_{\min}}^{D_{\max}} D^2 n(D) dD} \tag{41}$$

The Sauter mean diameter can be thought of as representing droplets with the same volume to surface area ratio as that of the whole spray. This can be a more accurate approximation of a droplet distribution when evaporation is important.

Tests were run using different inlet conditions for the droplet diameters to see how this would affect the amount of methanol vapour produced. Figure 19 summarizes the different initial droplet diameters used in these tests. These included using:

- the full experimental distributions at each radial position (from now on, denoted D_{exp})
- the experimentally measured Sauter mean diameter, D_{32}, at each radial position
- the experimentally measured arithmetic mean diameter, D_{10}, at each radial position
- a single droplet diameter, D_{mono}, for the whole of the spray.

The value of D_{mono} was calculated from the area-weighted average of the D_{10} values. For the RSA02 case, D_{mono} = 40.7 microns. The predicted methanol vapour concentrations are compared in Figure 20. The different size distributions result in a spread in the predicted concentrations of around 50% at the final measurement plane. At this position, the experiments show a blunted profile whereas all the CFD results exhibit a rounded peak. Most of the CFD results overpredict the peak concentrations, with the D_{mono} approach being closest to the experiments. The D_{10} results exhibit the largest overprediction, a consequence of the droplet diameters being between 10% and 50% smaller than the D_{32} values. These smaller droplets with the D_{10} inlet condition evaporate more readily, and produce higher methanol concentrations. The D_{32} and D_{exp} results are relatively close, confirming that the Sauter mean diameter is a reasonably good approximation of droplet distributions for evaporating sprays. Interestingly, despite the monodisperse spray having been derived from the average of the D_{10} values it performs very differently, producing much less vapour. This suggests that the smaller droplets are important in driving the majority of evaporation.

CFD simulations were undertaken to examine the effect of turbulent dispersion on the droplets (Figure 21). The dispersion model superimposes a forcing on droplet trajectories proportional to the magnitude of the square-root of the local turbulent kinetic energy in a random direction (see Section 2.2.5). The model has relatively little effect on the RSA02 results, producing a slight increase in the vapour concentrations at the 75, 100 and 150 mm positions.

In all of the preceding results, the ‘Gaussian’ mass flux profile shown in Figure 11 was used for the inlet conditions. Figure 22 shows predictions of the vapour concentration obtained using the alternative ‘Scaled’ mass flux profile at the inlet. The Scaled model predicts an overly wide spray envelope near the nozzle that is more blunt than the experimental profile. As the spray develops further downstream, the agreement between the CFD results and experiments improves. The overall error at the final measurement position, at 150 mm, is just a few percent. The inlet mass flux profile is one of the key uncertainties in the experiments. These results show that predictions are sensitive to the type of mass flux profile adopted. The difference is most acute near the nozzle. At the furthest downstream measurement position the width of the spray envelope is similar with the two models but the peak concentration still differs by 25%.

In many practical applications, the spray inlet conditions will not be nearly so well characterized as for the McDonell & Samuelsen spray. Measurements of the initial droplet conditions may consist of only an estimated mean droplet diameter and overall mass flux. As a numerical experiment, additional CFD simulations of the RSA02 spray were made using "best-guess" conditions that were deliberately chosen to be very simple, to see how "good" or "bad" the predictions would be. A summary of the conditions is given below:

Half-cone angle	20.9º
Initial droplet diameter	28 micron
Inlet velocity	60 m/s (both air and droplets)
Inlet diameter	4.9 mm

The values used have been selected based on the experimental data but no tuning of the parameters has been undertaken to try to improve the predictions. Droplets were injected from the nozzle itself, rather than at the 25 mm measurement plane. Figures 23 and 24 show the results for the axial velocity and vapour concentrations. The simple 'best-guess' model performs surprisingly well. The axial velocities are predicted with a comparable degree of accuracy as for the previously-adopted approach based on the experimental measurements. The predicted vapour concentration is less well predicted close to the nozzle, producing a distribution with two distinct peaks at the 25 mm position where in the experiments there was just a single peak on the centreline. Further away from the nozzle, however, the 'best-guess' conditions produce a blunted profile which is similar in shape to the experiments, although the peak is underpredicted by 25%. These results seem to indicate that a relatively coarse approximation of the inlet boundary conditions can produce reasonable CFD predictions for evaporating sprays. However, it may have been just a fortunate choice of parameters in this case that gave such good agreement with the experiments.

The motivation for undertaking this validation study is to investigate how well CFD models predict the development of vapour clouds produced by evaporating sprays of volatile liquids. In this context, the most important parameter to predict well is the vapour flux. Figure 25 compares the predicted volume fluxes of methanol against the experiments for the range of cases tested. In each case, the flux Q_c has been calculated from:

$$Q_c = \int_A (X_c U) dA \tag{42}$$

where X_c is the molar fraction of methanol vapour, U the axial velocity and A the total cross-sectional area of the spray. The results shown in Figure 25 comparing the different drop size distributions used the Gaussian mass flux profile without a dispersion model in all cases. For the turbulent dispersion comparisons, the D_{exp} size distribution was used with a Gaussian mass flux profile. For the mass flux profile comparison, the D_{exp} size distribution is used with the turbulent dispersion model.

In the experiments, the volume flux increases almost linearly with distance from the nozzle (see also Figure 15). All the CFD predictions tend to show slightly non-linear behaviour, with a relative steep initial increase of volume flux with distance, followed by a more gentle increase further away from the nozzle. In all cases, this has the effect that the volume flux nearest the nozzle is slightly overpredicted whilst at the final measurement position further downstream it is underpredicted. The spread in values at the final 150 mm measurement position is around 25% with different inlet droplet size distributions. The most physically representative size distribution, D_{exp}, underpredicts the measured flux by around 20%.

The turbulent dispersion model which only appeared to have a relatively minor influence in the concentration profiles (Figure 21), does affect the total vapour flux. The difference between results with and without the dispersion model is around 15% at the 150 mm position. Results obtained with the dispersion model are closer to the experiments.

Changing the inlet droplet mass flux profile was shown to have a significant effect on the vapour concentration profiles (Figure 22). However, it has only a relatively small effect on the integrated vapour flux (Figure 25).

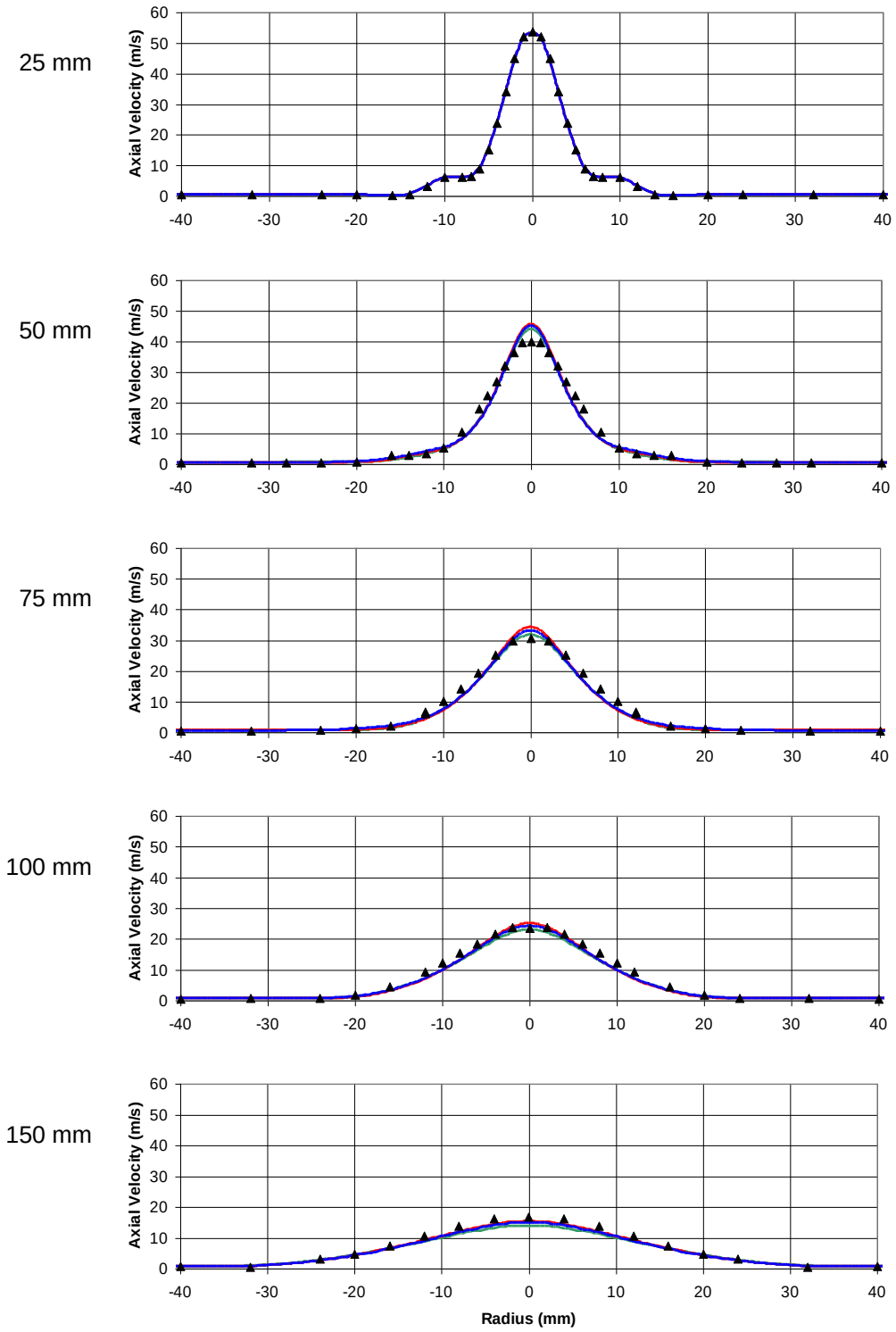

Figure 16 Comparison of gas velocity profiles for the RSA02 spray: — without any droplets modelled; — with droplets modelled using Gaussian mass flux profile; — with droplets modelled using scaled experimental mass flux profile; ▲ McDonell & Samuelsen experiments.

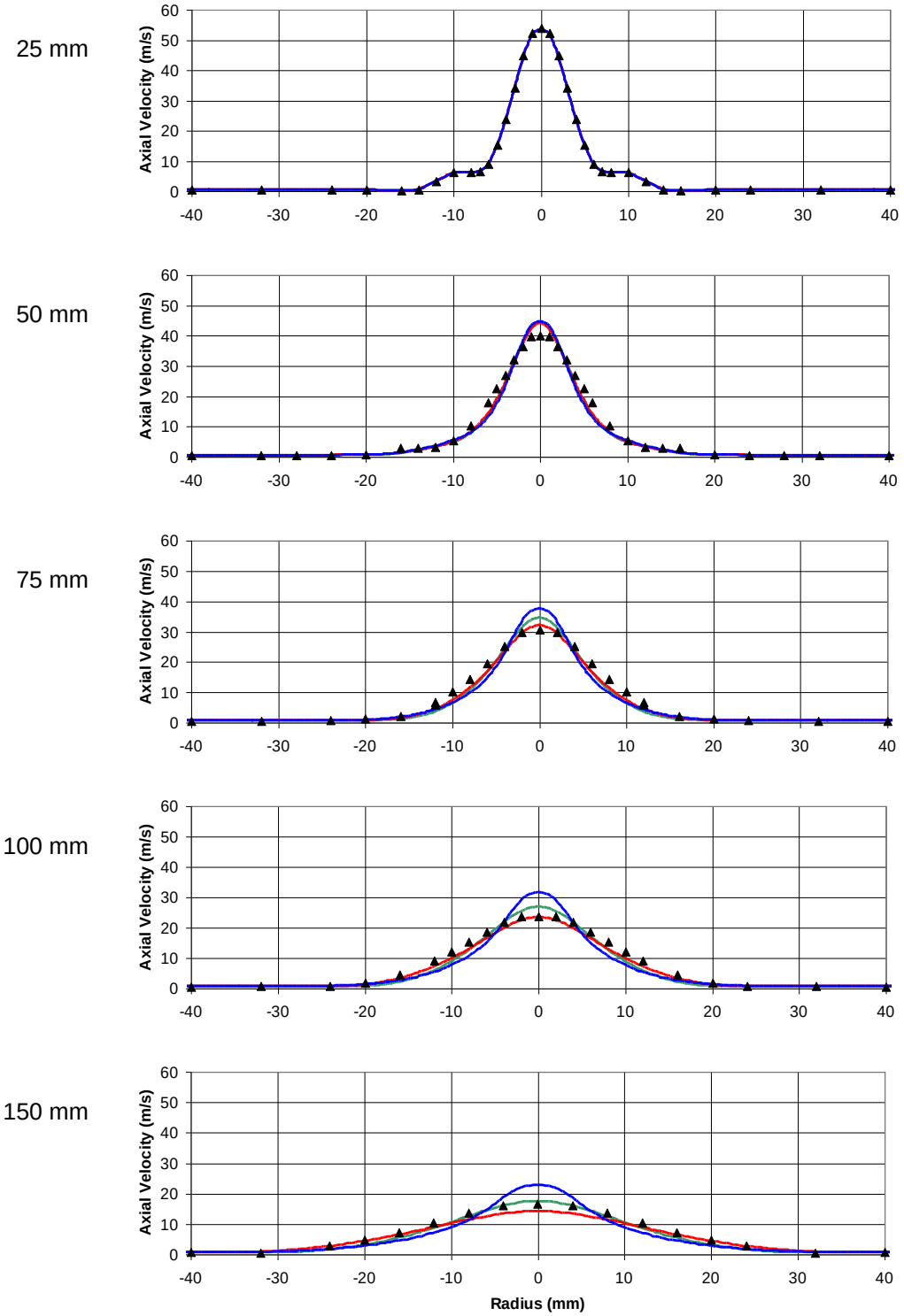

Figure 17 Predicted gas velocity profiles for the RSA02 spray with three different turbulence models: — *k-ε*; — SST; — LRR; ▲ McDonell & Samuelsen experiments.

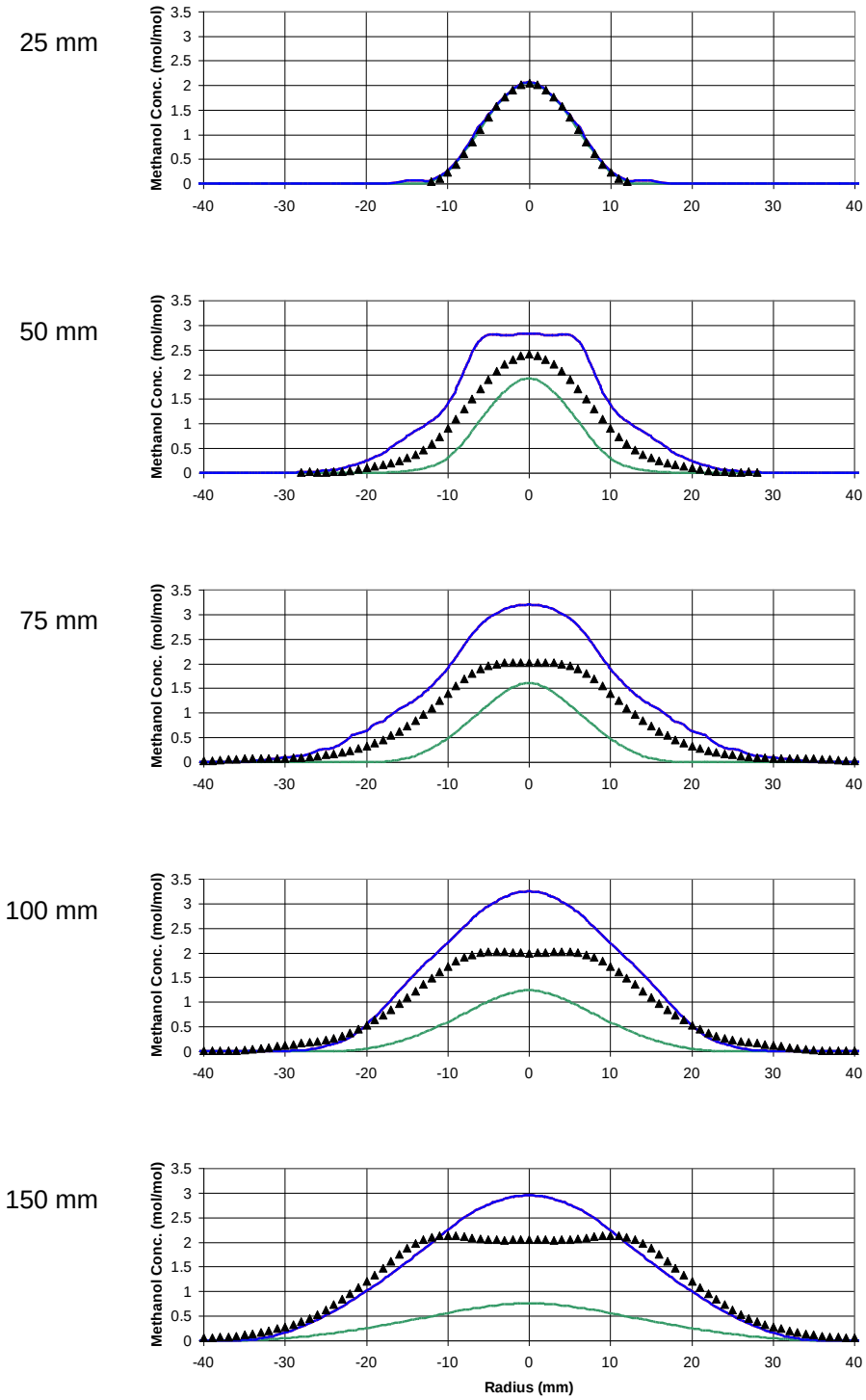

Figure 18 Predicted methanol vapour concentration profiles for the RSA02 spray: — without any evaporation modelled; — with evaporation but without breakup; — with evaporation and with breakup (the red and blue lines fall on top of one another); ▲ McDonell & Samuelsen experiments.

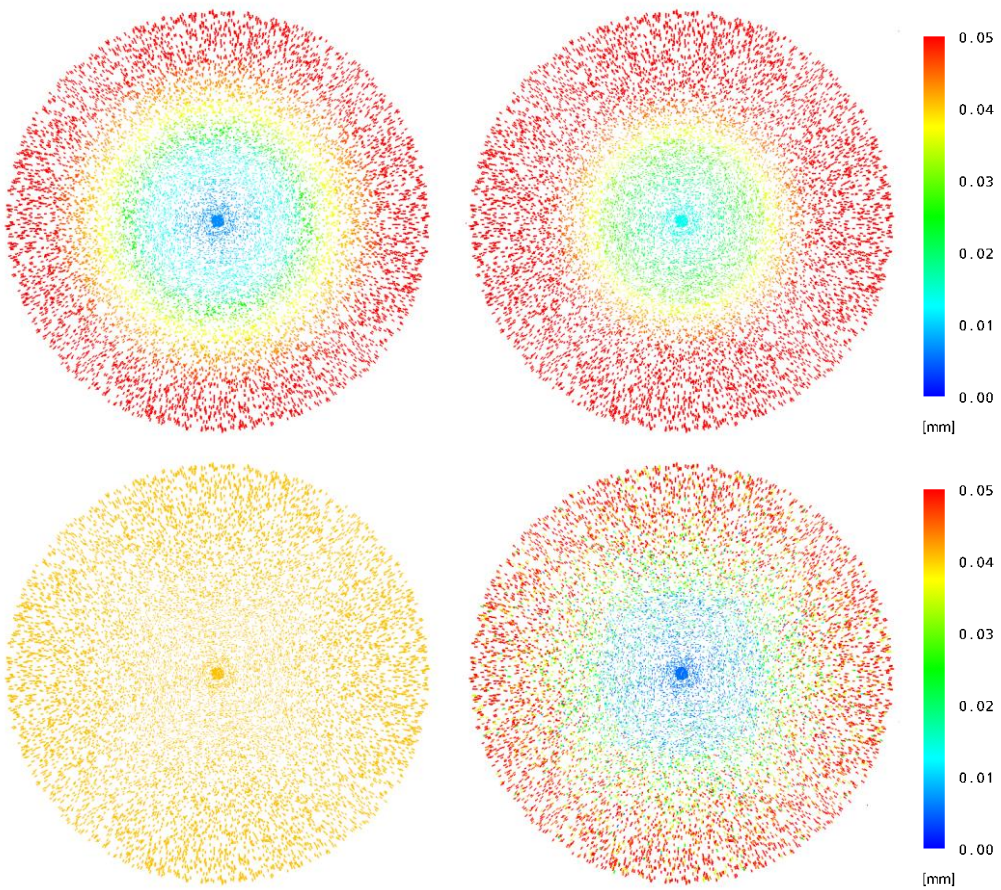

Figure 19 Initial droplet diameters used in the CFD simulations for the RSA02 case: D_{10}, D_{32}, D_{exp} and D_{mono} size distributions (clockwise from the top-left). Each coloured dot represents a computational particle and all particles are shown. Each ¼ model has been copied three times to produce the 360˚ view.

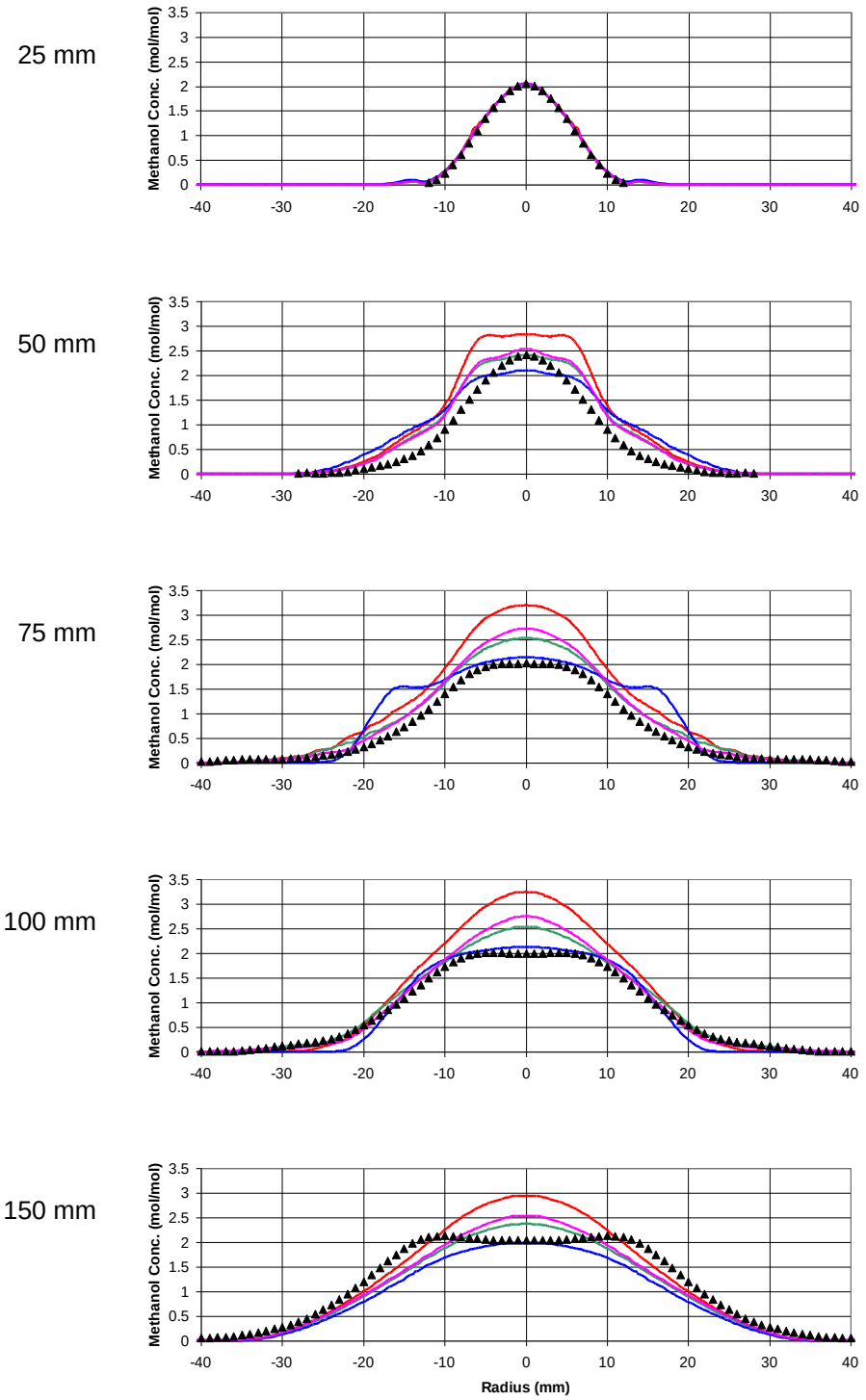

Figure 20 Predicted methanol vapour concentration profiles for the RSA02 spray with different initial droplet sizes: — D_{mono}, — D_{32}; — D_{10}; — D_{exp}; ▲ McDonell & Samuelsen experiments. In all cases, the Gaussian mass flux profile has been used and a turbulent dispersion model has not been used.

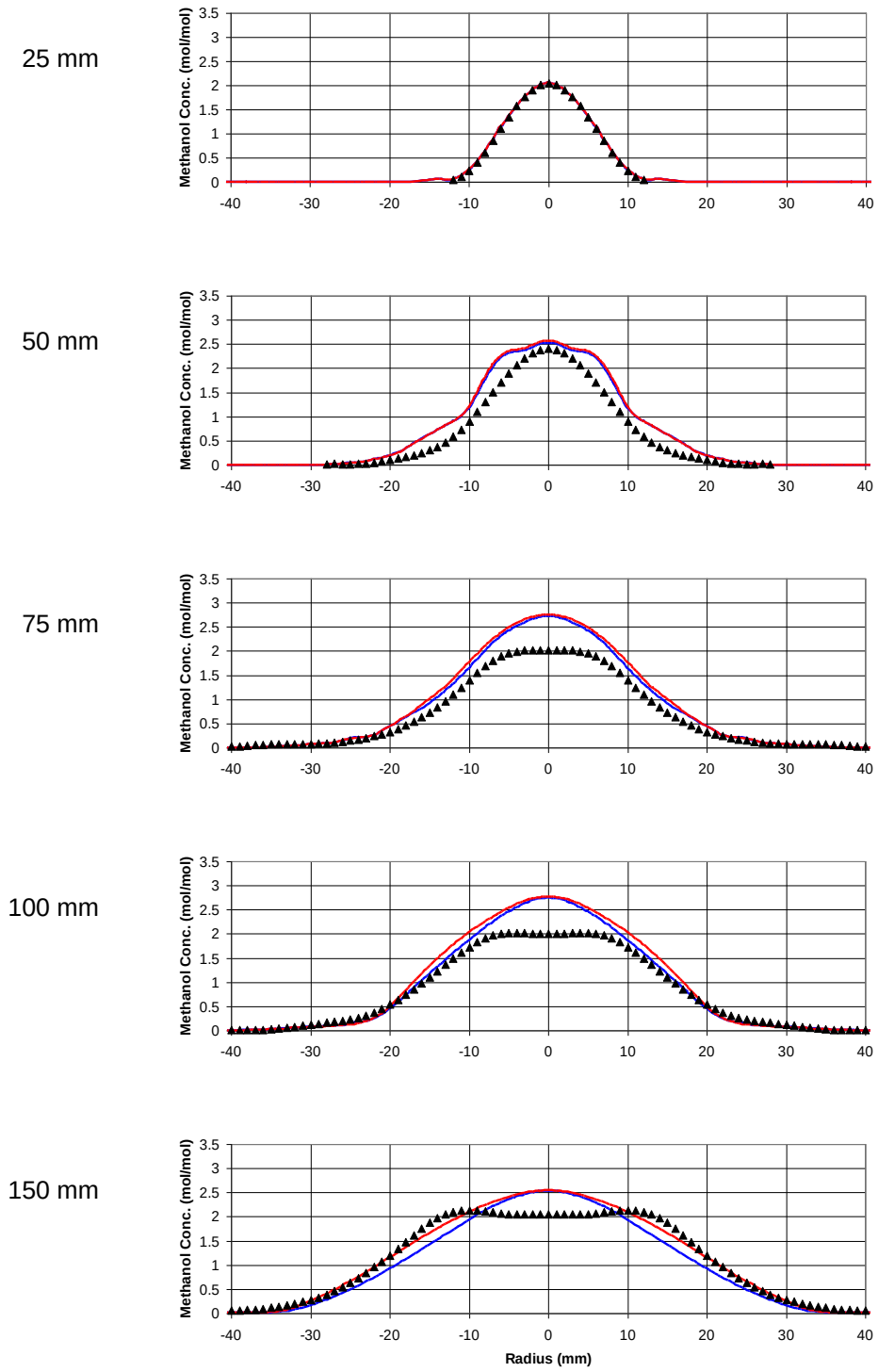

Figure 21 Predicted vapour concentrations for the RSA02 spray using different droplet models: — with turbulent dispersion; — without turbulent dispersion; ▲ McDonell & Samuelsen experiments. In both cases, the Gaussian mass flux profile and the D_{exp} droplet size distribution has been used.

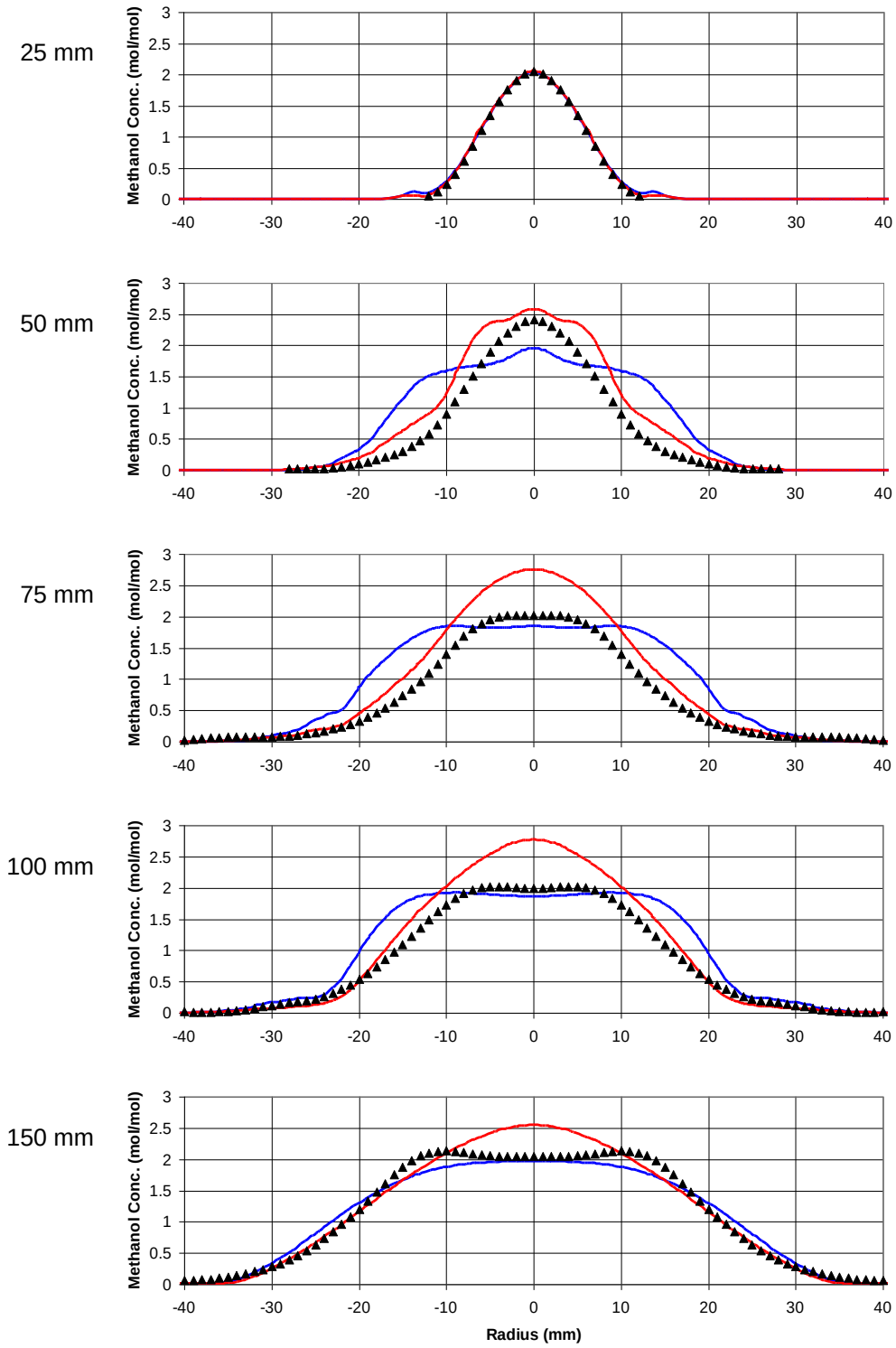

Figure 22 Predicted vapour concentrations for the RSA02 spray with different inlet conditions for the droplet mass flux: — Scaled, — Gaussian profile; ▲ McDonell & Samuelsen experiments. See Figure 11 for details of profiles used. Both models used the D_{exp} droplet size distribution with a turbulent dispersion model.

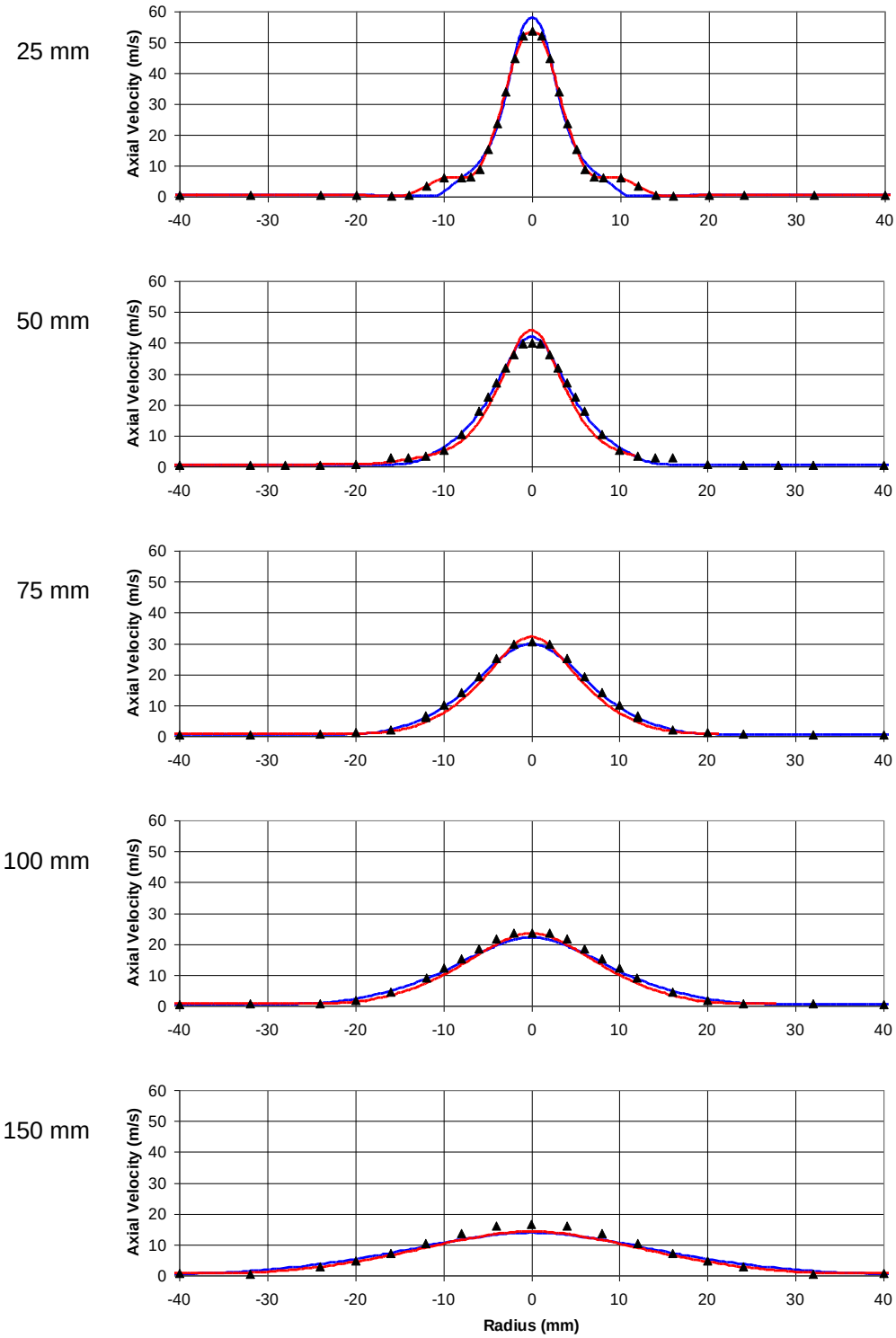

Figure 23 Predicted vapour velocity profiles for the RSA02 spray with different inlet conditions: — using experimental data; — using a 'best-guess' with no tuning; ▲ McDonell & Samuelsen experiments.

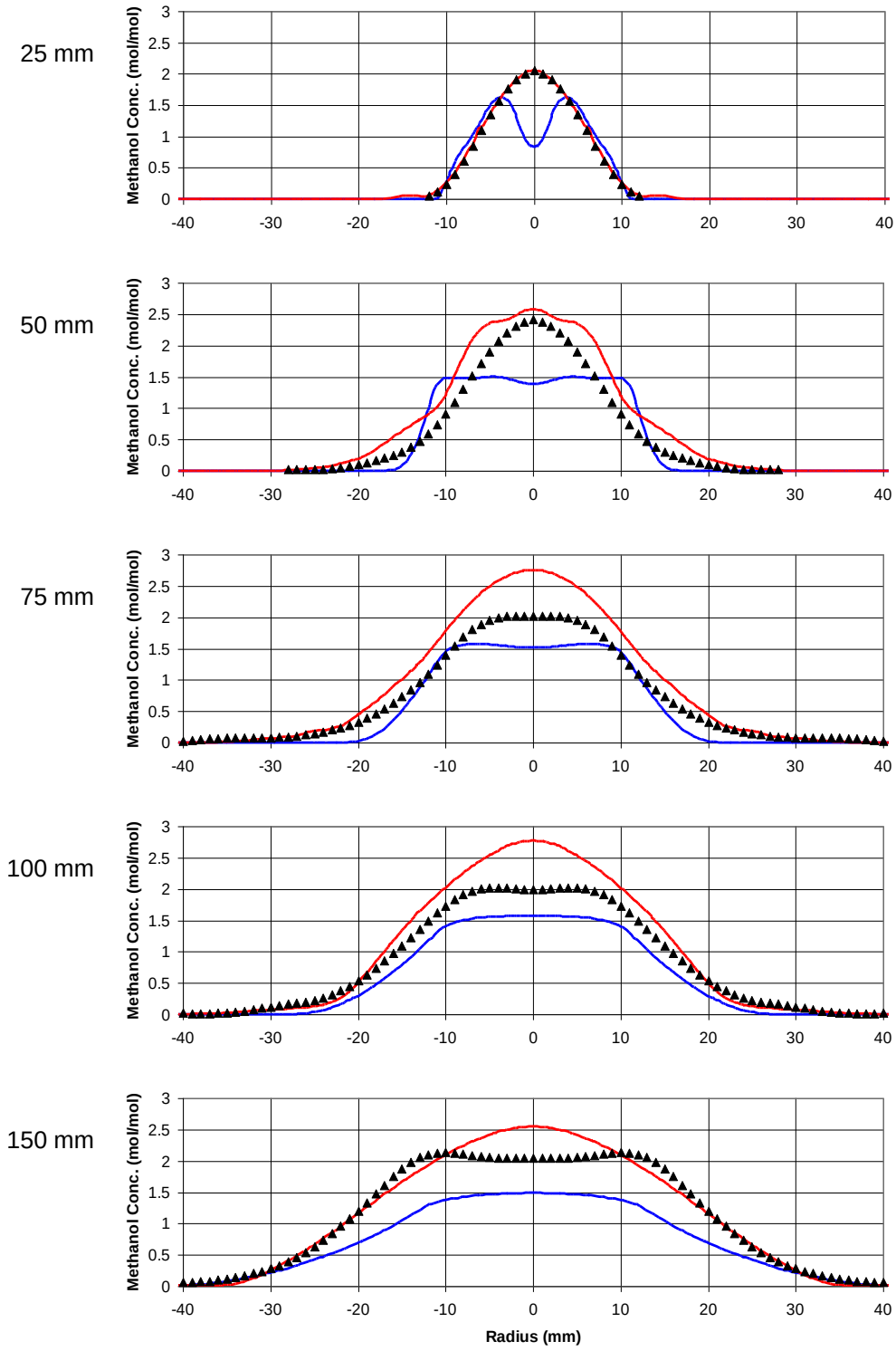

Figure 24 Predicted vapour concentrations for the RSA02 spray with different inlet conditions: — using experimental data; — using a 'best-guess' with no tuning; ▲ McDonell & Samuelsen experiments.

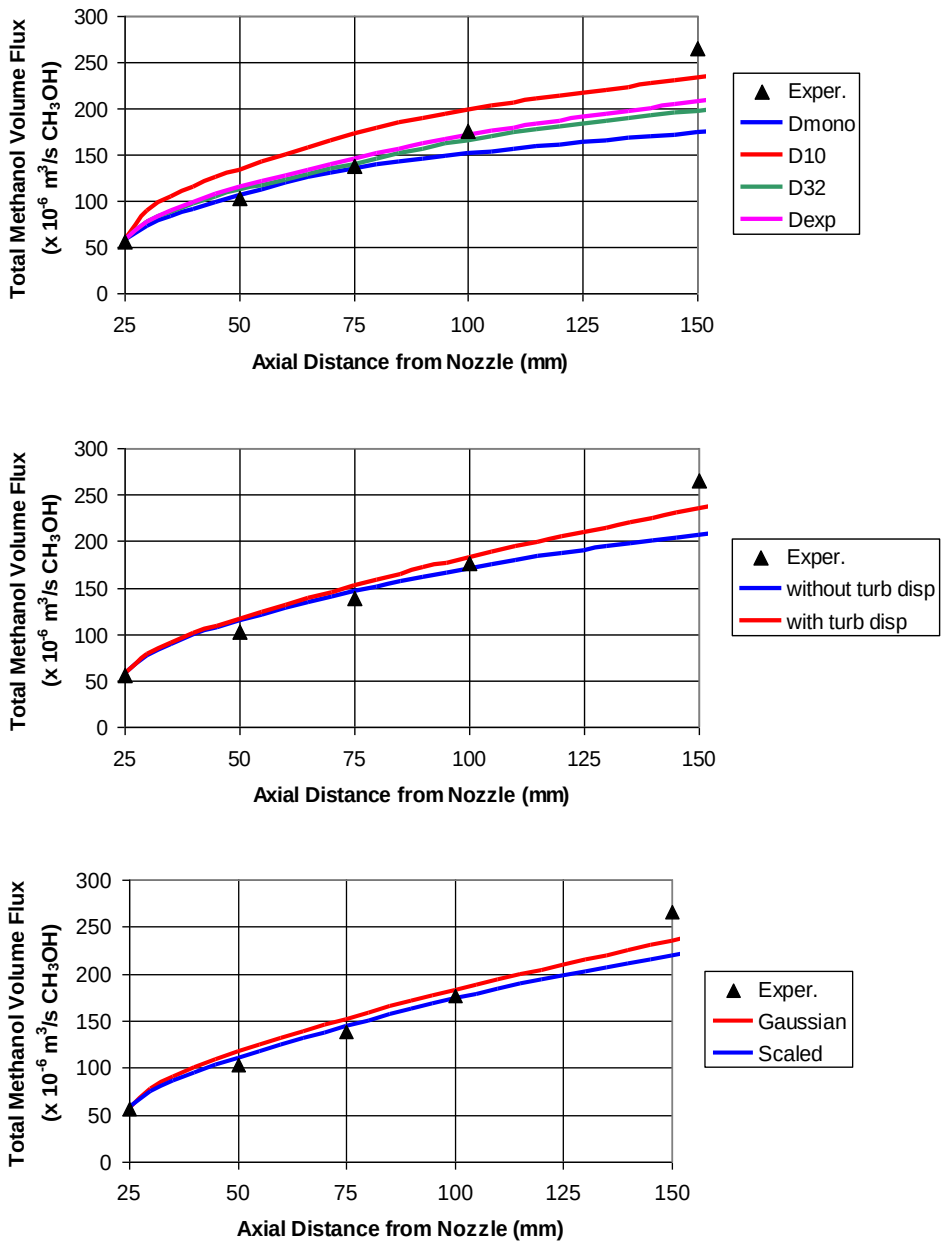

Figure 25 Predicted total volume fluxes of methanol vapour for the RSA02 spray. Three comparisons are shown: the effect of changing the drop size (top), the turbulent dispersion model (middle) and the mass flux profile (bottom).

3.5 NON-AIR-ASSISTED METHANOL SPRAY (CASE RSA01)

The non-air-assisted spray (RSA01) presents a much greater challenge for CFD than the previous case examined since the flow is entirely driven by the spray of droplets. As before, for the previous air-assisted case, a number of simulations have been performed to examine the sensitivity of the predictions to changes in the droplet size distribution, mass flux profile and other model conditions.

Four different inlet droplet size distributions were tested: D_{exp}, D_{32}, D_{10} and D_{mono} (see Figure 26). For an explanation of the meaning of each of these distributions, see the previous Section. The value of D_{mono} was 39.6 microns for the RSA01 case. The predicted axial gas velocities are shown in Figure 27. The CFD predictions diverge rapidly from the experimental profiles. Even at 35 mm, just 10 mm from the inlet plane, the peak velocity is underpredicted by 25% by all models and there is a secondary, smaller peak at $r \approx 25$ mm in the CFD profiles which does not appear in the experiments.

The slight disagreement between the CFD results and experimental profiles at the 25 mm plane for radial positions greater than $r = 30$ mm (the top graph in Figure 26) is due to the fact that the experimental data was only used to set the inlet conditions in the bulk of the flow ($0 < r < 30$ mm). In the peripheral region ($r > 40$ mm) the axial velocity was set to the constant coflow velocity of 0.8 m/s. Additional tests, not shown here, have been undertaken using the experimental velocity measurements for the full width ($0 < r < 80$ mm) to set the CFD inlet conditions. This was found to have only a minor effect on the predicted velocity field and practically no effect on the predicted methanol vapour concentrations.

One of the notable features of the experimental velocity profile used for the CFD inlet conditions for the RSA01 case at the 25 mm measurement position is a secondary peak in the velocity at radius $r = 20$ mm. This peak does not appear in the measurements at 35 mm. It is possible that the secondary peak in the experiments at 25 mm was in fact an incorrect reading, and that it was responsible for the erroneous secondary peak appearing in the CFD results further downstream. To test this hypothesis, a different inlet profile was tested in which the secondary peak was removed (see Figure 28). This had some limited effect in reducing the size of the secondary peak, but the predicted shape of the velocity profiles remained incorrect.

The previous tests with the air-assisted spray showed that the inlet profile adopted for the droplet mass flux could have a significant effect on the flow development. In the previous results (Figures 27 and 28) the 'Scaled' mass flux profile was used. Figure 29 shows the effect of changing the mass flux profile, using two different Gaussian profiles instead of simply scaling the experimental value (for details of the profile used, see Figure 12). Using either of the Gaussian profiles has a measurable effect on the velocity profiles. The secondary peaks are less pronounced and the centreline peak velocity increases slightly so that at the final measurement plane (100 mm) it is in slightly better agreement with the experiments than the original 'Scaled' profile. Nevertheless, the CFD models predict a peak velocity occurring on the centreline whereas the experiments have a localised velocity minima on the centreline at the 75 mm and 100 mm positions.

As found previously for the RSA02 case, the droplet breakup models have no effect in the non-air-assisted spray since the droplets have an initial size that is sufficiently small to be aerodynamically stable (i.e. the Weber number is less than 12). Results obtained using the Reitz-Diwakar breakup model are not shown here.

Since the velocity field is not calculated well using the experimental data for inlet boundary conditions, it seems unlikely that the CFD model will be able to predict the correct vapour concentrations. The velocity field controls the convection of methanol vapour and the concentration of methanol vapour affects the evaporation rates of the droplets. To see how well the vapour concentrations are predicted, Figure 30 compares the results obtained using various different inlet droplet size distributions. The peak concentration on the centreline is predicted surprisingly well with all the models, a maximum error of around 10%. The shape of the concentration profile away from the centreline is less well predicted, however, with a large spread in values towards the edge of the spray. At a radial position of 30 mm, the spread in predicted concentrations is of similar size as the absolute value of the concentration. The results obtained using the most detailed droplet size distribution, D_{exp}, were closest to the experiments, predicting the maximum width of the concentration profile to within a few percent but overpredicting the concentrations on the periphery of the spray.

The fact that all the profiles for different size distributions all collapse together in the centre of the spray could indicate that the vapour concentration reached equilibrium conditions, i.e. the vapour was fully saturated so that no further evaporation could take place. The droplet temperatures in the RSA01 spray fell to just below -9ºC at the edge of the spray (Figure 31). The saturation vapour pressure of methanol is 0.022 bar at -9ºC, hence the saturation concentration is around 2% mol/mol. This is of similar magnitude to the concentrations found in the spray. To show how close the vapour concentration was to the saturation condition, Figure 31 plots the ratio of the vapour mole fraction, X_A, to the local saturation mole fraction, X_A^{sat}:

$$\varphi = \frac{X_A}{X_A^{sat}} = \frac{X_A}{P_A^{sat} / P^{amb}} \tag{43}$$

where P^{amb} is the ambient pressure (101325 Pa), and P_A^{sat} is the saturation vapour pressure calculated from Antoine's equation using the local droplet temperature. A value of $\varphi = 1$ would indicate that the vapour is saturated and $\varphi = 0$ that there is no vapour present. Figure 32 shows that in the core of the spray, the concentration ratio reached $\varphi = 0.75$, suggesting that the vapour was not fully saturated. This does not therefore seem to explain the behaviour shown in Figure 29, where all different inlet droplet size distributions gave similar centreline vapour concentrations[4].

It was shown earlier that using the 'Gaussian' droplet mass flux profile instead of the 'Scaled' profile improved the prediction of the vapour velocity (Figures 29). It might therefore be expected to lead to improvements in the vapour concentration profiles. Figure 33 compares the predicted concentrations using the three different mass flux profiles shown in Figure 12. Results are significantly worse in the core of the spray using the Gaussian profiles with the peak concentrations overpredicted by nearly 50%[5].

Results are shown in Figure 34 for the predicted vapour concentrations with and without a droplet turbulent dispersion model. The effect of the dispersion model is even smaller in the

[4] The scattered red dots in Figure 31 appear to be related to the interpolation used to map from Lagrangian droplet temperatures to the Eulerian grid and is probably unphysical.

[5] The disparity between the Gaussian CFD results and the experimental profiles at the inlet plane in Figure 32 (the 25 mm position) is unexpected. This could be due to very rapid evaporation in the first grid cell or numerical instability due to the high droplet loading. On the inlet plane, the volume fraction of the cell occupied by droplets approached 1%.

RSA01 case than for the previous RSA02 case, leading to an increase in the width of the spray of just a few percent. The reason for the smaller effect in the RSA01 spray is shown in Figure 35, which plots the predicted turbulence intensity. The high-velocity RSA02 spray has significantly higher turbulence intensity, especially on the periphery of the spray, which leads to more significant turbulent dispersion effects than in the RSA01 spray.

CFD predictions of the total volume flux of methanol vapour for the RSA01 case are shown in Figure 36. Results shown comparing the different drop size distributions used the 'Scaled' mass flux profile without a dispersion model in all cases. For the turbulent dispersion comparisons, the D_{10} size distribution was used with a 'Scaled' mass flux profile. For the mass flux profile comparison, the D_{exp} size distribution was used without the turbulent dispersion model.

The measured fluxes increased non-linearly with distance from the nozzle – tending to increase faster further away from the nozzle. None of the CFD results exhibit this behaviour. In all cases, the CFD models overpredict the vapour flux near the nozzle and underpredict the final measurement at the 100 mm position. The different initial droplet size distributions produce a spread in the predicted vapour flux of around 20%. The best overall agreement with the measurements is obtained with the D_{32} and D_{exp} distributions. The middle graph in Figure 36 shows that the droplet turbulent dispersion model only has a minor affect on the fluxes, confirming the earlier observations (Figure 34). Also in agreement with earlier observations, the two Gaussian mass flux profiles are shown to produce excessively large vapour fluxes near the nozzle, overpredicting the vapour flux by around 25%.

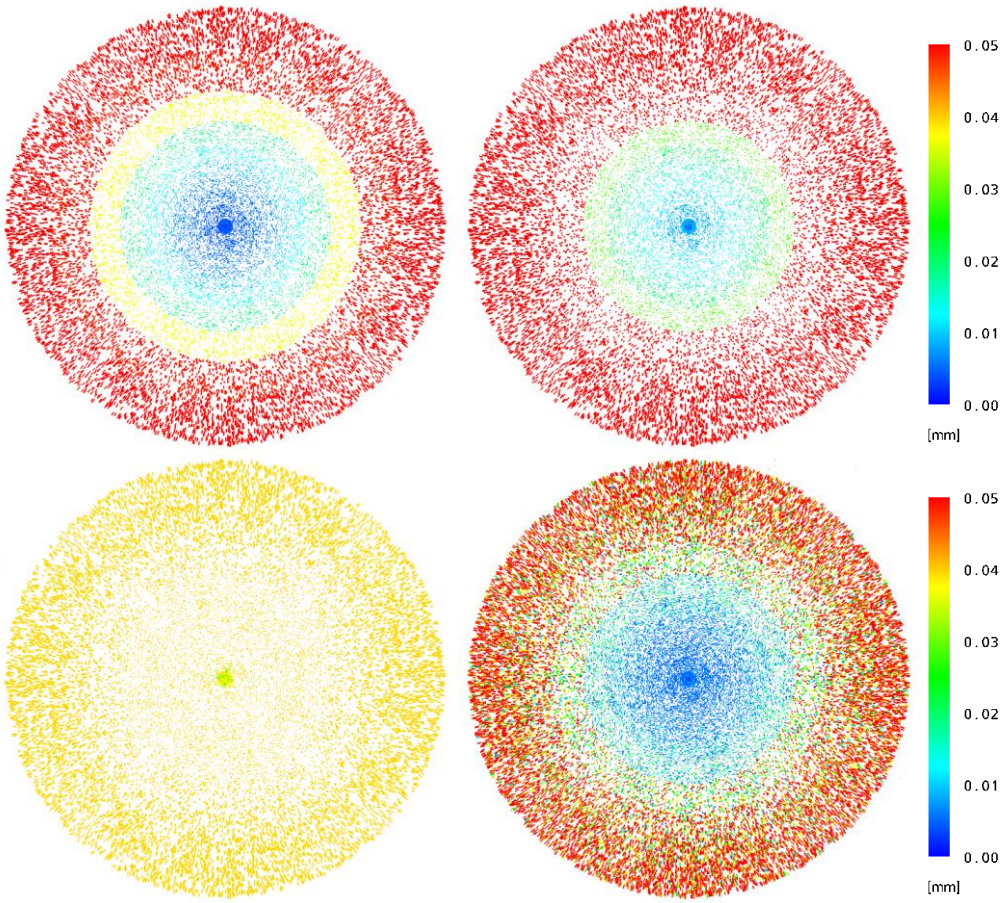

Figure 26 Initial droplet diameters used in the CFD simulations for the RSA01 case: D_{10}, D_{32}, D_{exp} and D_{mono} size distributions (clockwise from the top-left). Each coloured dot represents a computational particle and all particles are shown. Each ¼ model has been copied three times to produce the 360˚ view.

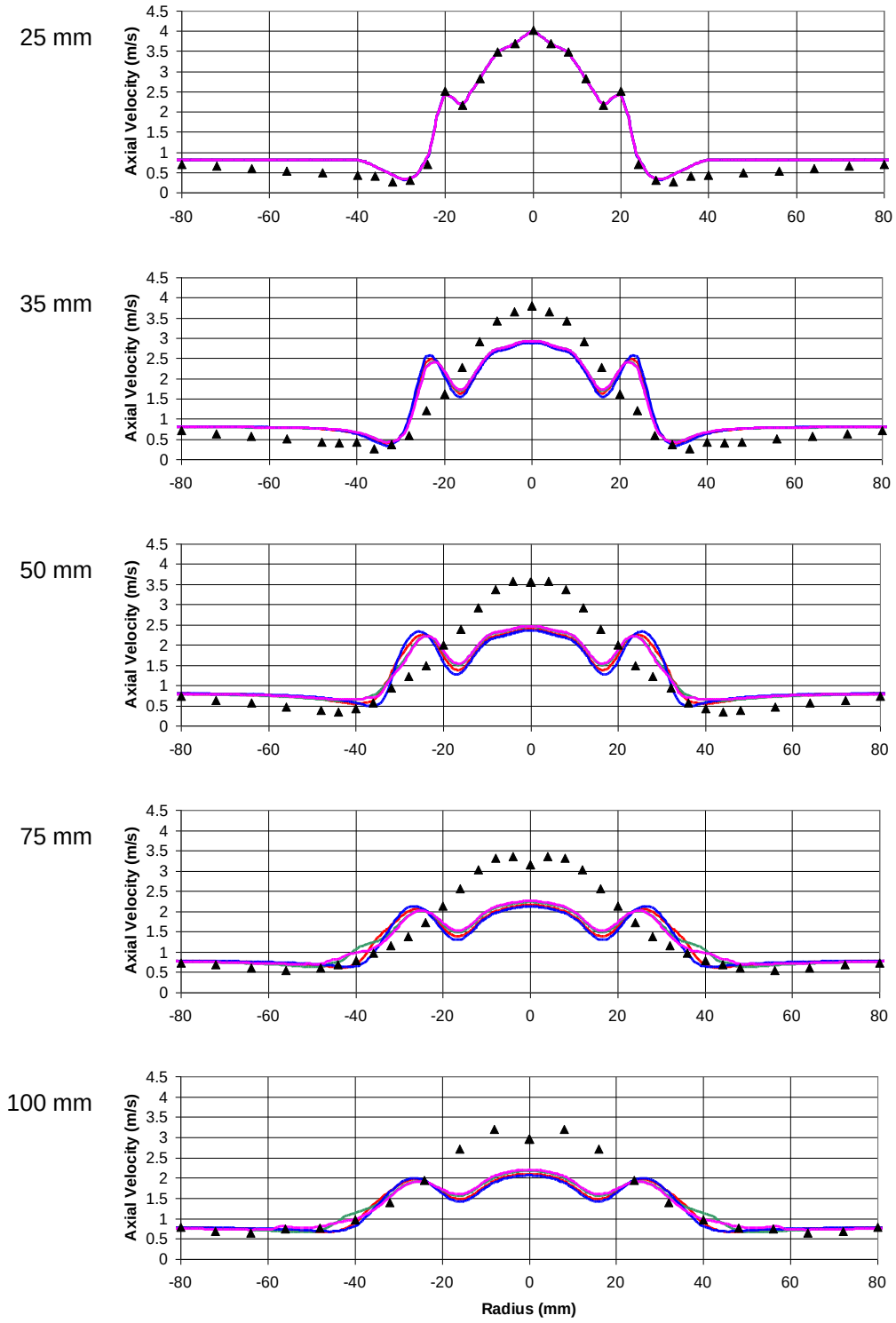

Figure 27 Predicted axial gas velocity profiles for the RSA01 spray with different initial droplet sizes: — D_{mono}, — D_{32}; — D_{10}; — D_{exp}; ▲ McDonell & Samuelsen experiments. In all cases, the 'Scaled' droplet mass flux profile was used without a droplet turbulent dispersion model.

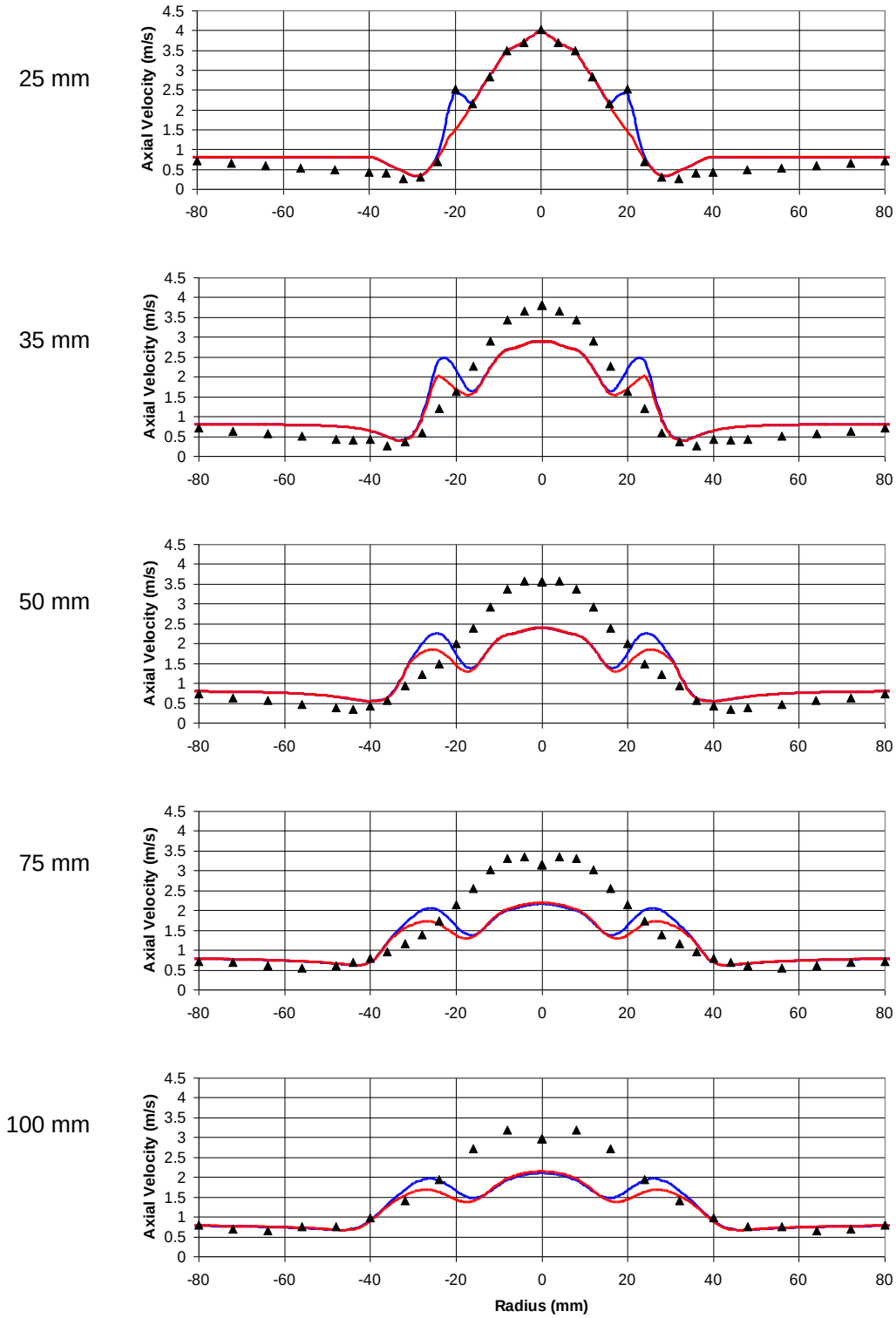

Figure 28 Predicted axial gas velocity profiles for the RSA01 spray with different inlet conditions for the gas velocity: — experimental measurement at r = 20 mm neglected; — original experimental profile; ▲ McDonell & Samuelsen experiments.

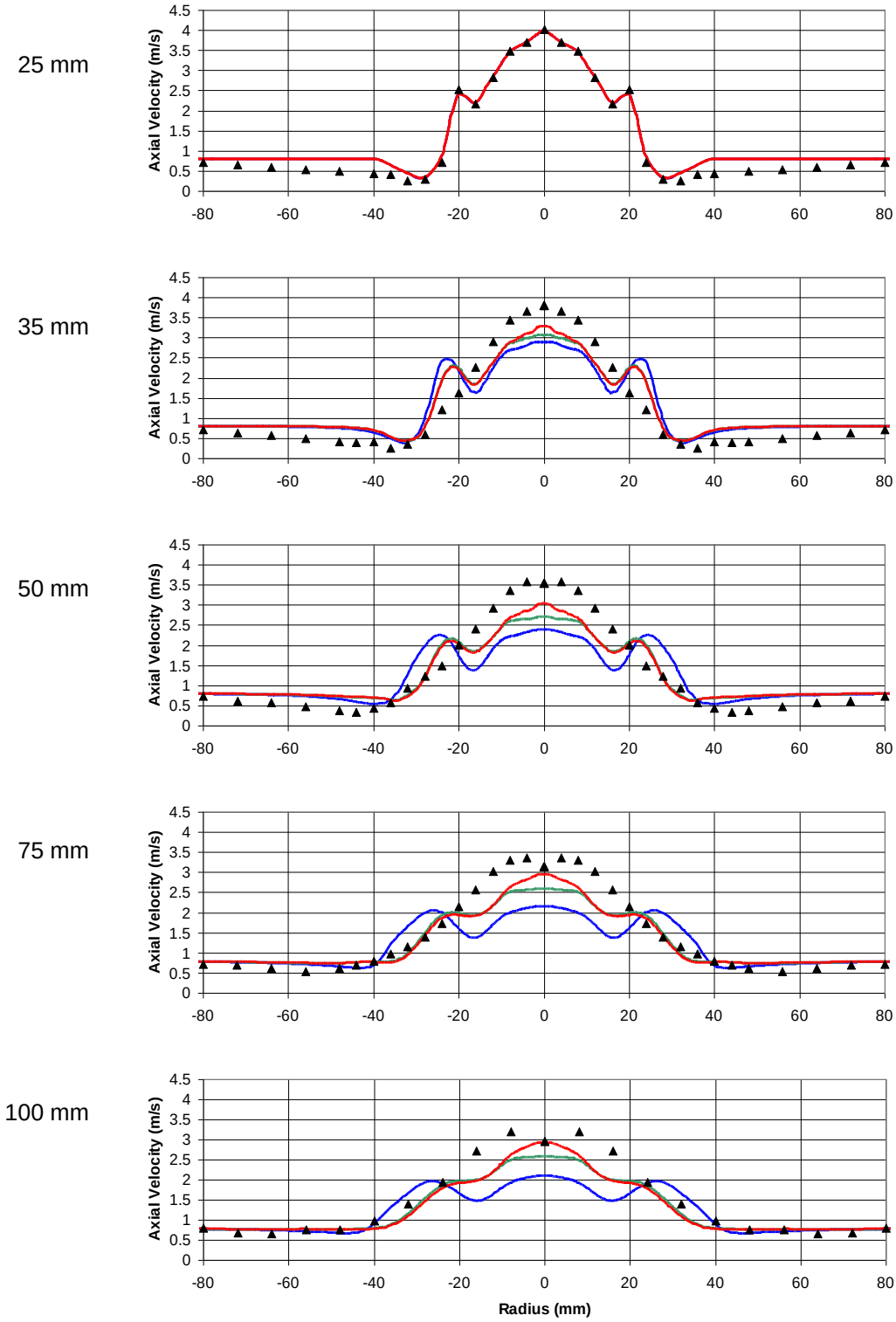

Figure 29 Predicted axial gas velocity profiles for the RSA01 spray with different inlet conditions for the droplet mass flux: — Scaled, — Gaussian A, — Gaussian B profiles; ▲ McDonell & Samuelsen experiments. See Figure 12 for details of profiles used.

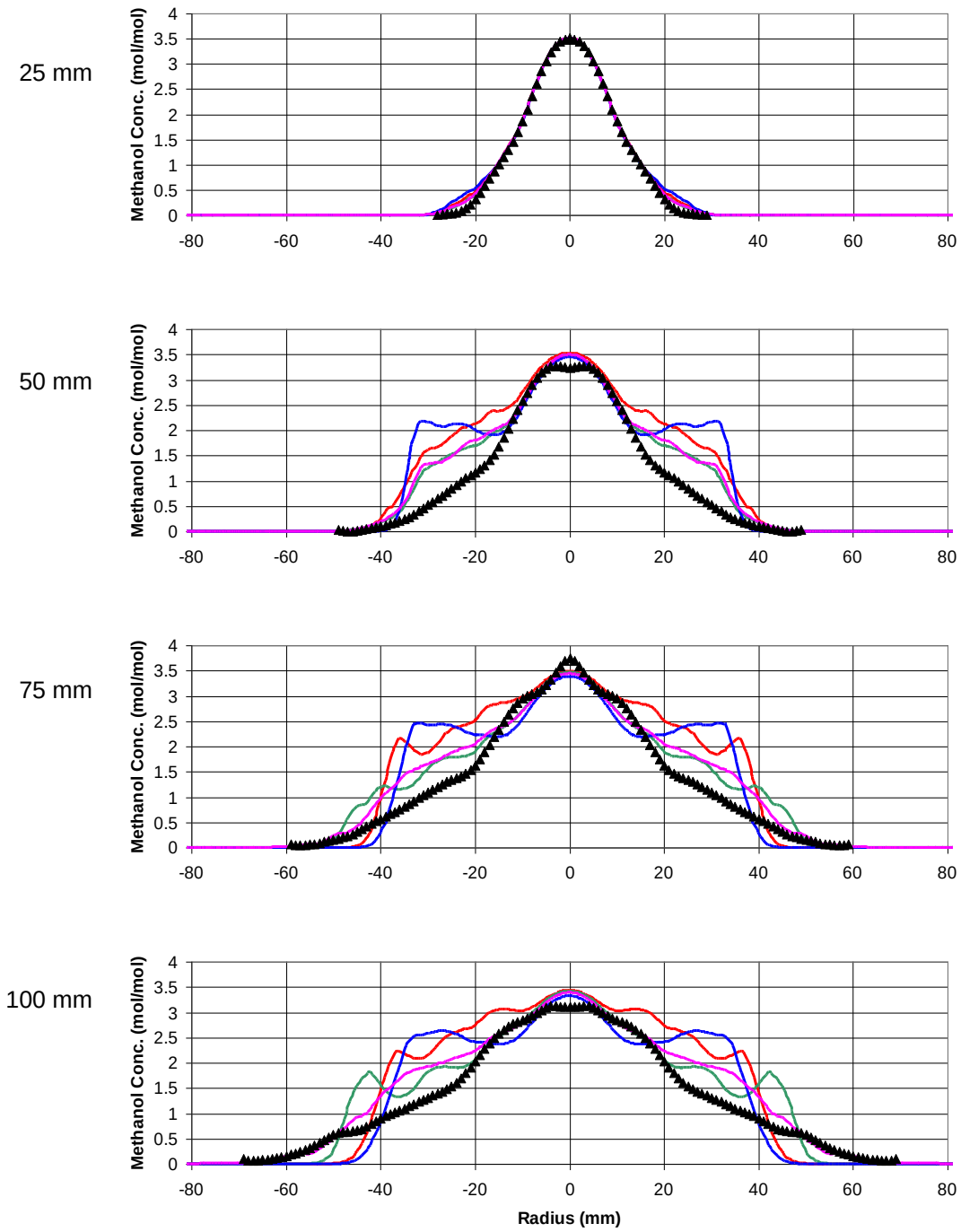

Figure 30 Predicted vapour concentrations for the RSA01 spray with different initial droplet sizes: — D_{mono}, — D_{32}; — D_{10}; — D_{exp}; ▲ McDonell & Samuelsen experiments In all cases, the 'Scaled' droplet mass flux profile was used without a droplet turbulent dispersion model.

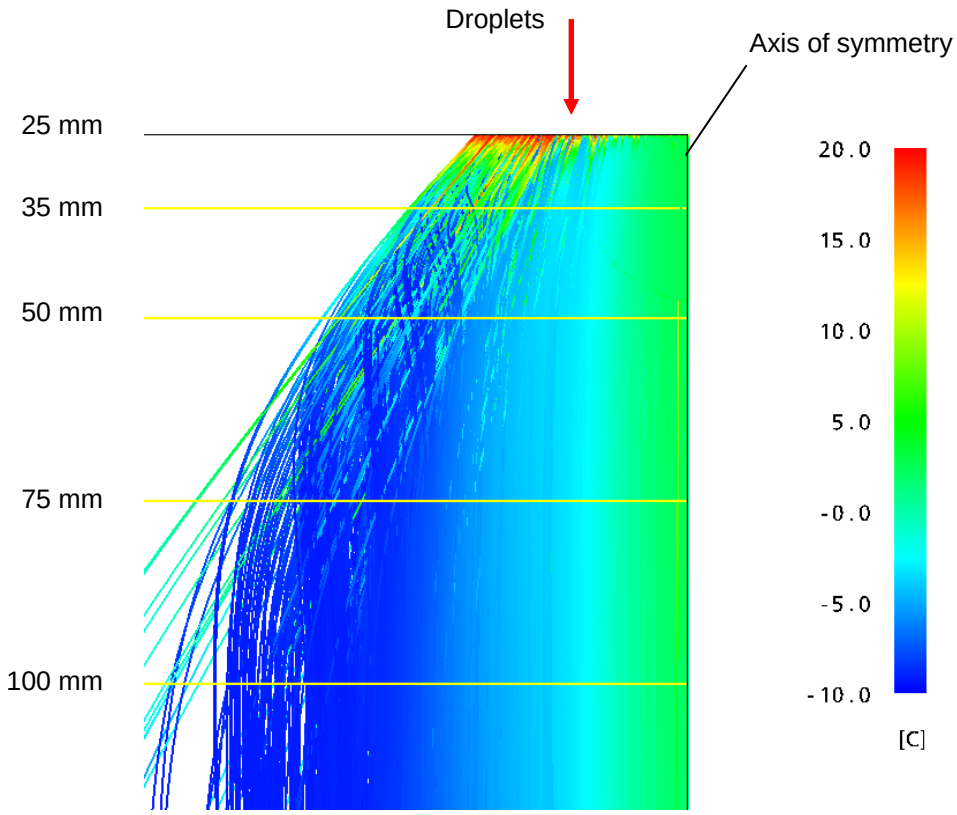

Figure 31 Particle trajectories coloured with their temperature using the D_{exp} droplet diameter distribution and the 'scaled' mass flux profile at the inlet. Yellow lines show the position of the 35, 50, 75 and 100 mm measurement positions.

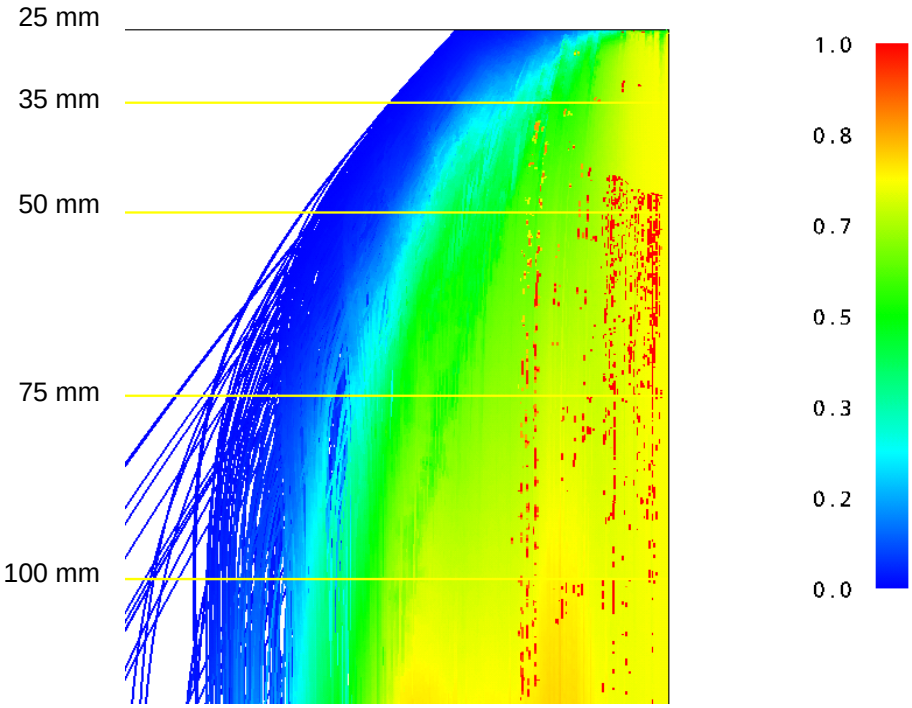

Figure 32 Particle trajectories coloured with the ratio of the local vapour concentration to the local saturation concentration. A value of 1 indicates that the vapour is fully saturated and no further evaporation can take place, a value of 0 indicates that there is no vapour present.

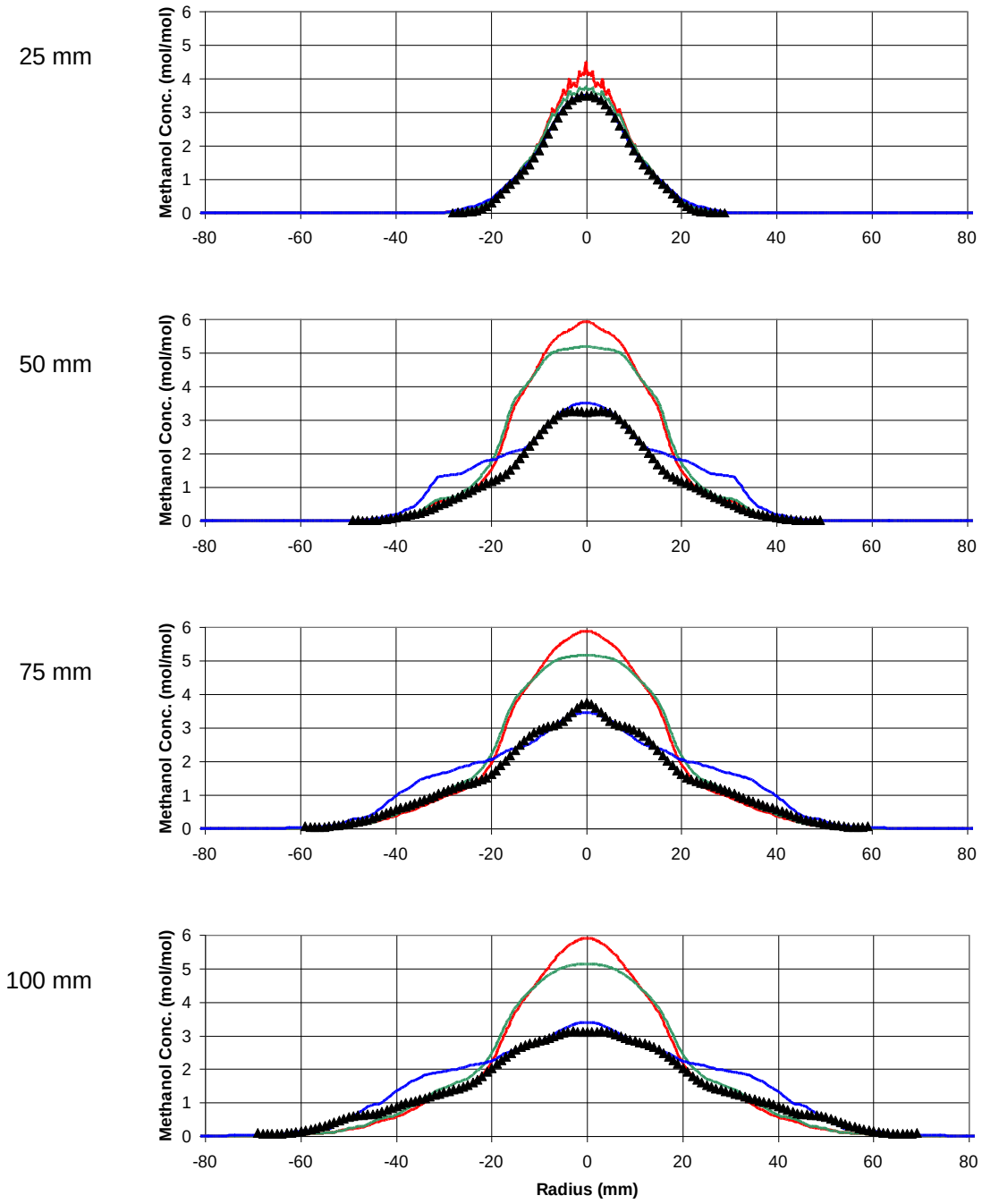

Figure 33 Predicted methanol concentration profiles for the RSA01 spray with different inlet conditions for the droplet mass flux: — Scaled, — Gaussian A, — Gaussian B profiles; ▲ McDonell & Samuelsen experiments. In all cases, the D_{exp} droplet size distribution was used without a turbulent dispersion model.

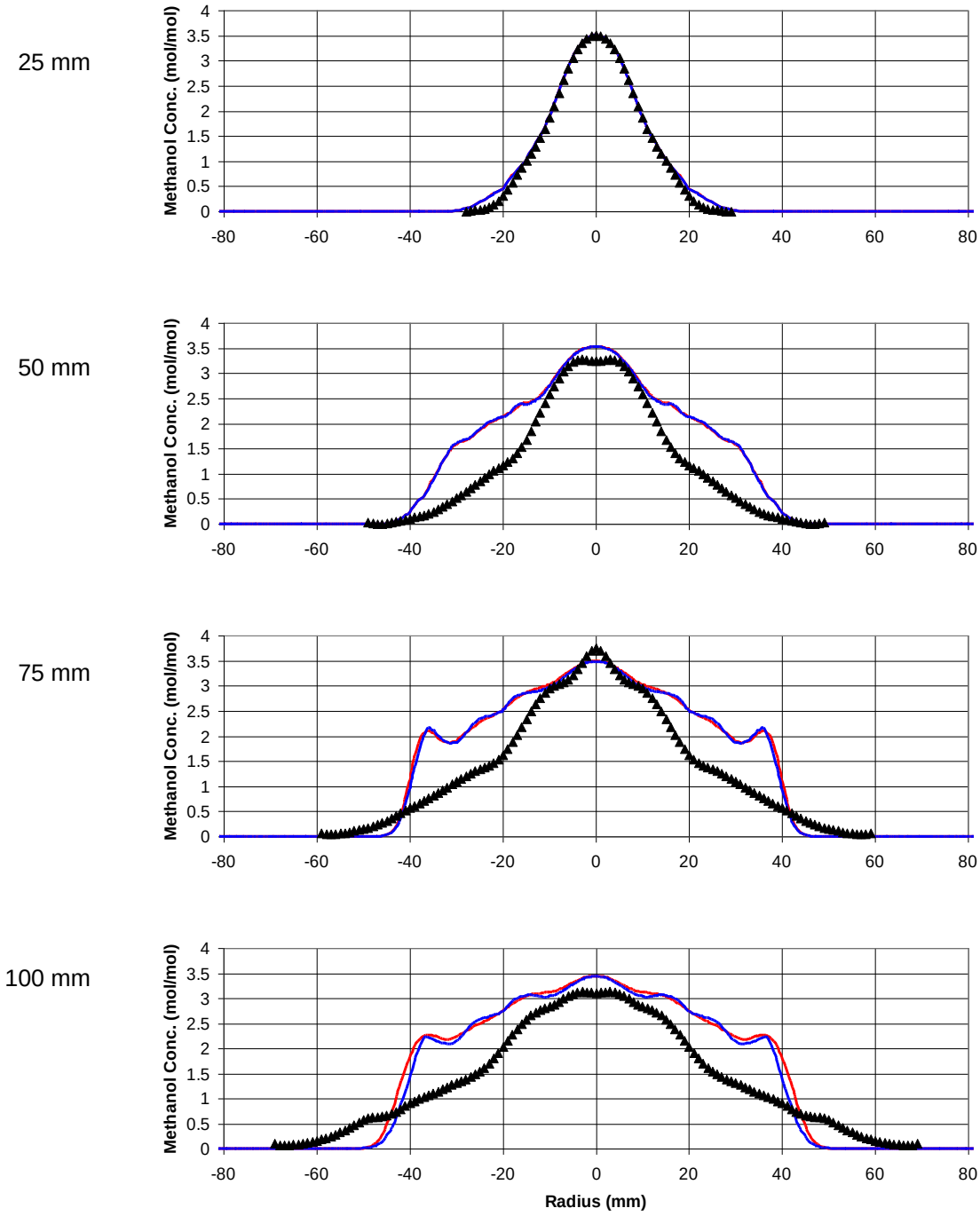

Figure 34 Predicted methanol concentration profiles for the RSA01 spray with different droplet models: — with turbulent dispersion; — without turbulent dispersion; ▲ McDonell & Samuelsen experiments. In both cases, the 'Scaled' mass flux profile and the D_{10} droplet size distribution has been used.

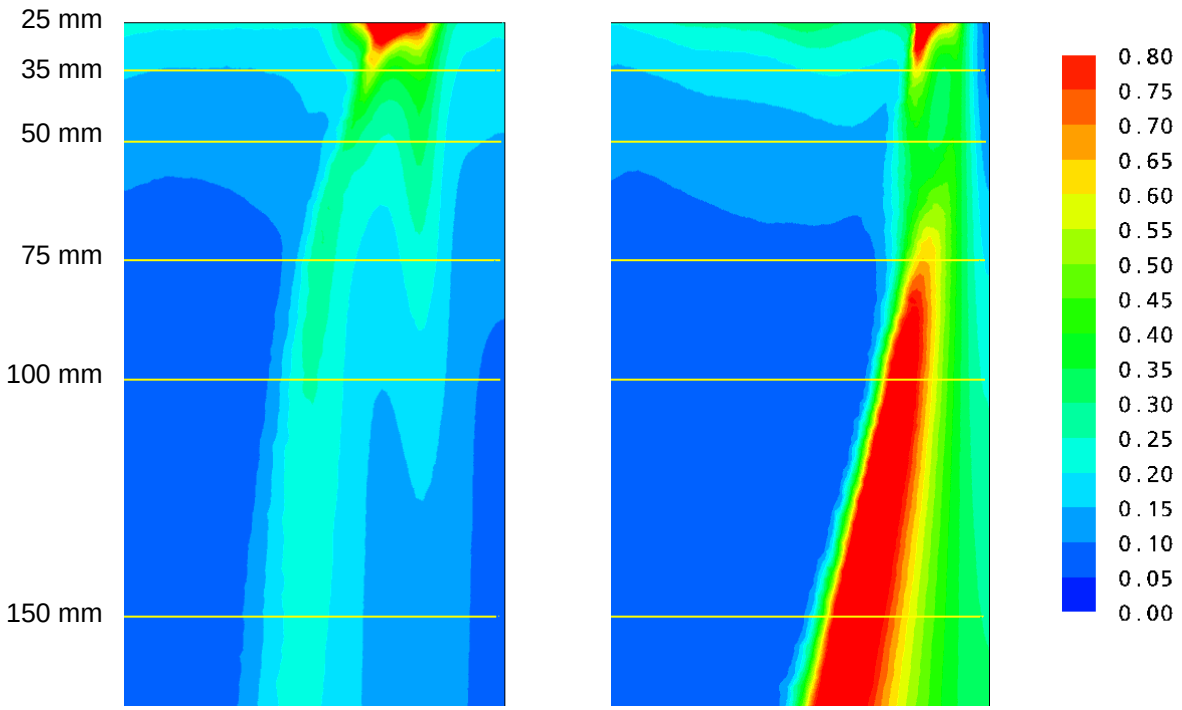

Figure 35 Predicted turbulence intensity, $\sqrt{k/|\mathbf{U}|^2}$, in the RSA01 spray (left) and RSA02 spray (right).

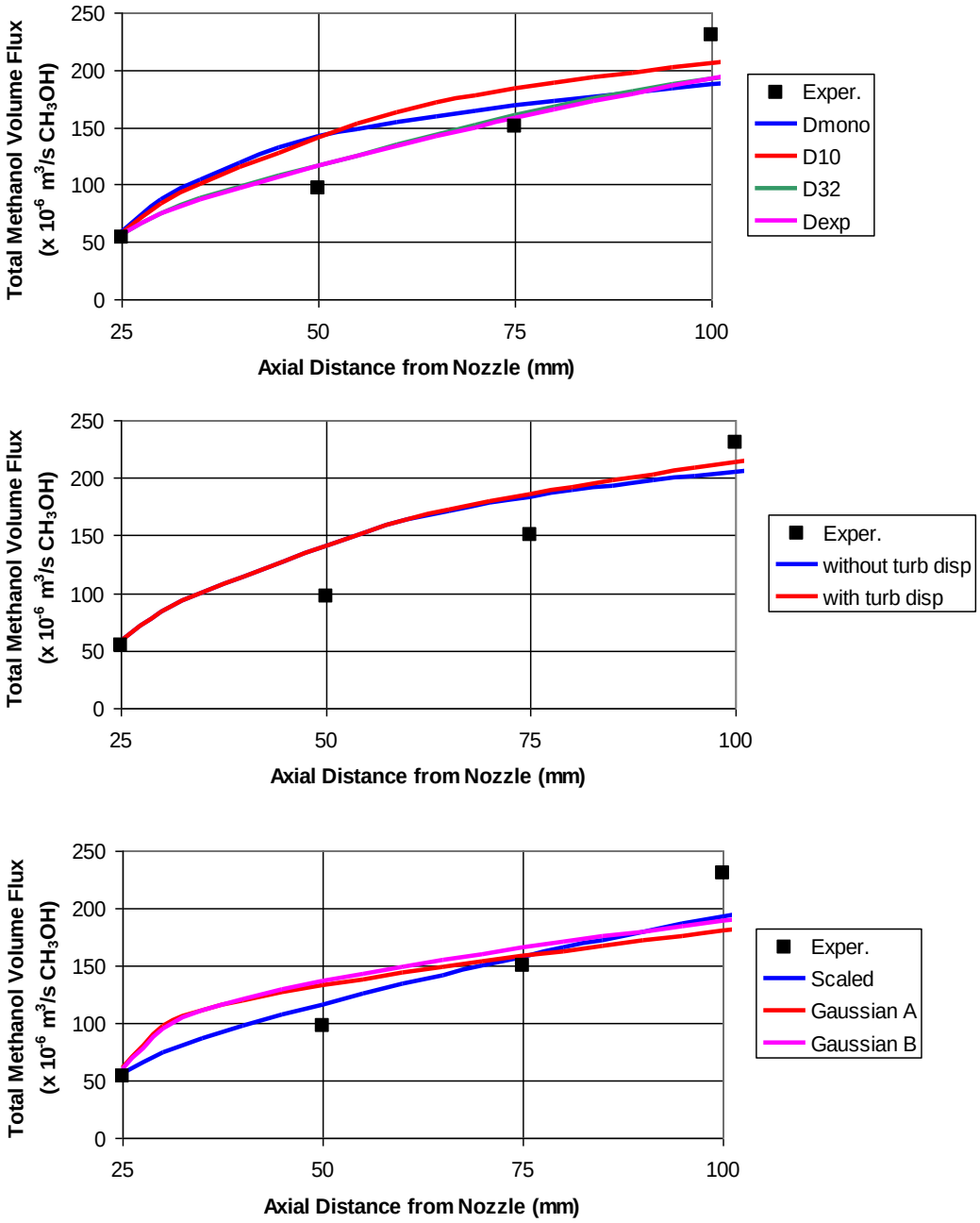

Figure 36 Predicted total volume fluxes of methanol vapour for the RSA01 spray. Three comparisons are shown: the effect of changing the drop size (top), the turbulent dispersion model (middle) and the mass flux profile (bottom).

3.6 COMPUTING COSTS

The CFD calculations in this study were performed using dual-processor 3.6 or 3.8GHz Intel Xeon computers. For most of the calculations, a previous results file was used to initialise the flow field and reduce the overall computing time needed. This makes direct comparison of the computing time required to reach converged solutions difficult, since the number of iterations required depends strongly on how close the initial flow field is to the converged solution. It is possible, however, to gain an appreciation for the relative costs associated with increasing the number of grid nodes and the number of particles by examining the relative computing times on a per iteration basis.

Figure 37 shows the relationship between the CPU seconds per iteration and either the number of grid nodes or the number of particles (each were varied independently). These indicate that there is an almost linear increase in computing effort with the number of grid nodes: doubling the number of nodes leads to a doubling in the computing time. The cost of increasing the number of particles is much less. An increase in the particle count by a factor of 4 only increased the computing time by around 40%. For a typical calculation run from scratch, with 517,000 nodes and 6,500 particles, the computing time was around 6 hours.

The difference in computing costs between increasing the number of grid nodes and increasing the number of particles is due to the different types of numerical solver involved. For the Lagrangian particles, an efficient ODE solver is used whereas for the Eulerian gas phase equations, a coupled PDE solver is used.

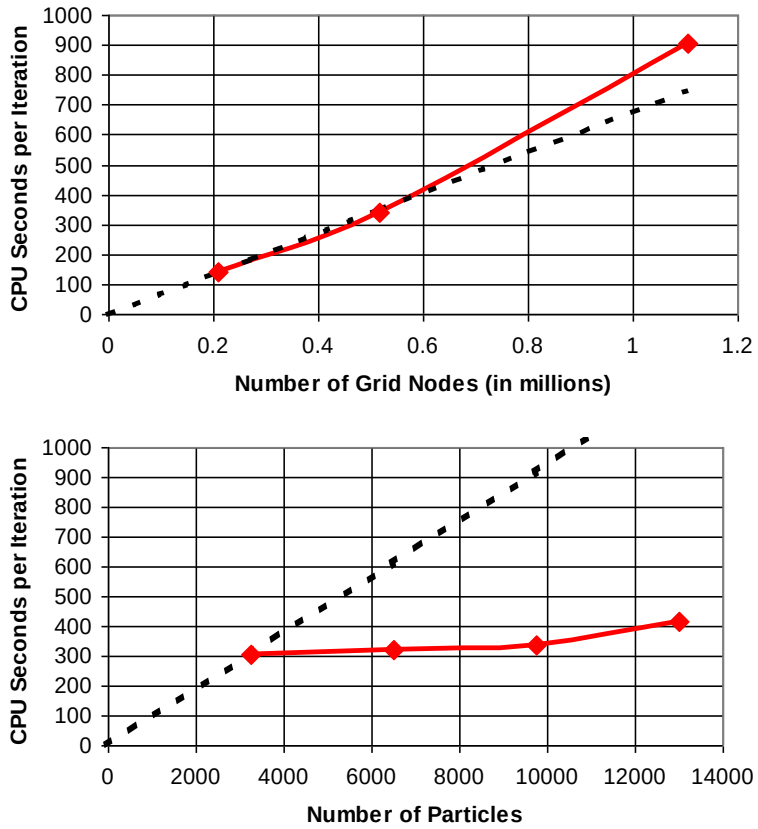

Figure 37 Computing costs as a function of the number of grid nodes and the number of particles in the CFD calculations. In each graph the dotted black line represents a simple linear increase.

4 DISCUSSION & CONCLUSIONS

Two different methanol sprays were examined in this validation study. Experimental measurements for each case were made by McDonell & Samuelsen [4-9]. The first case (RSA02) was an air-assisted spray where both methanol liquid and air were released through a nozzle at high speed (around 40 m/s). The development of the spray was shown to follow similar behaviour to a simple free-jet. CFD models were found to be able to predict correctly the velocity of the gas phase (air and vapour) without difficulty, although there were slight differences depending upon which turbulence model was used. The CFD droplet evaporation models were found to predict methanol vapour concentrations in reasonably good agreement with the experimental measurements. Sensitivity tests found that the peak concentration varied by 30% depending on the approximation used for the initial droplet size distribution, but the width of the profile and its overall shape was approximately correct. Even for a very simple representation of the spray, using 'best-guess' values instead of experimental measurements to define the inlet conditions, the resulting concentrations were only underpredicted by 25%. The results were broadly in agreement with the findings of two earlier studies [10, 11].

The other case considered was a non-air-assisted spray (case RSA01) where the flow was driven entirely by the droplets entraining air into the spray. The flow velocities were much lower in this case, typically around 3 m/s. The CFD results for this case were generally in worse agreement than the previous case. The shape of the gas phase velocity profile was not well predicted despite using experimental data to set the majority of the necessary inlet conditions for the model. Depending on the inlet mass flux profile used, the peak velocity was underpredicted by between 10 and 35%. It was expected that the model which made the best predictions of the velocity field would produce the best predictions of the vapour concentration. In practice, the model inlet conditions that gave the worst velocity profiles gave the best vapour concentration results. However, the peak vapour concentrations were generally well predicted, to within a few percent of the experimental values at all measurement positions provided that a "scaled" droplet mass flux profile was used. Again, the initial size distribution of the droplets was shown to affect the predicted concentrations, although not in the core of the spray.

There are a number of assumptions used in the CFD model that may be responsible for the differences between the CFD and the experimental results. Firstly, droplet collisions and coalescence are ignored. This should only be significant when the volume fraction of droplets exceeds 1%. The non-air-assisted spray did have a higher spray density than the air-assisted case, but the volume fraction was still less than 1%.

Secondly, in the CFD model there is no direct production of turbulence in the gas phase due to the presence of the droplets. Turbulence is only produced indirectly by shearing of the gas velocities induced by spray entrainment. This effect was investigated in the study of the RSA02 case by Kaer *et al*. [10]. They implemented the model of Shuen *et al*. [40] which takes into account directly the effect of droplets on turbulence. However, it was found to have no appreciable effect on the results.

Thirdly, the Schiller-Naumann drag coefficient correlation used here assumes that droplets are spherical, whereas in reality they may deform into more ellipsoidal shapes. It has been suggested by Gosman & Clerides [27] that this has only a minor effect in sprays. The study by Kaer *et al*. [10] modelled the 'blowing effect' where evaporation of droplets leads to a reduction in the drag coefficient. This has not been investigated in the present study and it was demonstrated in Section 2.2.1 that in theory it should have only a minor affect. It may have been more significant in the reacting flows considered by Kaer *et al*. [10] which featured much higher temperatures.

Probably the main source of discrepancy between the CFD and experimental measurements is the inlet conditions. The experiments provided nearly all of the information needed to specify the conditions at the inlet in the CFD model, which was positioned 25 mm downstream from the nozzle. However, there was still some uncertainty over the droplet mass flux profiles. Three different profiles were tested, none of which gave the correct velocity profiles in the gas phase for the RSA01 case. In addition to the primary effect of modifying the mass flux, since the droplet diameter distribution changes with radial position, the choice of mass flux profile also affects the ratio of small to large droplets which can alter the evaporation rates significantly.

The temperature of droplets and air/vapour was assumed to be 20 ˚C in the simulations whereas in reality there will have been some evaporation upstream of the 25 mm position which would have probably lowered the temperature below this. Using an overly high initial temperature in the CFD model would lead to more evaporation, due to the higher vapour pressure. This could explain the initial overprediction of the methanol vapour fluxes observed in some cases. However, it does not explain why the vapour fluxes were underpredicted further downstream from the nozzle.

It was assumed in the CFD simulations that the air entrained into the sprays was completely dry. Depending upon the amount of humidity present in the air when the experiments were undertaken, the cooling effect of the evaporating methanol spray could have caused some water vapour to condense out of the air. Any liquid water produced in this way would be likely to nucleate on the methanol spray droplets. This would have changed the heat transfer rates, due to the release of latent heat as the water changed phase from gas to liquid, and also changed the evaporation properties of the droplets, since they would be composed of a methanol-liquid mixture. The CFD simulations predicted a drop in mean air temperature from 20 ºC to around 8 ºC as the spray droplets evaporated. This equates to a drop in the equilibrium saturated water vapour concentrations in air from 2.3 to 1.0% by volume. Based on these conditions, for condensation to occur the initial relative humidity of the ambient air would have to be greater than 45%. No details are provided in McDonell & Samuelsen's papers concerning the ambient humidity when the experiments took place. They performed their experiments over a 27 month period and the results were repeatable to an error of less than 5%. Given the possible variation in humidity from summer to winter this would suggest that humidity effects were not significant.

Another possible cause of differences between experiments and CFD is from electrostatic charging of the spray droplets. Pumping liquids through pipes and spray atomisation can both induce a charge on the droplets. The charge can cause the droplets to repel one another and be attracted to any surrounding conductive surfaces that are grounded. These phenomena are exploited in electrostatic spray painting and crop spraying processes in order to obtain more uniform and complete coverage of the items sprayed. In these applications, however, specially-designed nozzles which incorporate induction charging coils or other needle devices connected to a high-voltage supplies are used to enhance the charge on the droplets (see for example [41-45]). Electrostatic effects are not mentioned in any of McDonell & Samuelsen's papers [4-9]. In the free-jet region of sprays, Watkins found that electrostatic forces accounted for at most only 5% of the hydrostatic forces even when they used an induction-charging nozzle to enhance the electrostatic effects [46]. It seems likely that in the sprays studied here, the flow was momentum dominated and that electrostatic effects were probably not significant.

The turbulence dissipation rate, ε, was not measured in McDonell & Samuelsen's experiments. Previous work by Kelsey [11] showed that this had an effect on the spreading rate of sprays. No sensitivity studies were undertaken in this study to examine its influence on results.

Notwithstanding these possible sources of error in the CFD model, it is possible that there were errors in the measurements of the spray conditions. The uncertainty associated with the measured droplet mass flux profile was discussed earlier (see also Section 3.1). McDonell & Samuelsen [9] reported a maximum systematic measurement error of 7% in their experiments with an additional 3% error associated with uncertainty due to symmetry effects.

Overall, this study indicates that CFD models can provide reasonably accurate predictions of spray evaporation. The error in the predicted total flow rate of methanol vapour produced in both of the evaporating sprays was generally less than 25%. Care should be taken, however, in extrapolating the performance of CFD models from one spray to another where the balance of physical effects such as droplet collisions and spray entrainment are different.

Only droplets composed of a single component, methanol, have been considered in the present work. Whilst multi-component droplets can be modelled using a similar approach to that adopted here with only a relatively trivial modification to the mass transfer equation for Raoult's Law, the accuracy of this approach is uncertain. Spray evaporation models developed by the automotive and aeronautical industry typically use more sophisticated models to account for the different diffusion rates of components within the droplets and for the vapour-rich boundary layer around each droplet. It is unclear whether these complications are necessary only for high-temperature/pressure combustion applications, or whether for atmospheric releases of, say, multi-component petrol mixtures, a relatively simple approach would suffice. This could be explored in future studies.

The present study has circumvented the issue of droplet breakup. In Buncefield-type releases primary breakup occurs as the liquid sheet flowing down the roof of the storage tank impinges onto a deflector plate around its rim. The cascading weir flow then separates to form filaments, blobs and droplets as it falls through the air (see Figure 1). Resolving such complexities is probably beyond the capability of industrial CFD for the foreseeable future. Although there are primary breakup models in modern commercial CFD codes, these have been tuned to high-speed flows through nozzles rather than weir flows. From a practical point of view, it would be useful to explore whether simple CFD models of the Buncefield release scenario could be developed that still capture the essential physics of the flow. One approach might be to neglect breakup entirely and instead start the spray using droplets with a predefined size, mass flux and velocity. Experiments would be needed to validate the CFD models in this case. Recent work on acetone spills by Bohl & Jackson [47] has proven that it is feasible to study experimentally the evaporation of volatile liquids and measure vapour concentrations, albeit on a laboratory scale.

5 APPENDICES

5.1 IMPLEMENTATION OF BOUNDARY CONDITIONS

In the present study, the CFD model inlet boundary conditions have been specified using experimental measurements taken by McDonell [4] at the 25 mm position, close to the nozzle exit. McDonell provided radial profiles of measured droplet axial and radial velocities, droplet mass fluxes and droplet diameter distributions at this position. In the CFD model, these conditions have been implemented using a series of circles or annuli. Table 2 summarizes the values used for the RSA02 case. Within each of the 17 circular or annular regions the droplets are assigned a velocity magnitude, droplet size distribution, droplet mass flux, particle count and a cone-angle which is representative of the trajectory determined by the measured axial and radial velocities. Droplets are then randomly injected into the CFD domain through each of these circular/annular faces. The particle count used in each case is described below in more detail (Section 5.2). Only the number-mean and Sauter mean droplet diameters (D_{10} and D_{32}) are shown in Table 2. McDonell [4] also provided more detailed information which has been used in some calculations. This consisted of droplet size distributions, expressed in terms of number of counts for 10 size classes at each of the 17 measurement positions. Assuming circular droplets, the count number has been expressed in terms of a mass fraction distribution. Two sample distributions, at the centre and periphery of the spray are given in Table 3 and Figure 38.

Table 2 Droplet parameters used for the inlet conditions with the air-assisted RSA02 case.

Radial Position (mm)	*Annulus Inner Radius (mm)*	*Outer Radius (mm)*	*Velocity Magnitude (m/s)*	*Half-Cone Angle (deg)*	*Droplet Diameter D10 (micron)*	*D32 (micron)*	*Mass Flux Scaled (g/s)*	*Gaussian (g/s)*
0	0	0.5	50.51	0.71	6.92	13.65	5.14E-05	4.69E-03
1	0.5	1.5	49.45	0.94	7.22	13.99	4.73E-04	3.69E-02
2	1.5	2.5	43.97	1.60	7.95	16.71	2.69E-03	7.04E-02
3	2.5	3.5	34.45	2.58	10.17	19.21	8.51E-03	9.77E-02
4	3.5	4.5	25.66	3.56	12.38	22.33	1.82E-02	1.17E-01
5	4.5	5.5	18.10	4.89	13.52	26.27	2.99E-02	1.27E-01
6	5.5	6.5	13.42	6.34	17.52	30.48	4.22E-02	1.28E-01
7	6.5	7.5	12.38	7.98	25.60	36.08	9.09E-02	1.22E-01
8	7.5	8.5	12.62	10.19	32.79	41.49	1.43E-01	1.10E-01
9	8.5	9.5	12.68	12.50	36.78	44.95	1.72E-01	9.52E-02
10	9.5	10.5	12.85	14.95	40.54	48.56	1.87E-01	7.86E-02
11	10.5	11.5	12.89	17.13	43.15	50.95	1.69E-01	6.23E-02
12	11.5	12.5	13.04	19.35	46.58	53.97	1.37E-01	4.74E-02
13	12.5	13.5	13.22	21.36	49.30	56.05	9.70E-02	3.48E-02
14	13.5	14.5	13.50	23.40	51.83	58.37	5.46E-02	2.46E-02
15	14.5	15.5	13.69	25.34	54.09	60.60	2.41E-02	1.67E-02
16	15.5	16.5	13.72	27.12	54.96	61.54	7.75E-03	1.10E-02
						Total	***1.184***	***1.184***

Table 3 Droplet size distributions for the air-assisted RSA02 spray at two radial positions: *r* = 0 mm and *r* = 16 mm

Droplet Diameters (micron)			*Mass Fraction*	
Min	***Max***	***Mean***	***at r = 0 mm***	***at r = 16 mm***
1	10	5.5	0.2995	0.0000
11	20	15.5	0.4918	0.0000
21	30	25.5	0.1395	0.0008
31	40	35.5	0.0654	0.0247
41	50	45.5	0.0038	0.1252
51	60	55.5	0.0000	0.2733
61	75	68	0.0000	0.3074
76	90	83	0.0000	0.2055
91	105	98	0.0000	0.0514
106	200	153	0.0000	0.0114
			1.0000	1.0000

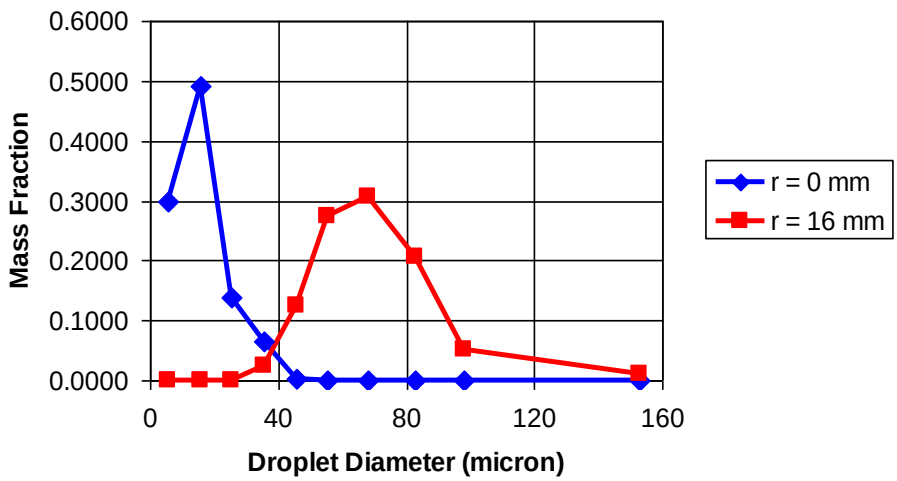

Figure 38 Droplet size distributions for the air-assisted RSA02 case at at two radial positions: *r* = 0 mm and *r* = 16 mm

In addition to measuring the droplet parameters, McDonell [4] also recorded conditions in the gas phase at the 25 mm position. This included profiles of axial and radial velocities (both mean and fluctuating RMS) and methanol vapour mole fraction. The RMS velocity fluctuations have been used to calculate the inlet turbulent kinetic energy values using $k = 0.5(\overline{u_a^2} + 2\overline{u_r^2})$, where $\overline{u_a^2}$ and $\overline{u_r^2}$ are the measured axial and radial RMS velocity fluctuations. The turbulent dissipation rate was calculated from $\varepsilon = c_\mu^{3/4} k^{3/2} / l_m$, where c_μ = 0.09 is the constant from the $k - \varepsilon$ model and l_m is a length scale equal to $0.0075L_{1/2}$, and $L_{1/2}$ is the spray half-width, equal to 0.0037m. This is the same approach adopted by Kelsey [11] and is documented in Versteeg & Malasekera [35]. A summary of the values used for the air-assisted RSA02 spray is given in Table 4.

Table 4 Gas-phase parameters used for the inlet conditions with the air-assisted RSA02 case.

Radial Position (mm)	*Annulus Inner Radius (mm)*	*Annulus Outer Radius (mm)*	*Mean Velocity Axial (m/s)*	*Mean Velocity Radial (m/s)*	*Methanol Mass Fraction (g/g)*	*Turb. Kinetic Energy, k (m^2/s^2)*	*Turb. Diss. Rate, epsilon (m^2/s^3)*
0	0	0.5	53.873	0.424	2.27E-02	1.46E+01	3.31E+04
1	0.5	1.5	52.251	1.103	2.22E-02	1.80E+01	4.52E+04
2	1.5	2.5	44.998	1.774	2.11E-02	3.20E+01	1.07E+05
3	2.5	3.5	34.116	2.138	1.94E-02	3.97E+01	1.48E+05
4	3.5	4.5	23.791	2.167	1.74E-02	3.60E+01	1.28E+05
5	4.5	5.5	15.282	1.81	1.49E-02	2.71E+01	8.36E+04
6	5.5	6.5	8.946	1.308	1.22E-02	1.67E+01	4.05E+04
7	6.5	7.5	6.455	0.907	9.43E-03	1.50E+01	3.44E+04
8	7.5	9	6.338	0.89	6.78E-03	1.92E+01	4.98E+04
10	9	11	6.254	1.364	2.59E-03	2.57E+01	7.73E+04
12	11	13	3.385	0.514	5.21E-04	2.00E+01	5.29E+04
14	13	15	0.413	-0.781	0.00E+00	1.93E+00	1.58E+03
16	15	18	0.213	-0.868	0.00E+00	1.40E-01	3.10E+01
20	18	22	0.439	-0.672	0.00E+00	6.50E-02	9.81E+00
24	22	28	0.517	-0.551	0.00E+00	4.49E-02	5.64E+00
32	28	36	0.6	-0.386	0.00E+00	5.38E-02	7.40E+00
40	36	44	0.631	-0.257	0.00E+00	6.56E-02	9.94E+00
48	44	52	0.652	-0.224	0.00E+00	4.18E-02	5.07E+00
56	52	60	0.715	-0.182	0.00E+00	4.20E-02	5.10E+00
64	60	68	0.803	-0.16	0.00E+00	5.21E-02	7.04E+00
72	68	76	0.884	-0.154	0.00E+00	4.41E-02	5.48E+00
80	76	84	0.973	-0.123	0.00E+00	4.34E-02	5.36E+00

To specify these conditions within the CFD model sub-domain, a piecewise linear interpolation was used. For a given radial location, r, between neighbouring points r_1 and r_2, the value of the mass fraction φ is calculated from:

$$\varphi = \varphi_1 + f\left(\varphi_2 - \varphi_1\right) \tag{44}$$

where φ_1 and φ_2 are the mass fractions at positions r_1 and r_2, respectively, and the interpolation factor, f, is calculated from:

$$f = \frac{r - r_1}{r_2 - r_1} \tag{45}$$

This approach is generalised to an arbitrary number of positions using a switching function, a_i, to perform piecewise linear interpolation.

$$\varphi = \sum_{i=1}^{n-1} a_i \left[\varphi_i + f\left(\varphi_{i+1} - \varphi_i\right)\right] \tag{46}$$

where:

$$a_i = step\left(r_{i+1} - r\right) \cdot step\left(r - r_i\right) \tag{47}$$

and n is the number of measurement positions. The function $step(x)$ takes a value of 1 if x is positive, 0 if x is negative and 0.5 if x is zero.

The axial coordinate is aligned with the Cartesian *z*-axis in the present study and the radial coordinate is parallel to the *x*-*y* plane. To convert the radial velocity components given in Table 4 to the Cartesian *x* and *y* components (*U* and *V*), the following formulas have been used:

$$U = [step(x) - step(-x)]u_r \cos\theta \tag{48}$$

$$V = [step(y) - step(-y)]u_r \sin\theta \tag{49}$$

$$\theta = \left|\tan^{-1}\left(\frac{y}{x}\right)\right| \tag{50}$$

where, as above, the function *step*(*x*) takes a value of 1 if *x* is positive, 0 if *x* is negative and 0.5 if *x* is zero. Here, *step*() is used to obtain the correct sign (positive/negative) for the Cartesian velocity components.

5.2 GRID-DEPENDENCY AND PARTICLE-COUNT STUDY

One of the fundamental principles of best-practice CFD is that the numerical methods and computational grid used in a simulation should not affect the results, i.e. one should use a grid such that an increase in the number of cells or slight rearrangement of them should not lead to different results. Ideally, a grid-refinement study should be undertaken. This involves running CFD simulations using a range of different grids with different resolutions (i.e. total number of grid cells). Typically, for low grid resolutions the CFD results will change as the grid is refined. However, above a certain level of grid refinement, the results will no longer change and the solution is said to be "grid-independent". Unfortunately, the number of cells required to reach a grid-independent solution is case-specific. The process to achieve a grid-independent solution is relatively straightforward to apply for single-phase flows. However, for multi-phase flow simulations, such as droplet sprays, there are further complications.

Firstly, in Lagrangian spray simulations the number of particles injected into the flow can be freely chosen. It should be noted that the number of particles is not the same as the number of droplets in the flow, each particle represents a statistical sample of many droplets. CFX note that typically between 100 and 1000 particles are used. Just like the grid-dependence issue, the number of particles should be increased incrementally until no change is observed in the solution. The number of particles required to reach a solution independent of the particle count can be sensitive to the type of droplet model used. A more complex droplet size distribution or use of a turbulent dispersion model may require a greater number of particles.

Secondly, there is a limit on the maximum volume of a grid cell that can be occupied by droplets. This arises because the mean parameters in the momentum, energy and turbulence equations for the gas flow are scaled by the void fraction (the ratio of the gas volume to the total grid cell volume). The void fraction must be non-zero and smoothly varying to avoid problems with numerical convergence. This presents difficulties near nozzles where the droplet density is high and the mesh is usually fine. There is no accepted solution to this problem. Gosman & Clerides [27] suggest that "at present, the best that can be done is to refine [the mesh] to the limits of the methodology and accept the results with limitations".

For the work documented in this report, a comprehensive grid and particle-count study was undertaken. The sensitivity to the number of particles was most apparent in the non-air-assisted

Mcdonell-Samuelsen RSA01 test case, where the vapour flow was driven by entrainment into the droplet spray. Of the various inlet models tested, the use of the experimental droplet size distributions at each of the 13 radial locations proved the most sensitive to the number of particles (the approach denoted D_{exp} in the main report).

The sensitivity to the number of particles was manifested in slight asymmetries in the flow behaviour. This was a consequence of the random distribution of particles over the injection areas and the unstructured grid. The asymmetry is most easily examined in contours of mean flow parameters on a cross-section through the spray. The flow is rotationally symmetric and so one would expect contours of the velocity, concentration etc. to appear circular in these plots. Figure 39 shows the velocity contours for three different particle counts: 500, 750 and 1000 particles, at each of the 13 injection positions for the one-quarter model geometry. In Figure 39, the full 360˚ view has been created by copying the image from the one-quarter model three times.

The top-left image in Figure 39 shows the asymmetry in the predicted droplet velocity with 500 droplets for the RSA01 case. The symmetry improves as the particle count is increased up to 1000, although the contours are still not circular even for this case. The particle count of 1000 at each injection position is equivalent to 13,000 particles for the one-quarter model or 52,000 for the full 360˚. This would usually be considered more than adequate. Figure 40 compares the velocity profiles of the 500, 750 and 1000 particle solutions. There is surprisingly little difference between the three curves given the differences previously observed in the contour plots. This may be just a consequence of a fortuitous choice of line along which the results are sampled. Figure 41 shows three profiles taken at different circumferential positions 45˚ apart for the 1000-particle case. There are some small differences of a few percent towards the outer edge of the spray. Overall, the use of 1000 particles per injection position was considered adequate. Results reported in the main report used 1000 particles for this particular case.

The use of simpler inlet conditions with a monodisperse droplet size distribution at each of the 13 radial positions (denoted D_{10} or D_{32}) led to less sensitivity to the particle count. A contour plot of the results using only 500 particles at each position is shown in Figure 42. For these, and other similar cases, the results shown in the main report used 500 particles (equivalent to 26,000 for the full 360˚).

Corresponding plots to those shown in Figures 39 and 42 for the methanol vapour concentration were more symmetric than the vapour velocity.

For the RSA02 test case, the vapour flow was driven primarily by the high-momentum release of air co-flowing through the nozzle. The vapour velocity contours therefore show little sign of asymmetry even using just 25 particles at each injection position since the droplets have very little effect on the flow velocity. The vapour concentration shows more sensitivity to the particle count. Figure 43 compares the vapour concentration for 25 and 250 particles at each of the 17 injection positions. The results shown are for the inlet conditions using experimental droplet size distributions at each of the injection locations (the most sensitive case). Results using 25 particles show some asymmetry but 250 appears to be sufficient to obtain a nearly circular distribution of contour lines. This particle count is equivalent to 4,250 for the quarter model or 17,000 for the full 360˚. All of the results reported for the RSA02 case in the main part of this report used 250 particles injected at each of the measurement positions.

Three different grid resolutions were tested for the RSA01 and RSA02 cases: coarse, medium and fine. The number of nodes was nearly doubled between each successive refinement, starting with 208,000 nodes for the quarter-geometry (coarse) and proceeding to 517,000 (medium) and 1,106,000 (fine). In each case, the grid was composed of primarily tetrahedral cells. Nodes were

tightly clustered together in the region near the inlet and expanded further out following the spray path. Plots of the medium mesh are shown in Figure 44.

There was relatively little difference between CFD results predicted on the three different meshes (Figures 45 and 46). The most significant difference was shown in the peak axial velocity for the RSA02 case, where the medium and fine mesh results were approximately 5% higher than the coarse mesh value. Results shown in the main report were obtained using the medium mesh.

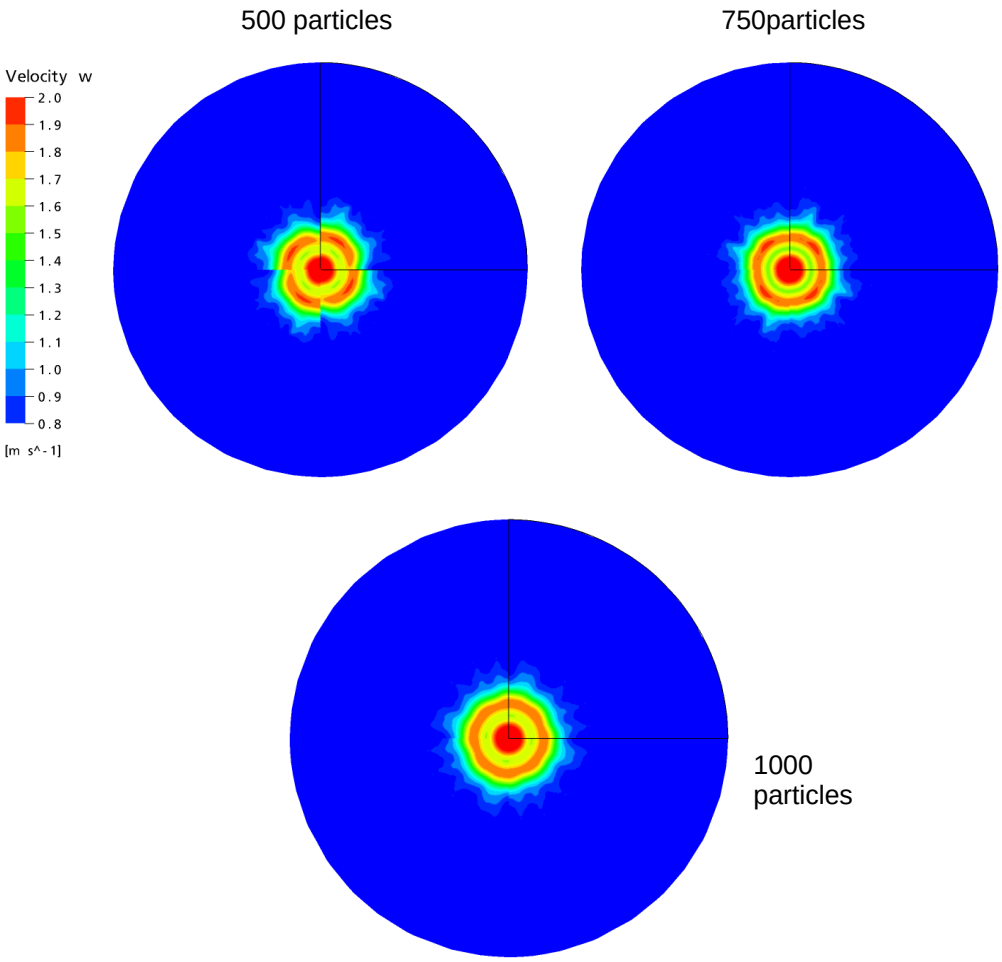

Figure 39 Contours of the axial vapour velocity for the RSA01 case at a position 100 mm downstream from the nozzle using 500, 750 and 1000 particles at each of the 13 injection positions (top left, top right and bottom, respectively). The simulations used the experimental size distributions at each of the 13 positions

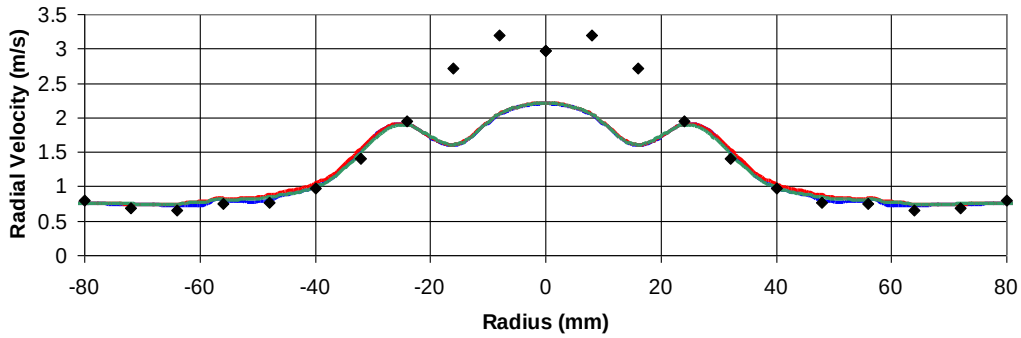

Figure 40 Profiles of the axial velocity for the RSA01 case at an axial position 100 mm downstream from the nozzle using different numbers of particles: — 500, — 750 and —1000 (at each of the 13 injection positions). Symbols: McDonell & Samuelsen experiments.

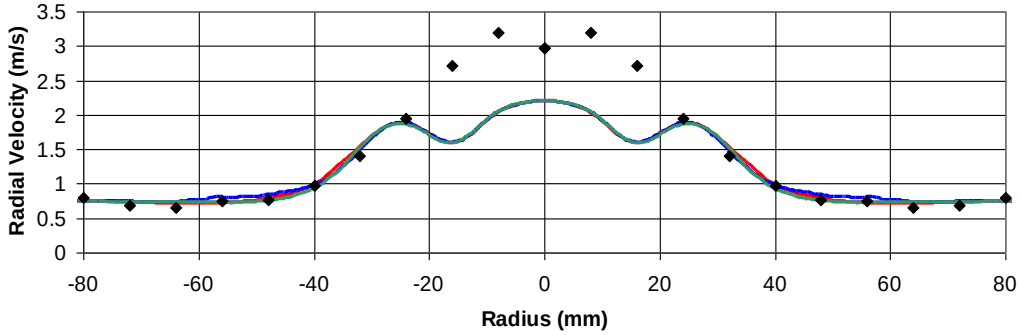

Figure 41 Profiles of the axial velocity for the RSA01 case at an axial position 100 mm downstream from the nozzle using 1000 particles at each of the 13 injection positions. Lines shown are three radial profiles at different circumferential positions: — 0˚, — 45˚ and — 90˚. Symbols: McDonell & Samuelsen experiments.

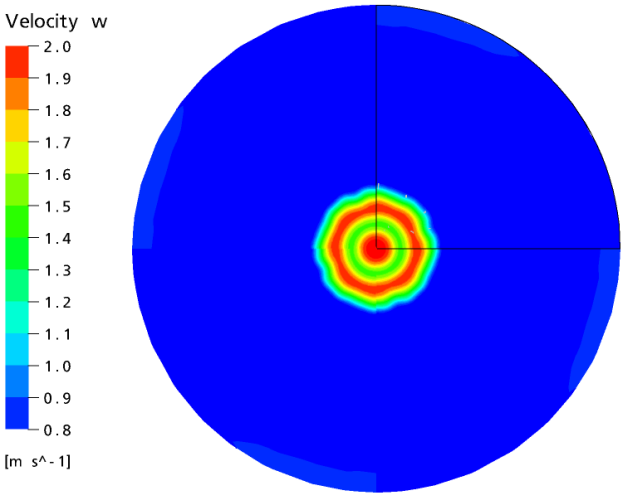

Figure 42 Contours of the axial vapour velocity for the RSA01 case at a position 100 mm downstream from the nozzle using 500 particles and a monodisperse size distribution at each of the 13 injection positions.

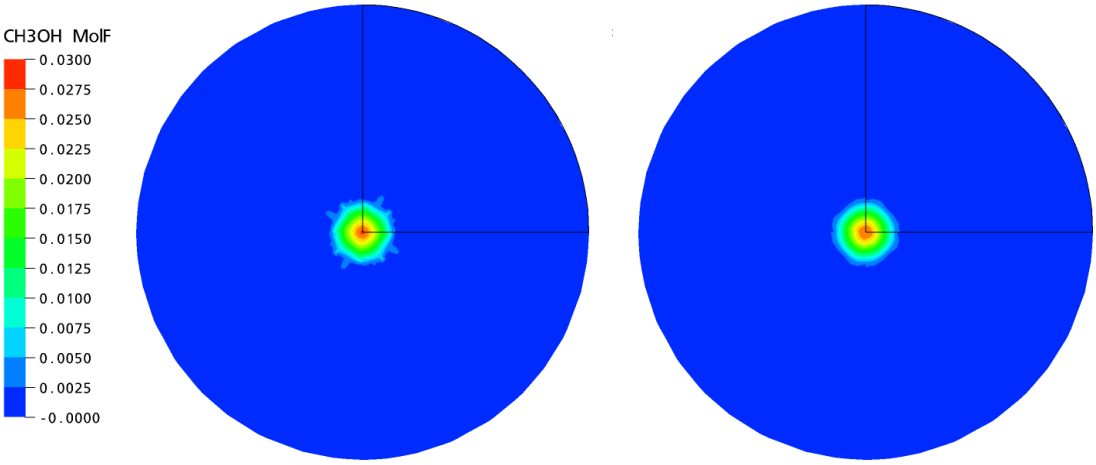

Figure 43 Contours of the molar (or volume) fraction of methanol for the RSA02 case at a position 100 mm downstream from the nozzle using 25 and 250 particles at each of the 17 injection positions (left and right, respectively).

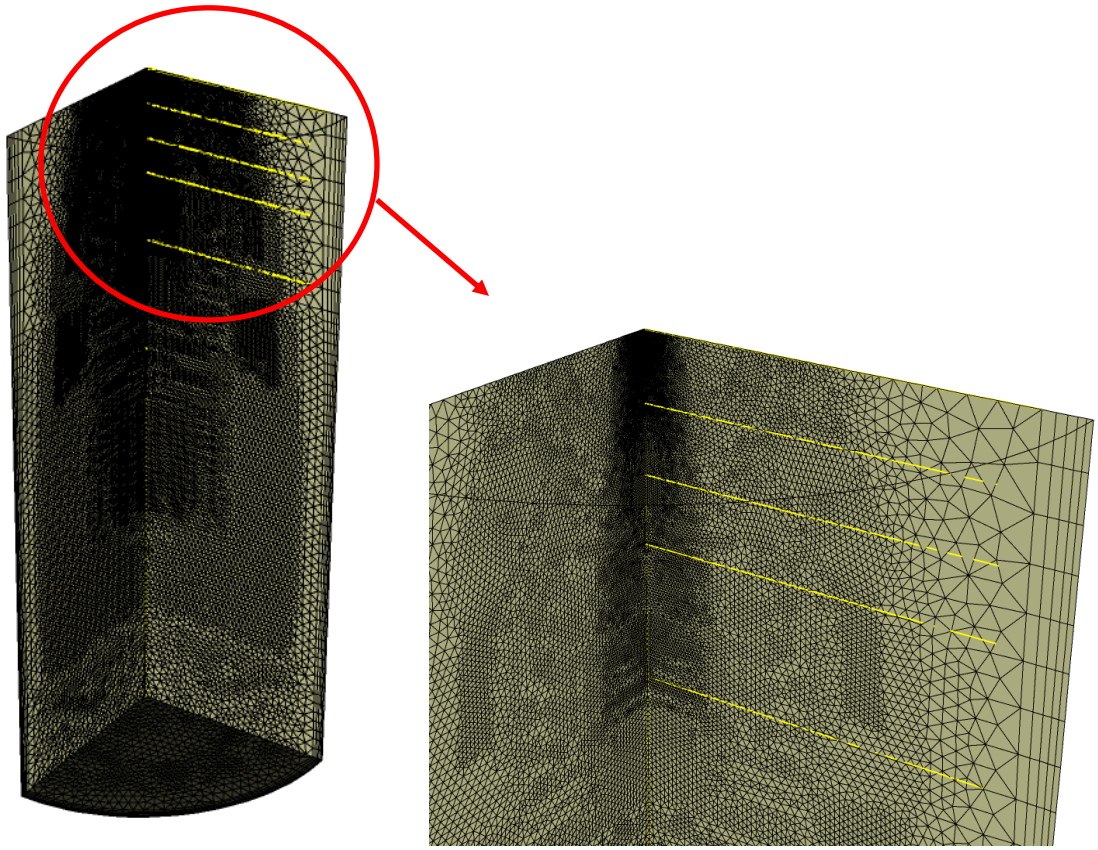

Figure 44 “Medium” resolution computational mesh. The inlet (at the top of the mesh) corresponds to the 25 mm measurement position in the McDonell & Samuelsen experiments. Yellow lines show the location of the 50, 75, 100 and 150 mm experimental measurement positions.

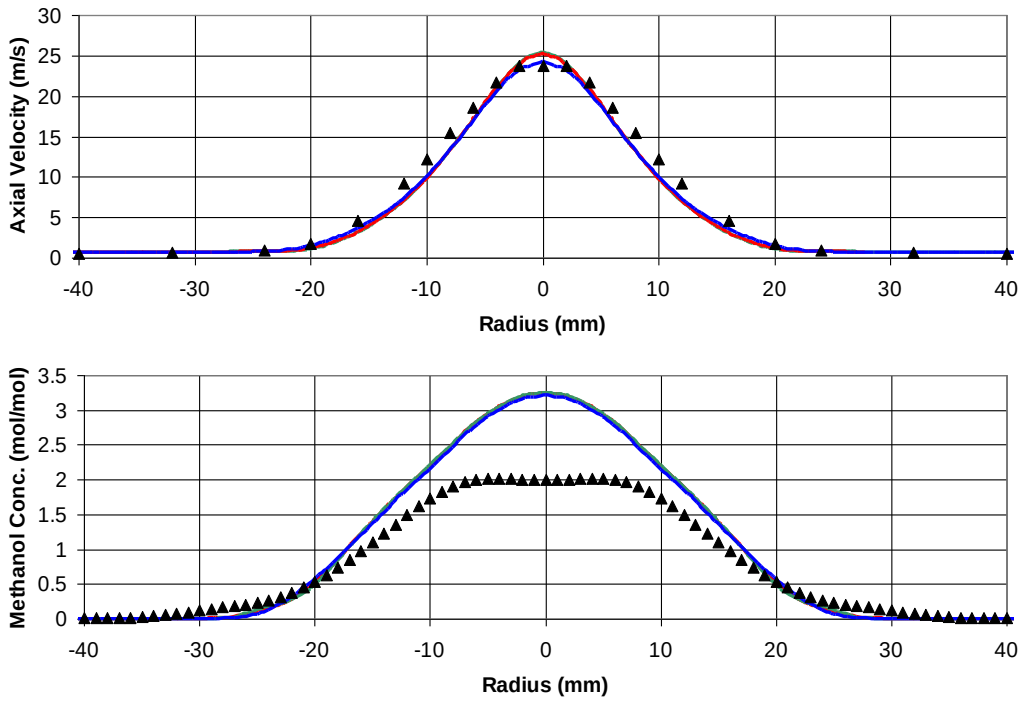

Figure 45 Profiles of the axial velocity and methanol vapour concentration for the RSA02 case at a position 100 mm downstream from the nozzle using three different meshes: — coarse, — medium — fine.

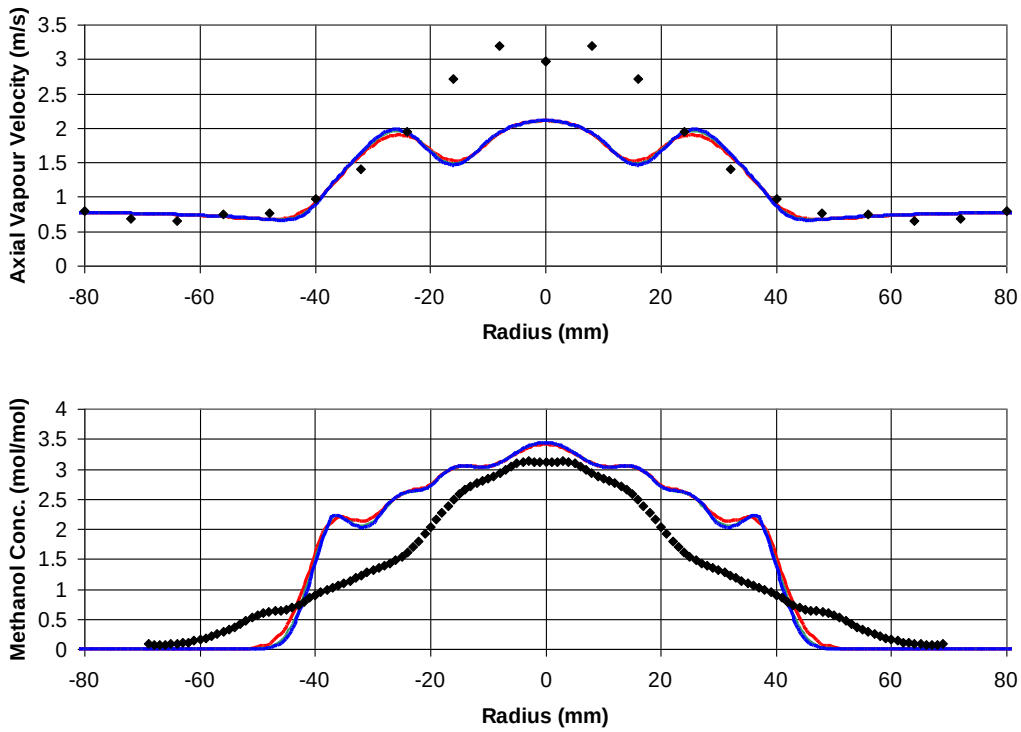

Figure 46 Profiles of the axial velocity and methanol vapour concentration for the RSA01 case at a position 100 mm downstream from the nozzle using three different meshes: — coarse, — medium — fine.

5.3 ALTERNATIVE SPRAY RELEASE MODEL

As discussed in Section 3.3, three fundamentally different CFD models for the spray release conditions were tested in the present work. The first model introduced droplets from the nozzle location and used a fully three-dimensional geometry. The second model injected droplets 25 mm downstream from the nozzle and used source terms in the model equations to force the conditions at that position to the experimental values. The third model only used one-quarter of the flow geometry and started the CFD flow domain at the 25 mm position, avoiding the need for special source-term treatments. The three models are shown in Figures 13 and 14. The third approach was similar to that adopted in two previous studies [11, 12].

The first two models proved problematic for various reasons and were abandoned. The third model was used instead to produce the results presented in the main report. The purpose of this Section is to document in greater detail the first (abandoned) spray release model. This model was unable to produce physically realistic results for evaporating sprays. There were insufficient resources within the project to explore the reasons for this behaviour but, by documenting the approach taken, the reasons for its failure could be followed up in future work.

The spray model was written in user-coded Fortran subroutines which interfaced with the CFX-10 code. The computational spray particles were introduced on a ring of radius r_{noz}. Each particle injection position was set by the angle, α, about the axis of injection, assumed to be the positive *z*-axis, as shown in Figure 47.

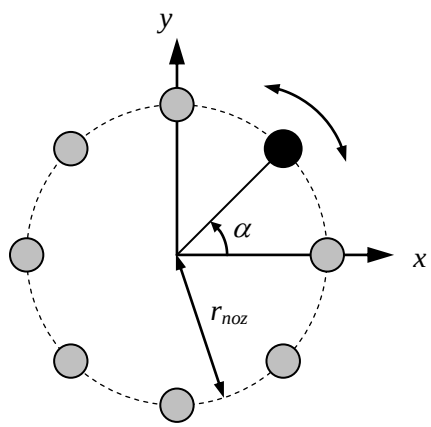

Figure 47 Particle injection viewed along the axis of injection (the *z*-axis)

The steps involved in injecting the computational particles are shown in the flow diagram presented in Figure 48. Firstly, the droplet diameter, *D*, was randomly selected between prescribed minimum and maximum diameter limits using a random number, *RND(x)*, in the range [0;1]:

$$D = \min(D) + RND(x) * [\max(D) - \min(D)] \tag{51}$$

The random number was generated using the `RAN2` routine from Numerical Recipes [48].

The probability, *P(D)*, of a droplet of diameter *D* being present in the spray was determined by interrogating the experimental droplet size histogram (details of the experimental data used for this are discussed below). The particle mass, m_p, was then calculated from:

$$m_p = \rho_l \frac{\pi D^3}{6} P(D) * C \tag{52}$$

where ρ_l is the liquid density and *C* is a constant to ensure total mass conservation, whose physical meaning is related to the number of droplets represented by the computational particle.

The cone angle, θ, for the droplet size class was assumed proportional to the radial variation in droplet size, *R(D)*:

$$\theta = \min(\theta) + R(D) * [\max(\theta) - \min(\theta)] \tag{53}$$

where *R(D)* is the normalised radial position which was interpolated from a droplet-size versus radial-position table.

Lastly, the velocity magnitude for the new particle was interpolated from a droplet-velocity versus droplet-diameter table:

$$|V_p| = f(D) \tag{54}$$

Each of the Cartesian velocity components were found from:

$$u_p = |V_p| \sin(\theta) \cos(\alpha) \tag{55}$$

$$v_p = |V_p| \sin(\theta) \sin(\alpha) \tag{56}$$

$$w_p = |V_p| \cos(\alpha) \tag{57}$$

The model required a combination of scalar input data, as summarised in Table 5, and two tabulated data sets. One table provided the variation of droplet diameter as a function of radius. Another table provided the droplet velocity as a function of its diameter. For the McDonell-Samuelsen non-air-assisted RSA01 case, it was decided to use the measurements from the plane 25 mm below the injector exit. At this plane, the droplet sizes should be representative of the spray as a whole. The measurements provided droplet size distributions at 13 radial positions. Three different approaches to generate a single representative size distribution for the spray were tested.

Table 5 User input scalar data requirements.

Variable	***Units***
Nozzle position	m
Nozzle radius	m
Inner cone angle	deg
Outer cone angle	deg
Mass flow rate	kg/s
Velocity magnitude[6]	m/s
Temperature	K
Density	kg/m^3

[6] *The velocity magnitude was only required if the table of droplet velocity magnitude as a function of droplet size was not provided.*

The first employed the droplet sizes collected at the position of the maximum-recorded velocity (at radial position, r = 22 mm). Since convective forces dominate the spray, it was postulated that droplets collected at this position might prove to be the dominant influence. The droplet size Probability Density Function (PDF) for this location is presented in Figure 49.

The second profile used droplet sizes collected at the position r = 10 mm, where the maximum number of samples was recorded (Figure 50). The decision was made to ignore the smallest droplet size classes under the assumption that small droplets (< 5 micron diameter) act as seeding particles that are carried by the air and do not contribute significantly to the spray morphology. Compared to the first case, it is evident from Figure 50 that the droplet size distribution is considerably more biased towards the smaller drop sizes.

The final profile tested, shown in Figure 51, was taken from the r = 16 mm measurements. This was the radial location associated to the maximum data rate recorded during the experiments and it was postulated that this could therefore provide the greatest contribution to the overall spray development.

Three different velocity magnitude profiles were tested, as summarized in Table 6. In theory, the measurements recorded at the 7.5 mm position closest to the nozzle (Case 1) should be the most representative of the flow at the nozzle itself. However, due to limitations in the PDA measurement technique and the high spray mass density here, the data may not be reliable.

The second case employed measurements from the plane 25 mm from the nozzle exit, where the spray was more diffuse and any PDA measurement errors should have been less significant. The droplet velocities measured here will, however, be lower than their values at the nozzle exit due to the effects of aerodynamic drag.

The third case attempted to allow for this, by applying a scalar correction to the entire velocity magnitude profile. The correction was determined from the ratio of the maximum measured velocity to the maximum predicted velocity using the profile from Case 2 at the z = 25 mm position. The shape of the velocity profiles are shown in Figure 52.

Table 6 Possible choices for velocity magnitude application

Case	*Radial location*	*Assumption*
1	7.5 mm	Closest to nozzle
2	25 mm	More representative total sample
3	25 mm	Case (2) scaled to account for deceleration

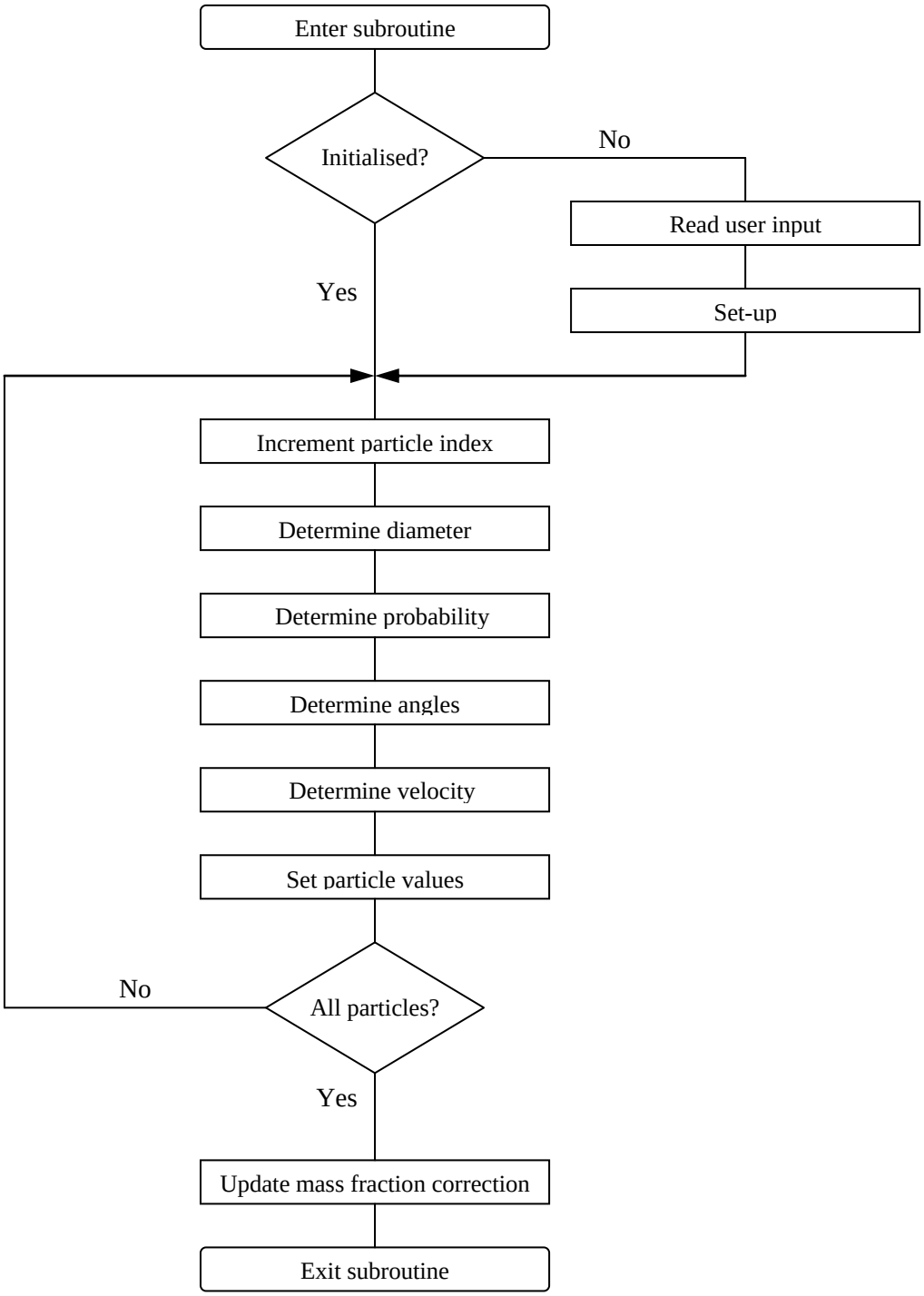

Figure 48 Flow diagram for Fortran spray initialisation program

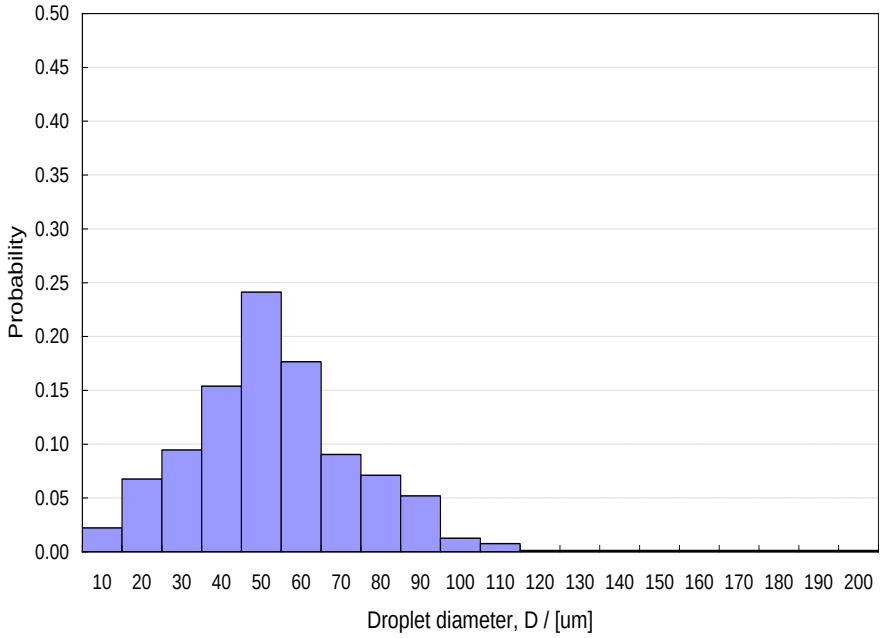

Figure 49 Droplet diameter distribution at radial position, *r* = 22 mm

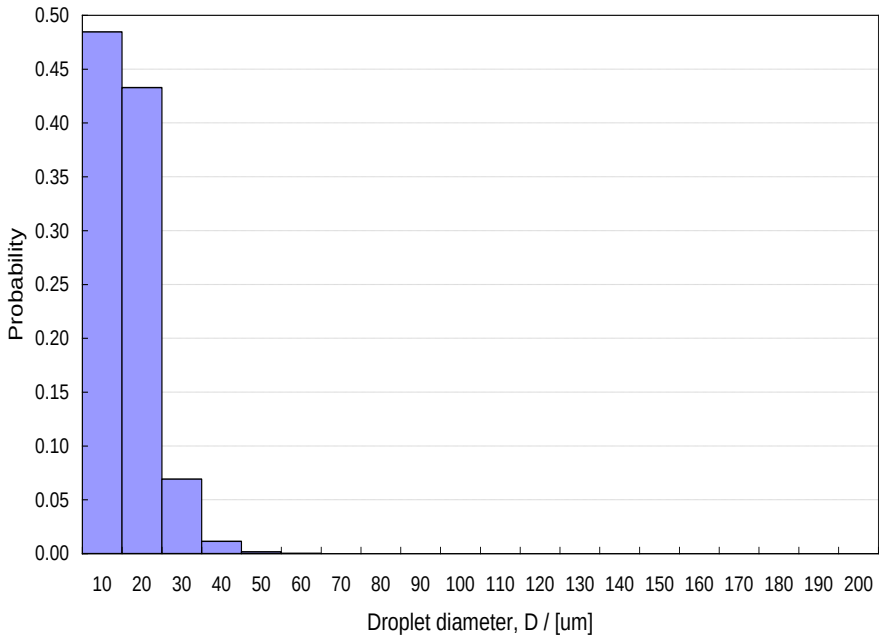

Figure 50 Droplet diameter distribution at radial position, *r* = 10 mm

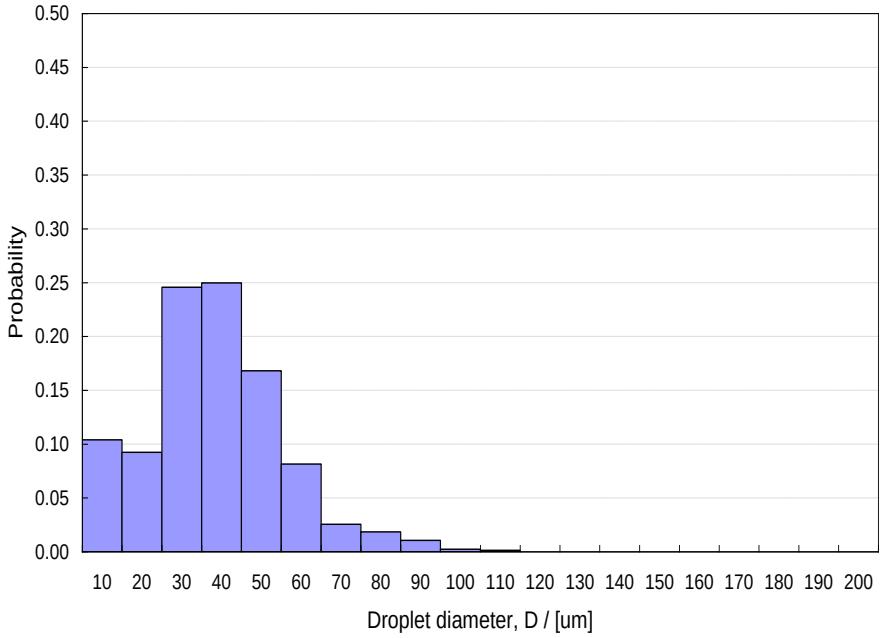

Figure 51 Droplet diameter distribution at radial position, *r* = 16 mm

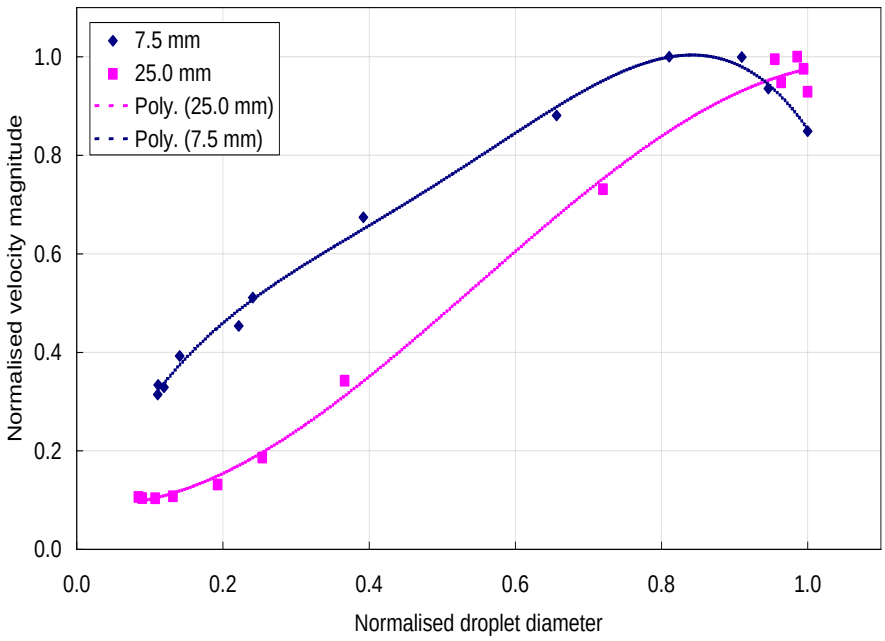

Figure 52 Velocity magnitude profiles

6 BIBLIOGRAPHY

1. *Buncefield Investigation Progress Report*, Major Incident Investigation Board (MIIB) (available from http://www.buncefieldinvestigation.gov.uk) 21 February 2006.

2. *Buncefield Investigation Second Progress Report*, Major Incident Investigation Board (MIIB) (available from http://www.buncefieldinvestigation.gov.uk) 11 April 2006.

3. *Buncefield Investigation Third Progress Report*, Major Incident Investigation Board (MIIB) (available from http://www.buncefieldinvestigation.gov.uk) 9 May 2006.

4. McDonell, V.G., *Detailed Data Set: PDI and IRES measurements in methanol sprays under reacting and non-reacting conditions*, in *Report UCI-ARTR-90-17A*, University of California at Irvine Combustion Laboratory (UCICL) August 1990 1990.

5. McDonell, V.G., M. Adachi, and G.S. Samuelsen, *Structure of reacting and nonreacting swirling air-assisted sprays.* Combust. Sci. and Tech., **82**: p. 225-248, 1992.

6. McDonell, V.G. and G.S. Samuelsen, *Structure and vaporizing pressure atomised sprays.* Atomization and Sprays, **3**: p. 321-364, 1993.

7. McDonell, V.G., M. Adachi, and G.S. Samuelsen, *Structure of reacting and nonreacting, nonswirling, air-assisted sprays, Part I: Gas Phase Properties.* Atomization and Sprays, **3**(4): p. 389-410, 1993.

8. McDonell, V.G., M. Adachi, and G.S. Samuelsen, *Structure of reacting and nonreacting, nonswirling, air-assisted sprays, Part II: Drop Behaviour.* Atomization and Sprays, **3**(4): p. 411-436, 1993.

9. McDonell, V.G. and G.S. Samuelsen, *An experimental data base for the computational fluid dynamics of reacting and non-reacting methanol sprays.* J. Fluids Eng., **117**(1): p. 145-153, 1995.

10. Kaer, S.K., K.K. Nielsen, T.J. Condra, and L.A. Rosendahl. *Numerical modelling of non-reacting and reacting non-swirling methanol sprays*. in *Third CFX International Users Conference*. 1996.

11. Kelsey, A., *CFD modelling of two-phase flashing jets: simulation of evaporating sprays to inform modelling of flashing jets*, Health & Safety Laboratory Report CM/99/08 1999.

12. Raju, M.S., *On the importance of chemistry/turbulence interactions in spray computations.* Numerical Heat Transfer, Part B: Fundamentals, **41**: p. 409-432, 2002.

13. Maremonti, M., G. Russo, E. Slazano, and V. Tufano, *Post-accident analysis of vapour cloud explosions in fuel storage areas.* Trans. IChemE, **77**: p. 360-365, 1999.

14. Yuill, J. *A discussion on losses in process industries and lessons learned*. in *51st Canadian Chemical Engineering Conference (see http://psm.chemeng.ca)*. 2001. Halifax, Nova Scotia, Canada.

15. Sirignano, W.A., *Fluid dynamics and transport of droplets and sprays*, Cambridge University Press, 2005.

16. Crowe, C., M. Sommerfeld, and Y. Tsuji, *Multiphase flows with droplets and particles*: CRC Press, 1998.

17. Herrmann, M., *Modeling primary breakup: A three-dimensional Eulerian level set/vortex sheet method for two-phase interface dynamics*, in *Center for Turbulence Research, Annual Research Briefs, Stanford University, USA* 2003.

18. Tauber, W. and G. Tryggvason, *Direct numerical simulations of primary breakup.* Computational Fluid Dynamics Journal, **9**: p. 594, 2000.

19. Cristini, V. and Y. Renardy, *Scalings for droplet sizes in shear-driven breakup: non-microfluidic ways to monodisperse emulsions.* Fluid Dynamics & Materials Processing, **2**(2): p. 77-94, 2006.

20. Pilch, M. and C.A. Erdman, *Use of breakup time data and velocity history data to predict the maximum size of stable fragments for acceleration induced breakup of a liquid drop.* Int. J. Multiphase Flow, **13**(6): p. 741-757, 1987.

21. Brodkey, R.S., *The Phenomena of Fluid Motions*: Addission-Wesley, Reading, Mass., USA, 1969.

22. Rudinger, G., *Fundamentals of gas-particle flow*, in *Handbook of Powder Technology*, Elsevier Scientific Publishing Co.: Amsterdam, 1980.

23. Rogers, G.F.C. and Y.R. Mayhew, *Thermodynamic and Transport Properties of Fluids*. Fourth Edition ed: Blackwell Publishers, 1988.

24. Lide, D.R. and H.V. Kehiaian, *CRC Handbook of Thermophysical and Thermochemical Data*: CRC Press Inc., 1994.

25. Yaws, C.L., ed. *Chemical Properties Handbook: physical, thermodynamic, environmental, transport, safety, and health related properties for organic and inorganic chemicals*. McGraw-Hill, 1999.

26. Schiller, L. and A. Naumann, *Uber die grundlegenden berechungen bei der schwerkraftaufbereitung.* Vereines Deutscher Ingenieure, **77**: p. p318-320, 1993.

27. Gosman, A.D. and D. Clerides. *Diesel spray modelling: a review*. in *Invited Lecture, Proc. ILASS-1998*. 1998. Florence, Italy.

28. Patterson, M.A., S.-C. Kong, G.J. Hampson, and R.D. Reitz, *Modeling the effects of fuel injection characteristics on diesel engine soot and NOx emissions*, in *SAE Technical Paper Series, No. 940523* 1994.

29. Eisenklam, P., S.A. Arunachalam, and J.A. Weston. *Evaporation rates and drag resistance of burning drops*. in *Eleventh Symposium on Combustion*. 1967. Combustion Institute, Pittsburgh, PA.

30. Reitz, R.D. and R. Diwakar, *Effect of drop breakup on fuel sprays*, in *SAE Technical Paper Series, No. 860469* 1986.

31. Habchi, C., D. Verhoeven, C. Huynh Huu, L. Lambert, J.L. Vanhemelryck, and T. Baritaud, *Modeling atomization and break up in high-pressure diesel sprays*, in *SAE Technical Paper Series, No. 970881* 1997.

32. Hsiang, L.-P. and G.M. Faeth, *Near-limit drop deformation and secondary breakup.* Int. J. Multiphase Flow, **18**(5): p. 635-652, 1992.

33. O'Rourke, P.J. and A.A. Amsden, *The TAB method for numerical calculation of spray droplet breakup*, in *SAE Technical Paper Series, No. 872089* 1987.

34. Pope, S.B., *Turbulent Flows*: Cambridge University Press, 2000.

35. Versteeg, H.K. and W. Malalasekera, *An Introduction to Computational Fluid Dynamics: the finite volume method*: Longman Scientific & Technical, 1995.

36. MacInnes, J.M. and F.V. Bracco, *Stochastic particle dispersion and the tracer-particle limit.* Phys. Fluids, **A4**: p. 2809-2824, 1992.

37. Gouesbet, G. and A. Berlemont, *Eulerian and Lagrangian approaches for predicting the behaviour of discrete particles in turbulent flows.* Progress in Energy and Combustion Science, **25**: p. 133-159, 1999.

38. Gosman, A.D. and E. Ioannides, *Aspects of computer simulation of liquid fuelled combustors.* AIAA: p. 81-0323, 1981.

39. Raju, M.S., *Numerical investigation of various atomizarion models in the modeling of a spray flame*, in *NASA Report CR-2005-214033 (also published as AIAA-2006-0176)* 2005.

40. Shuen, J.-S., A.S.P. Solomon, Q.-F. Zhang, and G.M. Faeth, *Structure of particle-laden jets: measurements and predictions.* AIAA Journal, **23**(3): p. 396-404, 1985.

41. Bellan, J. and K. Harstad, *Electrostatic dispersion of fuel drops to reduce soot*, in *NASA Tech Brief, Vol 22, No. 4, Item 187*, U.S. National Aeronautics and Space Administration 1998.

42. Romat, H. and A. Badri, *Internal electrification of diesel oil injectors.* Journal of Electrostatics, **51-52**: p. 481-487, 2001.

43. Krämer, H., *Safety aspects of electrostatic paint, powder and flock spraying processes.* Journal of Electrostatics, **30**: p. 77-92, 1993.

44. Jahannama, M., A.P. Watkins, and A.J. Yule, *Electrostatic effects on agricultural air-assisted sprays and deposition: Part I: An experimental Study.* Atomization and Sprays, **15**(6): p. 603-628, 2005.

45. Jahannama, M., A.P. Watkins, and A.J. Yule, *Electrostatic effects on agricultural air-assisted sprays and deposition: Part II: A computational study.* Atomization and Sprays, **15**(6): p. 629-660, 2005.

46. Watkins, A.P., *Personal Communication*, 2007.

47. Bohl, D. and G. Jackson, *Experimental study of the spill and vaporization of a volatile liquid.* J. Hazardous Mater., **140**(1-2): p. 117-128, 2007.

48. Press, W.H., B.P. Flannery, S.A. Teukolsky, and W.T. Vetterling, *Numerical Recipes in Fortran: The Art of Scientific Computing*: Cambridge University Press (see http://www.nr.com), 1992.